BAM
Bundesanstalt für
Materialforschung
und -prüfung

Dissertation

von

Kenny Ebel

Universität Potsdam

Quantification of low-energy electron induced single and double strand breaks in well-defined DNA sequences using DNA origami nanostructures

Dissertation
Zur Erlangung des akademischen Grades
"doctor rerum naturalium"
(Dr. rer. nat.)
in der Wissenschaftsdisziplin "Physikalische Chemie"

von

Kenny Ebel

Eingereicht an der
Mathematisch-Naturwissenschaftlichen Fakultät
der Universität Potsdam
Institut für Chemie

In Kooperation mit der
Bundesanstalt für Materialforschung und -prüfung

Abgabe: 25.11.2020

Tag der Disputation: 26.03.2021

Erstgutachter:	Prof. Dr. Ilko Bald
Zweitgutachter:	PD Dr. habil. Adrian Keller
Drittgutachterin:	Dr. Marie Davídková

"Science doesn't always go forwards. It's a bit like doing a Rubik's cube. You sometimes have to make more of a mess with a Rubik's cube before you can get it to go right."
Jocelyn Bell Burnell (*1943, Northern Ireland)

https://doi.org/10.25932/publishup-50449
https://nbn-resolving.org/urn:nbn:de:kobv:517-opus4-504499

Abstract

Ionizing radiation is used in cancer radiation therapy to effectively damage the DNA of tumors leading to cell death and reduction of the tumor tissue. The main damage is due to generation of highly reactive secondary species such as low-energy electrons (LEE) with the most probable energy around 10 eV through ionization of water molecules in the cells. A simulation of the dose distribution in the patient is required to optimize the irradiation modality in cancer radiation therapy, which must be based on the fundamental physical processes of high-energy radiation with the tissue. In the present work the accurate quantification of DNA radiation damage in the form of absolute cross sections for LEE-induced DNA strand breaks (SBs) between 5 and 20 eV is done by using the DNA origami technique. This method is based on the analysis of well-defined DNA target sequences attached to DNA origami triangles with atomic force microscopy (AFM) on the single molecule level. The present work focuses on poly-adenine sequences (5'-d(A_4), 5'-d(A_8), 5'-d(A_{12}), 5'-d(A_{16}), and 5'- d(A_{20})) irradiated with 5.0, 7.0, 8.4, and 10 eV electrons. Independent of the DNA length, the strand break cross section shows a maximum around 7.0 eV electron energy for all investigated oligonucleotides confirming that strand breakage occurs through the initial formation of negative ion resonances. Additionally, DNA double strand breaks from a DNA hairpin 5'-d$(CAC)_4$T(Bt-dT)$T_2$$(GTG)_4$ are examined for the first time and are compared with those of DNA single strands 5'-d$(CAC)_4$ and 5'- d$(GTG)_4$. The irradiation is made in the most likely energy range of 5 to 20 eV with an anionic resonance maximum around 10 eV independently of the DNA sequence. There is a clear difference between σ_{SSB} and σ_{DSB} of DNA single and double strands, where the strand break for ssDNA are always higher in all electron energies compared to dsDNA by the factor 3. A further part of this work deals with the characterization and analysis of new types of radiosensitizers used in chemoradiotherapy, which selectively increases the DNA damage upon radiation. Fluorinated DNA sequences with 2'-fluoro-2'-deoxycytidine (^{dF}C) show an increased sensitivity at 7 and 10 eV compared to the unmodified DNA sequences by an enhancement factor between 2.1 and 2.5. In addition, light-induced oxidative damage of 5'-d$(GTG)_4$ and 5'-d($(CAC)_4$T(Bt-dT)$T_2$$(GTG)_4$) modified DNA origami triangles by singlet oxygen $^1O_2$ generated from three photoexcited DNA groove binders [ANT994], [ANT1083] and [Cr(ddpd)$_2$][BF$_4$]$_3$ illuminated in different experiments with UV-Vis light at 430, 435 and 530 nm wavelength is demonstrated. The singlet oxygen induced generation of DNA damage could be detected in both aqueous and dry environments for [ANT1083] and [Cr(ddpd)$_2$][BF$_4$]$_3$.

Zusammenfassung

In der Radiotherapie wird ionisierende Strahlung verwendet, um die DNA in Tumorzellen wirksam zu schädigen. Der Hauptschaden ist auf die Erzeugung hochreaktiver Sekundärspezies wie niederenergetische Elektronen (LEE) durch Ionisierung von Wassermolekülen in den Zellen mit einer wahrscheinlichsten Energie um 10 eV zurückzuführen. Die Optimierung der Bestrahlungsmodalität in der Strahlentherapie beruht auf Simulationen der Dosisverteilung im menschlichen Körper, die auf fundamentale physikalische Prozesse zwischen hochenergetischer Strahlung mit dem Gewebe basieren.

Die vorliegende Arbeit beschäftigt sich mit der exakten Quantifizierung von LEE-induzierten DNA-Strahlenschäden in Form von absoluten Wirkungsquerschnitten σ_{SB} für DNA-Strangbrüche (SBs) zwischen 5 und 20 eV mit Hilfe der DNA-Origami-Technik. Diese Methode verwendet wohl definierte DNA-Zielsequenzen gebunden an DNA-Origami Nanostrukturen, dessen Schädigung durch die Rasterkraftmikroskopie auf Einzelmolekülniveau untersucht werden kann. Ein großer Fokus liegt auf den Bestrahlungsexperimenten von Polyadeninsequenzen ((5'-d(A_4), 5'-d(A_8), 5'-d(A_{12}), 5'-d(A_{16}) und 5'-d(A_{20}) unterschiedlicher Nukleotidanzahl) bestrahlt mit 5.0, 7.0, 8.4 und 10 eV Elektronen. Unabhängig von der DNA-Nukleotidlänge zeigen die Strangbruchquerschnitte für alle untersuchten Oligonukleotide ein Maximum um 7.0 eV Elektronenenergie. Diese DNA-Strangbrüche sind durch die anfängliche Bildung negativer Ionenresonanzen bedingt. Zusätzlich werden erstmals Wirkungsquerschnitte für DNA-Doppelstrangbrüche σ_{DSB} spezifischer Sequenz (5'- d(CAC)$_4$T(Bt-dT)T$_2$(GTG)$_4$) ermittelt und mit den Wirkungsquerschnitten von DNA-Einzelstrangbrüchen σ_{SSB} (5'- d(CAC)$_4$ und 5'-d(GTG)$_4$) verglichen. Die Bestrahlungen erfolgen im Energiebereich von 5 bis 20 eV mit einem anionischen Resonanzmaximum um 10 eV unabhängig von der DNA-Sequenz. Es wird ein deutlicher Unterschied zwischen σ_{SSB} und σ_{DSB} von DNA-Einzel- und Doppelstrangbrüchen im Verhältnis von 3 zu 1 erhalten. Des Weiteren befasst sich ein großer Forschungsbereich in der Radiochemotherapie mit der Charakterisierung und Analyse neuer Radiosensibilisatoren, die den DNA-Schaden bei Bestrahlung selektiv erhöhen können. Dafür werden DNA-Sequenzen mit 2'-Fluor-2'-desoxycytidin (^{dF}C) modifiziert, die eine erhöhte Empfindlichkeit mit einem Verstärkungsfaktor zwischen 2.1 und 2.5 bei 7 und 10 eV im Vergleich zu den nicht modifizierten DNA-Sequenzen zeigen.

Außerdem können mit der DNA-Origami-Technik lichtinduzierte oxidative DNA-Schädigungen von 5'-d$(GTG)_4$ und 5'- d$(CAC)_4$T(Bt-dT)$T_2$$(GTG)_4$ durch hochreaktivem Singulett-Sauerstoff $^1O_2$ untersucht werden. Der Singulett-Sauerstoff wird durch photoaktive DNA-Binder [ANT994], [ANT1083] und $[Cr(ddpd)_2][BF_4]_3$ mit UV-Vis Licht bei Wellenlängen von 430, 435 und 530 nm gebildet, die sich auf den DNA-Origami Nanostrukturen nahe den Zielsequenzen zufällig binden. Die Erzeugung von DNA-Schäden konnte sowohl in wässriger als auch in kondensierter Umgebung durch [ANT1083] und $[Cr(ddpd)_2][BF_4]_3$ nachgewiesen werden.

Contents

Abbreviations

Abbreviations

^{2F}A	2-fluoroadenine
^{dF}C	2'-fluoro-2'-deoxycytidine
^{5F}U	5-fluorouracil
°C	Degrees Celsius
A	Adenine
A	Ampere
Å	Angström; 10^{-10} m
AA	Associative attachment
AD	Autodetachment
AFM	Atomic force microscopy
AGE	Agarose gel electrophoresis
ANO	Anode
BNC	Bayonet Neill–Concelman – coaxial connector
bp	Base pair
Bt	Biotin
C	Cytosine
C	Coulomb; 1 As
ca	Circa
Cl-ara	Clofarabine; (IUPAC)
cm	Centimeter; 10^{-2} m
CS	Cross section
d	Diameter of double stranded DNA
$d_{1/2}$	Diameter of single stranded DNA
d_i	Diameter of discrete circles of the electron beam
D^0	Bond dissociation energy
DEA	Dissociative electron attachment
DNA	Deoxyribonucleic acid

DSB	Double strand break
dsDNA	Double stranded DNA
E	Energy
EA	Electron affinity
EDTA	Ethylenediaminetetraacetic acid
EELS	Electron energy loss spectroscopy
EF	Enhancement factor
EI	Electron ionization
ENG	Energy for electron acceleration
EPO	Endoperoxide
eq	Equation
EtOH	Ethanol
eV	Electronvolt
EXT	Extractor; third electrostatic lens in the electron gun
F	Fluorine
F_{FC}	Absolute fluence
F	Relative Fluence
F-ara	Fludarabine
FC	Faraday cup
FCP	Franck-Condon principle
fig	Figure
FIL	Filament
FRET	Förster resonance energy transfer
fs	Femtosecond; 10^{-15} s
FWHM	Full-width-at-half-maximum
G	Guanine
g	Centrifugal force
Gem	Gemcitabine; 2′-2′-difluorodeoxycytidine
Gy	Gray

h	Hour
h	Height position(z-coordinate) of the faraday cup
H_2O	Water
HOMO	Highest occupied molecule orbital
HPLC	High performance liquid chromatography
Hz	Hertz; 10^0 s^{-1}
I	Current
I_i	Current of a certain area Z_i
I_i^s	Current of a certain square area Z_s
IE	Ionization energy
IVR	Intramolecular vibrational energy redistribution
kcal	Kilocalories
K_d	Dissociation constant
kDa	Kilodalton
kg	Kilogramm
kHz	Kilohertz; 10^3 Hz
k_i	Distance from a discrete circle to the center of the beam
L	Length
LEE	Low energy electron
LET	Linear energy transfer
LMDS	Local multiply damage site
LUMO	Lowest unoccupied molecular orbital
MeV	Megaelectron volt
MO	Molecular orbital
Mol	Molar
m	Meter; 10^0 m
mbar	Millibar; $10^5 \frac{\mathrm{kg}}{\mathrm{m}*\mathrm{s}^2}$
mM	Millimolar; $10^{-3} \frac{\mathrm{mol}}{\mathrm{m}^3}$
mm	Millimeter; 10^{-3} m

ms	Milliseconds; 10^{-3} s
µL	Microliter; 10^{-9} m^3
µs	Microseconds; 10^{-6} s
N	Newton; $\frac{\mathrm{kg} \cdot \mathrm{m}}{\mathrm{s}^{-2}}$
nA	Nanoampere; 10^{-9} A
n_e	Number of electrons
nm	Nanometer; 10^{-9} m
nM	Nanomolar
N_p	Number of projectiles
N_R	Number of reactions
ns	Nanosecond; 10^{-9} s
N_{SB}	Number of strand breaks
N_{SB0}	Number of strand breaks at zero fluence
N_T	Number of targets
nt	Nucleotide
N_0	Maximum number of intact oligonucleotides
PDT	Photodynamic therapy
PIA	Picoamperemeter
PS	Photosensitizer
ps	Picosecond; 10^{-12} s
Ref	Reference
r_i	Radius of discrete circles of the electron beam
RS	Radiative stabilisation
s	Second; 10^0 s
SAM	Self-assembled monolayers
SAv	Streptavidin
SI	Système international d'unités
SB	Strand break
SSB	Single strand break

ssDNA	Single stranded DNA
T	Thymine
tab	Table
TAE	TRIS Acetat-EDTA
TNI	Transient negative ion
Tris	Tris(hydroxymethyl)aminomethane
UHV	Ultra high vacuum
UV	Ultraviolet radiation
VAE	Vertical attachment energy
VDE	Vertical detachment energy
VEA	Vertical electron affinity
VIE	Vertical ionization energy
VdW	Van-der-Waals forces
WEH	Wehnelt cylinder
Z_i	Circle area
Z_i^s	Square area
Γ	Heisenberg uncertainty
$\hbar$	Reduced Planck constant
σ	Cross section
τ	Lifetime

1 Introduction

The discovery of x-rays, radioactivity and nuclear fusion made people aware that irradiation of a living being and thus human cells with high-energy electromagnetic or particle radiation can have serious consequences. One of the most important and most fragile points of attack is the deoxyribonucleic acid (DNA) in living cells. However, everyday things, such as overdosed sunlight [1] and high energy radiation [2], aging, immune conditions or chemical substances [3] can also lead to structural damages leading to a restriction on its functionality or even to inherited genetic mutations. The cells have many effective repair mechanisms [4] that ultimately reach their limits in the event of DNA double strand breaks. Irreparable DNA damage causes the cell to initiate cell death in order not to damage the genetic information [5]. If cell death is no longer possible, this usually leads to rapid and uncontrolled cell growth, which is usually the diagnosis of cancer. Cancer is the second most common cause of death in developed countries, exceeded by heart disease [6]. There are many cancer therapies available, some of which are more stressful on the body than others [7]. The most frequently used methods are surgery, chemo- and radiotherapy or a combination of all [8]. However, the type and position of the tumor in the body, as well as the physical constitution of the patient, the stage of the disease, are decisive for the choice and severity of cancer therapy. In some cases, tumors cannot be surgically removed due to their position or the spread of the tumor makes surgical removal impossible. Therefore, radiation is used for treatment in radiotherapy in which carcinogenic tissue is irradiated. Modern radiotherapy technologies increase the precision of dose delivery into defined target volume. In order to increase the effect of radiotherapy, radiation sensitive molecules (radiosensitizers) are administered in the human body to enhance the effect of ionizing radiation. The uptake of the radiosensitizers is higher for cancer cells, since they have a faster metabolism compared to healthy cells. Hence, the understanding of the reaction mechanism of different types of radiation, such as γ-ray, X-ray, particle radiation and high energy electron beams with the surrounding tissue is of fundamental interest in radio- or the combined chemoradiotherapy. Depending on the radiation type and energy, different irradiation beam shapes, penetration depths and energy distribution of the incoming particle in the medium can be reached. Independently of the radiation type, the therapies are based on the generation of secondary particles through the ionization of the surrounding water in the cells. One of the most abundant secondary species produced by ionizing radiation are low-energy electrons (LEEs) [9] and can damage the DNA via dissociative electron attachment (DEA). LEEs are generated along the radiation track with the most likely energy between 0 and 20 eV with a maximum at around 10 eV. The most favored process of DNA damage via DEA over transient negative ions (TNI) is formed by attachment of an electron to a formerly unoccupied molecule orbital at a specific resonance energy. The reaction mechanism between the DNA and LEEs that lead to tumor reduction or death have not yet been fully understood. A simulation of the dose distribution in the patient is required to optimize the irradiation modality in cancer radiation therapy, which must be based on the fundamental physical processes of high-energy radiation with the tissue. Consequently, there is a need of accurate quantification of DNA radiation damage in the form of absolute cross sections for radiation-induced DNA strand breaks (SBs). Therefore, a broad range of experimental methods have been developed to study the interaction of LEEs with cells, biomolecules, plasmid DNA, DNA oligonucleotides or DNA building blocks. Each method varies in the type of information that can be obtained and the size and complexity of the system that can be effectively studied. The in vivo study of tumor growth and survival rates can be monitored in animals for different radiation in combination with radiosensitizers and are the closest system with one of the highest biological relevance. Complex biological systems like cells yield important information about the survival probability. Instead, detailed fragmentation mechanisms with unclear biological relevance can be examined in idealized DNA building blocks. Nevertheless, there is an information gap between short DNA nucleotides leading information about fragmentation mechanism and complex DNA structures like supercoiled plasmid DNA yielding information about non-specific electron dependent DNA damage. With the invention of the DNA origami technique from *Keller et al.* in 2012 [10], the investigation of LEE-induced DNA damage of well-defined DNA oligonucleotides using DNA origami triangles reaches a new level and closes the information gap. This technique enables the study of LEE-induced DEA to customized DNA oligonucleotides with different DNA sequences [11], length [12], topology [13] and modifications with radiosensitizers [14] in dependence of the radiation source and energy.

The present work is produced in cooperation with the University of Potsdam and the Federal Institute of Materials Research and Testing and deals with the investigation of DNA damage caused by electron-induced reactions in vacuum using the DNA origami technique. A new established setup from *Rackwitz et al.* [15], [16] is further developed and is used to quantify the sequence, length and electron energy dependencies of DNA single and double-strand breaks. The DNA damage is visualized by atomic force microscopy (AFM) on the single molecule level. Chapter two describes the theoretical background of the DNA as the main target molecule and its fundamental reactions with highly reactive secondary particles (LEE), radiation and photosensitive molecules. The necessary experimental setup for the investigation of LEE-induced DNA strand breaks is explained in more detail in chapter three. Chapter four focuses on poly-adenine DNA single strands with 4, 8, 12, 16 and 20 nucleotides irradiated at 5, 7, 8,4 and 10 eV electron energy. Independent of the DNA length, the strand break cross section of all sequences show a maximum around 7.0 eV electron energy. Additionally, DNA double strand breaks from 5′- d$(CAC)_4$T(Bt- dT)$T_2(GTG)_4$ are examined for the first time using the DNA origami method and are compared with those of DNA single strands 5′-d$(CAC)_4$ and 5′-d$(GTG)_4$. The effects of LEEs in a most likely energy range between 5 and 20 eV are important to study as a basic research of radiation damage to biomolecules regardless of the related implications for applications of ionizing radiation in medicine.

Furthermore, a wide field of new radiosensitizers incorporated into the DNA sequence or DNA binders non-covalently bound by ion exchange are investigate to enhance the sensitivity against DNA damage upon radiation. On the one hand, the investigation of the radiosensitizer 2′-fluoro-2′-deoxycytidine (^{dF}C) incorporated into short DNA oligonucleotides is presented and the absolute DNA strand break cross sections are determined in dependence of the electron energy at 7 and 10 eV. The enhancing effect of ^{dF}C compared to the unmodified DNA sequence is between 2.0 and 2.5 depending on the DNA sequence order and irradiation energy. On the other hand, photosensitive DNA binder are molecules that generate the reactive singlet oxygen $^1O_2$ in the presence of molecular oxygen $^3O_2$ upon irradiation with UV-Vis light. $^1O_2$ is known as highly reactive species and can induce single or double strand breaks in the direct vicinity of DNA. For the first time, the three DNA binders [ANT994], [ANT1083] and $[Cr(ddpd)_2][BF_4]_3$ are bound to modified DNA origami triangles with 5′-d$(GTG)_4$ and 5′-d$((CAC))_4$T(Bt-dT)$T_2(GTG)_4)$ target DNA strands and illuminated in different experiments with UV-Vis light at 430, 435 and 530 nm wavelength for up to one hour (h). A slight DNA strand damage could be determined in both the aqueous and dry state, whereby [ANT1083] and $[Cr(ddpd)_2][BF_4]_3$ are confirmed as potential DNA photosensitive molecules. Independent of all radiation experiments, determining the DNA damage using AFM analysis is very time-consuming. Therefore, the *Pythagoras* software was developed specifically for this method, which supports and greatly reduces the analysis time.

2 Theoretical Background

This chapter explains fundamental knowledge and theoretical processes of the DNA and their interaction with radiation. Moreover, the basics for cancer therapies are discussed and an insight into the current status of cancer research is given.

2.1 Deoxyribonucleic acid

In nature, DNA developed as a highly compressed storage for genetic information and is able to code the blueprint of a whole organism. The structure of the DNA was successfully analyzed in 1953 by James D. Watson and Francis Crick using X-ray diffraction [17]. The DNA stores the genetic information for the development, function and reproduction of all living organisms. It is a right-handed double helix consisting of two polynucleotide chains that are formed from a phosphate residue and the sugar unit deoxyribose (fig. 2.1). The phosphates are linked at the third and fifth carbon atoms of the sugar unit, which enables a clearly defined reading direction to be determined. Due to the phosphate residues, the DNA is negatively charged and surrounded by positive counterions in physiological

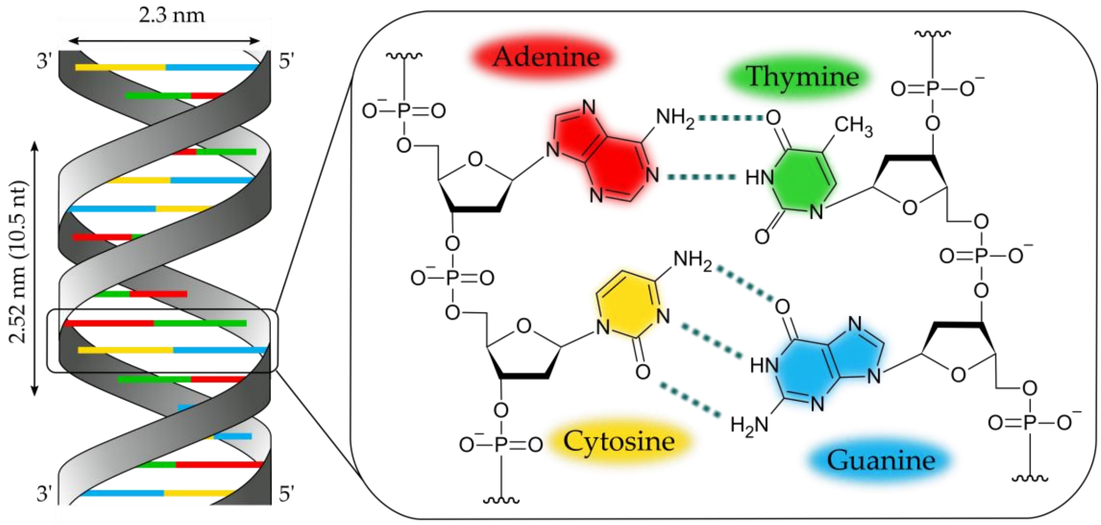

Figure 2.1 Scheme of a B-DNA and its chemical structure of the Watson-Crick base pairing. The DNA backbone consisting of the phosphate group and the sugar deoxyribose is shown in black. The four DNA bases adenine (A), thymine (T), guanine (G) and cytosine (C) are bound N-glycosidically to the sugar unit. The double-stranded character arises when the base pairs A-T and G-C interact via two or three hydrogen bonds (turquoise dotted line). One helical turn from a A-DNA consist of 10.5 nucleotides (nt) with a length of 2.52 nm and a diameter of 2.3 nm.

environment. The four different DNA bases adenine (A), thymine (T), guanine (G) and cytosine (C) are N-glycosidically bound to the sugar unit and point into the interior of the double helix. Hydrogen bonds always pair a purine and a pyrimidine base (Watson-Crick base pairing) to ensure a consistent distance between 1.8 and 2.3 nm depending on the DNA type (tab. 2.1). The adenine-thymine base pair (bp) is held together via two and guanine and cytosine via three hydrogen bonds. These interactions create double stranded DNA (dsDNA) from two complementary single stranded DNA (ssDNA).

Complementary DNA single strands enable the double helix formation from which an enthalpic gain results. Additional factors that drive the formation of the double helix are the polarity of the phosphate groups, the hydrophobicity of nucleobases and the stacking interaction of nucleobases, which provides additional stability for the DNA. The π-π interactions are particularly strong between the same nucleobases or between purine bases and can significantly alter the interaction with incident radiation. The two complementary strands are not directly opposite each other, forming a major and a minor groove with widths of a few Angström (Å), respectively [18].

Table 2.1 Overview of diameter, base distance and chirality of different types of DNA.

DNA type	diameter [nm]	base distance [nm]	chirality
B-form	2.0	0.34	right-handed
A-form	2.3	0.24	right-handed
Z-form	1.8	0.46	left-handed

In physiological environment the DNA is fully hydrated and exists in its B-form. It has a diameter of 2.0 nm and a distance between base pairs along the helical axis of 0.34 nm [19]. Lower humidity and high salt concentrations used in *in vitro* experiments change the dimensions of the DNA by forming the A- and Z-DNA [20]. The right-handed A-DNA is more compact because of a reduced number of water molecules [21]. In contrast to the A- and B-DNA the Z-DNA is left-handed and only a transient structure involved in biological reactions [22]. The diameter of the Z-DNA is 1.8 nm and has a distance between bases along the axis of 0.46 nm [23]. Under high-vacuum and high salt conditions in condense state, the DNA is likely to be present as A-DNA in the following methods (chapter 3). Taking these aspects into account, the size of the DNA in terms of a geometrical cross section (CS) σ_{geo} can be estimated from the length of the DNA sequence l and its diameter for double-stranded d and single-stranded DNA $d_{1/2}$. The calculated geometrical cross section for single σ_{SSgeo} and double stranded DNA σ_{DSgeo} and the geometrical cross section per nucleotide σ_{N-geo} is summarized in table 2.2.

$$\sigma_{geo} = l \cdot d \tag{2.1}$$

Table 2.2 Calculated geometrical cross section (σ_{geo}) from the length of the A-DNA sequence for single stranded (σ_{SSgeo}) and double stranded DNA (σ_{DSgeo}) and the geometrical cross section per nucleotide (σ_{N-geo}) [12].

Type of DNA	Number of bases/base pair	DNA length [nm]	σ_{SSgeo}/ σ_{DSgeo} [10^{-15} cm^2]	σ_{N-geo} [10^{-16} cm^2]
ssDNA	4	0.96	11.04	27.60
	8	1.92	22.08	
	12	2.88	33.12	
	16	3.84	44.16	
	20	4.80	55.20	
dsDNA	28/14	3.36	77.28	27.60

2.1.1 Overview on structural DNA nanotechnology

Today, nanotechnology in general is an established method for the production of nanostructures such as fullerenes [24], nanotubes [25] or nanowires [26] in the nanometer range. These nanostructures are used in areas such as semiconductor physics, food technology, mechanical engineering, and surface chemistry and physics.

Inspired by nature, researchers have explored nucleic acids as convenient building blocks to assemble also nanodevices and nanomachines in these small scales. It only needs four different chemical building blocks, which follow relatively simple, but with highly specific and predictable rules for base pairing at the molecular level. This makes nucleic acids by far the preferred biological material for nanometer-precise structures. DNA can be chemically synthesized as short nucleotides (nt) at low cost (< 100 nt for DNA) [19] or can be obtained from genomic DNA as longer and predefined sequence. The possibility of DNA synthesis and extraction enables the production of nanomaterials based on DNA. The first branched DNA nanomaterials were created by N. Seeman 1982 with short oligonucleotides to form immobile junctions [27] and later in 1999 four-arm holliday junction arrays [28]. Since then different DNA arrays (DNA tiles) have been created with different shapes and increasing size by introducing sticky ends on all DNA double helices [29]. Under certain conditions large 2D and 3D structures out of DNA tiles can be created. Within this method multiple reaction steps have to be done to get a high purity of a variety of short DNA oligonucleotides in a certain stoichiometry. To overcome these problems, Paul W. K. Rothemund [30] demonstrated in 2006 how to fold single stranded M13 viral DNA into arbitrary 2D and 3D shapes. The DNA origami technology was born enabling addressable surface areas and nanomechanical devices.

2.1.2 DNA origami triangle

In last two decades the DNA origami nanotechnology was well established and is now used for many different applications. Complex DNA structures in different shapes can serve as templates e.g. in the fields of biosensing [31], plasmonics [32] or enable theragnostic applications with nanorobots [33], [34]. In this work, the triangular-shaped 2D DNA origami nanostructure from Rothemund is used, because of its high stability under dry and aqueous condition and its low clustering tendency during adsorption processes.

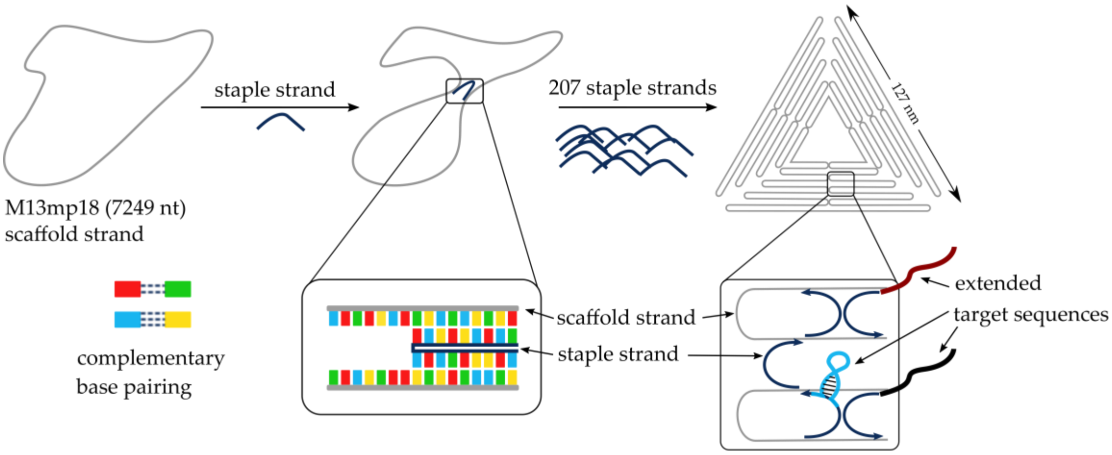

Figure 2.2 Scheme of the formation of a triangular DNA origami nanostructure and its modification with target DNA sequences according to Rothemunds DNA folding [29].

The DNA origami substrate (fig. 2.2) is a nanostructure consisting of a 7249 nt long circular M13mp18 viral DNA (scaffold strand) and 208 short artificial oligonucleotides (staple strands). Due to the Watson-Crick base pairing, the DNA strands hybridize to form e.g. a triangular DNA origami in a self-assembling process. The staple strands are complementary DNA strands and connect to at least two different positions of the scaffold strand. Only the secondary structures are dissolved by increasing temperature and the thermodynamically most favorable structure can be formed by controlled cooling. An arrangement of antiparallel helices is formed within the DNA origami structures, which are connected to their neighbours at a 180° angle via crossovers at a distance of 1.5 helix turns (~16 base pairs). The DNA origami triangle consists of three identical trapezoids, which are connected at the short ends to form a triangle with a thickness of ca. 2.3 nm and a side length of 127 nm. The formation of DNA origami nanostructures depends on the presence of positively charged counterions, which compensate the negative charge of the phosphate groups in the DNA backbone. Magnesium ions are commonly used in aqueous solution to minimize the electrostatic repulsions between the two single strands and to provide a connection to the negatively charged silicon dioxide surface, which is used for the condensed state irradiation experiments (chapter 3.3). Divalent ions are able to stabilize neighboring phosphate groups located on the same or adjacent strands. Additionally, a buffer is used that supports the stability of the DNA origami nanostructures in a physiological pH in the range of 7 to 8. Typically, a TRIS-Acetat-EDTA-buffer (TAE) is used with pH at around 8 (chapter 3.1).

Each staple strand has a unique sequence and location in the DNA origami nanostructure. Therefore, the DNA origami substrate can be used as a pegboard, where a specific staple strand can be modified and extended with the target sequence to be analyzed after electron irradiation.

2.2 Electrons

2.2.1 Timescale of Events

DNA as one of the most important cell components is a critical target for cell damage caused by high-energy radiation. It is constantly exposed not only to natural radioactivity and cosmic rays but also to artificial sources of radiation during medical treatments (chapter 2.4). Since DNA is one of the most important targets, its damage has to be studied in detail.

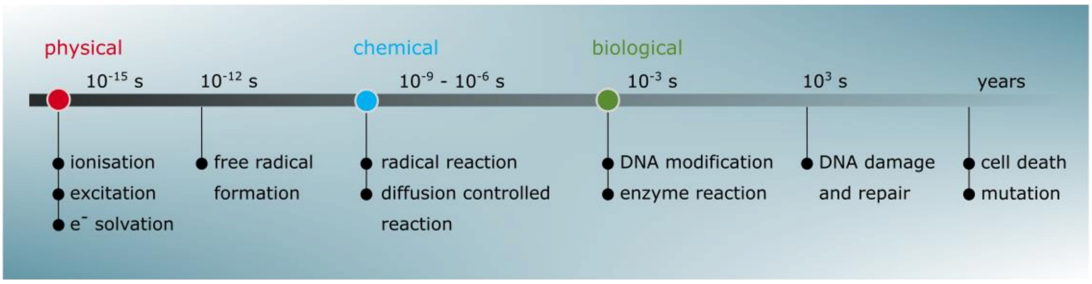

Figure 2.3 Timeline of events after irradiation of matter and subsequent reactions with DNA.

The final effectiveness of radiation to biological tissues is characterized by the linear energy transfer (LET) and describes the amount of energy deposited per length $\left(\mathrm{LET}=\frac{E}{L}\right)$. High energy electromagnetic radiation like γ rays have a low and particle radiation like α particles possess a high LET. Overall, the radiation induced processes and damage to biological tissues are very complex and can be divided in physical, chemical and biological stage with different timescales ranging from femtoseconds (fs) over seconds (s) to a whole human life (fig. 2.3). The main initial reaction step of the primary radiation (UV, X-ray, γ-ray, ion-beam) is the direct interaction with the water molecules in the cells and represents the physical stage in a femtosecond (10^{-15} s; fs) to picosecond (10^{-12} s; ps) timescale. Within femtoseconds the excitation and ionization of H_2O takes place and generates highly reactive secondary species. The ionization of water produces transiently H_2O^*, which autoionizes to form $H_2O^{\bullet+}$ and secondary electrons (SE). The $H_2O^{\bullet+}$ deprotonates directly to form $OH^{\bullet}$ and H_3O^+ or dissociates to $OH^{\bullet}$ and $H^{\bullet}$ [35].

$$H_2O + h\nu \rightarrow H_2O^+ + e^- \rightarrow H^+ + OH^{\cdot} + e^- \qquad (2.2)$$

On the one hand, the primary radiation excites directly the DNA and can initiate physical and chemical processes that are referred as *direct damage*. Ultrafast excited-state dynamics in nucleic acid experiments show that the excited-state lifetimes of DNA nucleobases are in the subpicosecond regime [36]. A strong vibronic coupling of the excited and ground state results in a fast recovery of the ground state [14]. This ultrafast photophysical process protects the DNA against UV radiation damage. Moreover, a direct electronic excitation of the DNA nucleobases can initiate the photochemical formation of cyclobutene pyrimidine dimers [37]. These intermediates are known as mutagenic and carcinogenic for skin cancer. On the other hand, the secondarily generated species that are formed by ionization of water molecules close to the DNA have a much higher influence and can induce DNA damage (*indirect damage*) of different yields, e.g. single (SSB) and double strand breaks (DSB) and base loss. Depending on the state of the various radiation-produced electrons, the overall energy of the electrons is rather small, but its damaging effect to DNA is very large and can cause about twice as much damage to the DNA as the OH radicals [38]. By ionizing water molecules with high energy primary radiation, about 80% of the energy is distributed to generate low-energy electrons with a broad energy distribution between 0 eV and 100 eV electron energy (fig. 2.4 left) [9]. Depending on the type and energy of primary radiation, the mean energy for secondary electrons is at around 10 eV [39].

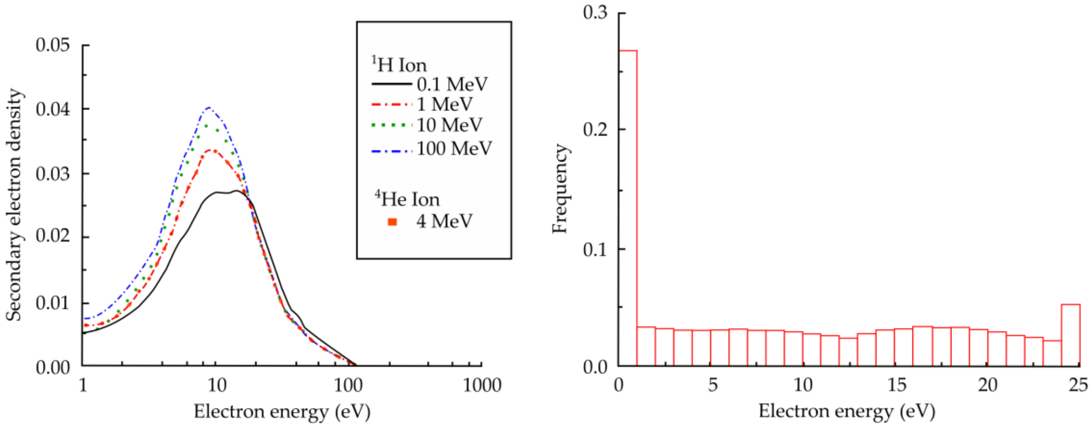

Figure 2.4 Left: Energy distribution of secondary electrons produced in liquid water by primary ionization events caused by 1H radiation of 0.1, 1, 10 and 100 MeV. Right: Frequency distribution of secondary electrons from 1 MeV electron irradiation with the highest fraction between 0 and 1 eV kinetic energy of about 27%. Diagram reprinted with permission from ref. [9].

The produced free electrons can induce further reactions depending on their energy and their state of solvation. Secondary electrons (SE) lose energy to form LEE, quasi-free electrons (e^-_{qf}), prehydrated electrons $\left(e^-_{pre}\right)$, which are fully solvated within ps to form solvated electrons (e^-_{sol}) [40].

If the energy of SE exceeds the ionization energy IE of the nucleobases (~8 - 9 eV) ionization processes can occur [41]. Ionization of DNA components are threshold processes and can cause DNA strand breaks (SB) that are less effective compared to resonant processes. One of these resonant processes is described by the dissociative electron attachment mechanism of LEEs with electron energies below 10 eV. Such LEEs can cause single and double strand breaks through DEA in the DNA. Quasi-free electrons (e^-_{qf}) have energies close to 0 eV and can rupture sugar-base bonds via bond elongation through a barrier-free glycosidic bond cleavage [42]. The pre-hydrated electrons (e^-_{pre}) are partly hydrated and become fully dissolved within ps to become solvated electrons (e^-_{sol}), which are then chemically rather inactive [43]. Before (e^-_{pre}) are completely thermalized DEA can take place within 10^{-14}-10^{-10} s (chapter 2.2.3). Solvated electrons can still bind efficiently to nucleobases, but are known to not cause DNA strand breaks [44].

The second stage is the chemical stage and is defined by the diffusion-controlled reactions that take place within nanoseconds (10^{-9} s; ns) to milliseconds (10^{-6} s; ms). It is also governed by DNA single and double strand breaks induced by hydroxyl radicals with less effect compared to the generated electrons.

The slowest classification on the timescale is the biological stage and can extend over the whole human lifetime. DNA damage and modifications trigger biological processes, like subsequent enzyme reactions with the aim to repair the DNA. By using the complementary DNA strand as a template, e.g. single strand breaks, inter- and intrastrand crosslinks (ICL), mis-matches and base losses can be repaired very easily by enzymes (fig 2.5). In the case of a double strand break, a missing or faulty repair of the DNA lesion leads to mutations or cell death, which is on the timescale of hours. Mutations can have different possible consequences, ranging from inheritable diseases to cancer.

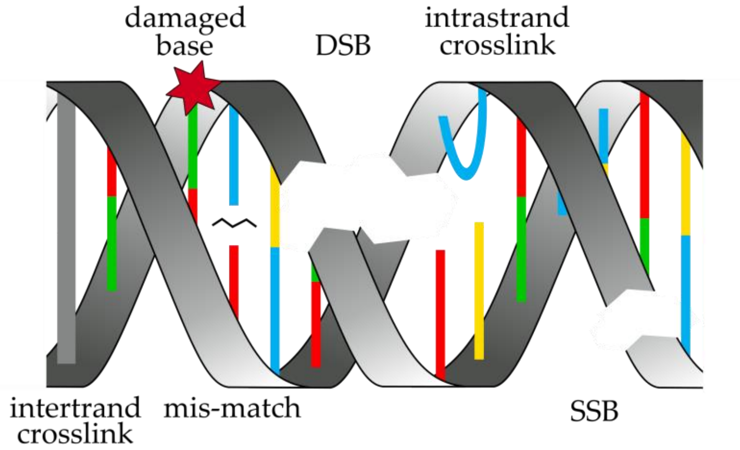

Figure 2.5 Formation of general damage forms that can occur at a DNA strand.

2.2.2 Electron-molecule scattering

In classical physics, interactions of free electrons with different types of matter (atoms, molecules, clusters, condensed matter) is divided into resonant and direct scattering. Latter includes elastic and inelastic scattering. During elastic scattering the kinetic energy can only be transferred between the collision partners. Thereby the internal energy and kinetic energy is preserved. If inelastic scattering takes place, the internal energy and kinetic energy of the collision partners can be decreased or increased due to excitation or de-excitation (translational or internal degrees of freedom). In non-polar molecules the transfer of energy via translation or rotation and vibration is very inefficient due to the low mass of the electron. The following equations describes the interaction of a neutral molecule AB and an electron e of a specific potential ϵ (eq. 2.13).

$$AB +\ e^{-}(\epsilon_1) \rightarrow AB + e^{-}(\epsilon_2) \qquad \epsilon_1 \approx \epsilon_2 \tag{2.3}$$

$$AB +\ e^{-}(\epsilon_1) \rightarrow AB^{*} + e^{-}(\epsilon_2) \qquad \epsilon_1 > \epsilon_2 \tag{2.4}$$

When an energetic electron collides with an atom or molecule transferring enough energy to eject an electron from the target particle, the process is called electron ionization (EI). The electron acts primarily as a projectile with kinetic energies above the ionization energy of the target partner to provide the energy.

$$AB +\ e^{-}(\epsilon) \rightarrow AB^{*+} + 2e^{-} \quad \epsilon > IE \tag{2.5}$$

If a free electron with a kinetic energy of around 2 eV hits a particle, it takes about 10^{-15} s (1 fs) to travel 10^{-9} m (1 nm), equivalent to about 7 bond lengths when assuming a C- C bond length of about 150 pm [45]. Even for large molecules a free electron does not need more than a few fs to pass the whole molecule. Whereas, molecular motions like translational thermal motion (10^{-11} s for travel distance of 1 nm at velocities of 100 m/s) or vibrations (10^{-14} s with frequencies of 10^{14} Hz) occur at much longer timescales. In view of that, the molecule is in a stationary state while the electron attaches via electronic transition from one vibrational energy level to another with a significantly overlapped wave function (vertical Frank-Condon-Principle). Due to the different mass of nuclei and electrons, there are no changes in the positions of the nuclei in the molecular entity and its environment (Born-Oppenheimer-Approximation).

In contrast to direct scattering, resonant scattering can also occur at very low and specific energies. Only a specific amount of energy can be absorbed by the molecule, what is given by the energy difference between the neutral and anionic state within the Franck-Condon region. Hence, resonances are characterized by sharp changes in cross sections (chapter 2.2.4) with energy, and by transit times exceeding the normal duration for passing the target particle. If an electron attaches to a neutral molecule to occupy a formerly unoccupied molecular orbital (MO) the negatively charged transition state is referred to as transient negative ion (TNI).

The formation of a TNI can be classified into single particle (1p) resonances *(shape resonance, vibrational Feshbach resonances)* and two particle resonances (2p1h) *(core excited shape, core excited Feshbach)*. In the first case a single particle attaches to the target molecule and excites only vibrationally, then it is called *shape resonance*, because it depends on the centrifugal barrier and thus on the shape of the interaction potential [46]. The interaction between the incoming electron and the target molecule is dominated at small distances by the repulsive centrifugal potential from the angular momentum of the electron, while at large distances the attractive potential is dominating. In total, the sum of both potentials is crucial if the electron is trapped temporarily in the potential or not. The incoming electron is occupying a virtual MO and the electron configuration of the target molecule is unchanged. It usually occurs below 4 eV with short lifetimes of 10^{-15} to 10^{-10} s [47]. Compared to that, the *vibrational Feshbach resonance* lies below the neutral ground state and thus has a positive electron affinity (EA). The electron attachment is accompanied by rearrangements in the electronic structure which hinders autodetachment (AD) (chapter 2.2.3) and the lifetimes are extended about 10^{-6} s [48]. If the excited state is close to the ground state of the neutral molecule, *vibrational Feshbach resonances* appear at energies close to 0 eV.

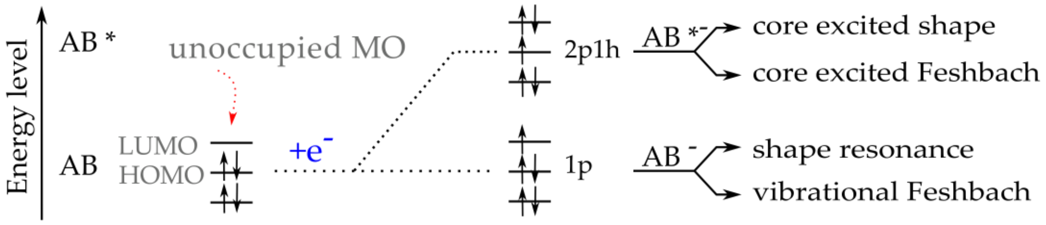

Figure 2.6 Illustration of the TNI formation and its classification into two particles one hole 2p1h (core excited shape and core excited Feshbach) and single particle resonances 1p (shape resonance and vibrational Feshbach).

In contrast to that, the 2p1h resonance includes the attachment of two electrons with higher electron energy by generating an electron hole (fig. 2.6) and is divided into *core excited shape* and *core excited Feshbach resonance*. Unlike in the one particle resonance, in the 2p1h resonance, two electrons are occupying a formerly virtual MO and a hole is generated. If the generated TNI is energetically above the corresponding electronically excited neutral molecule it is referred to as *core excited shape* resonance. When the TNI lies below the electronically excited neutral molecule, AD is not accessible and it can just relax by rearranging the electronic structure through a two-electron transition into lower excited states. This extends the lifetime compared to the shape resonance and is referred to as *core excited Feshbach resonance*.

The resonance lifetime is usually longer than 1 fs, because the electron is not only spending the transit time in the vicinity of the molecule, the attached electron is trapped by the target molecule. The lifetime of the resonances is dependent of the molecule size with its electronic structure, the surrounding medium of the molecule and the electron, the attaching electron energy and its internal energy. Therefore the lifetime of a resonance can range from times corresponding to short vibrational periods (10^{-14} s) [49], over microseconds (10^{-6} s) in larger molecules [50], up to some milliseconds (10^{-3} s) [51]. The attachment of an electron generates a transient anionic state by resonant transitions from the neutral molecule AB to an anionic state at specific energies below its ionization threshold according to the following equation.

$$AB + e^-(\epsilon_1) \rightarrow AB^{\#-} \qquad (2.6)$$

The index "#" represents the transient negative ion (TNI) [52].

In contrast to EI, the TNI is a one particle intermediate state, where the excess energy from the electron cannot be transferred into kinetic energy and is stored as potential energy. The consequence is that the entire kinetic energy and electron affinity is stored in the TNI, resulting in resonances rather than a threshold process. The TNI has a finite lifetime and can decay via non-radiative stabilization processes. It can either decay back into the neutral parent molecule under loss of the electron (AD), be stabilized (associative attachment; AA), lose the excess energy by emitting a photon (radiative stabilization; RS) or fragment into a negative ion and a neutral product (DEA). The TNI is in general unstable against autodetachment [53], what implies the loss of the additional electron of the TNI. This process describes the counter reaction to the attachment of the electron and follows the vertical Franck-Condon principle and is accessible until the crossing point R_C of the potential curves (chapter 2.2.3).

$$\textbf{AD:}\ AB^{\#-} \rightarrow AB^* + e^-(\epsilon_2) \qquad \epsilon_1 > \epsilon_2 \qquad (2.7)$$

When the TNI is generated in a vibrational excited state of the anion, the neutral molecule AB is left in an excited state AB^* after AD. The detached electron lost some kinetic energy referred to the vibrational energy and can be measured, which is done in electron energy loss spectroscopy (EELS). The lifetime of the autodetachment τ can be calculated by the energy linewidth Γ of the anion state according the Heisenberg uncertainty principle and the reduced Planck constant ħ

$\left(\frac{h}{2\pi} = 6.58 * 10^{-16} eVs\right)$. According to equation (2.8) we are getting the shortest lifetime with the broadest linewidth.

$$\tau \approx \frac{\hbar}{\Gamma} \qquad (2.8)$$

The excess energy can also be converted by intramolecular vibrational energy redistribution (IVR). Here, the anionic state relaxes into the potential minimum, which is below the potential minimum of the ground state. This is common in Feshbach resonances, where the crossing point of both potential curves is close to 0 eV excess energy. To stabilize the TNI it has to lose some of its excess energy via collision with adjacent molecules in the environment.

$$\textbf{AA: } AB^{\#-} + AB \rightarrow AB^{*} + AB^{-} \qquad (2.9)$$

The process with the lowest contribution is the RS and is as well the slowest mechanism. A photon $h\nu$ is emitted by the charged molecule to lose the excess energy of the excited state resulting in a stabilized anion.

$$\textbf{RS: } AB^{\#-} \rightarrow AB^{-} + h\nu \qquad (2.10)$$

The most important process that competes with both other processes (AD and AA) is dissociation into a stable anion and a neutral radical. This reaction describes a bond cleavage, which is favored when the extra electron is occupying a MO with an antibonding character. It is the main reaction step when talking about a DNA bond breakage.

$$\textbf{DEA: } AB^{\#-} \rightarrow A + B^{-} \qquad (2.11)$$

The timescale of DEA reactions is in the order of 10^{-14} to 10^{-12} s and DEA competes with AD, which occurs in the same timescale [53].

2.2.3 Dissociative electron attachment (DEA)

Figure 2.7 shows a two-dimensional potential energy diagram for the formation of a TNI via a single particle shape resonance. When an electron attaches to a molecule, the excitation energy E necessary to form the TNI corresponds to the vertical electron affinity (EA) of the molecule. As described in the chapter 2.2.2, the adiabatic EA is defined as the energy difference between the neutral molecule and the anionic state in their electronic, rotational and vibrational ground state. If the EA is positive, the ground state of the anion lies below the ground state of the neutral molecule and per definition a thermodynamically stable anion is formed. To form the TNI, the vertical attachment energy (VAE) is needed and describes the energy difference between the neutral ground state and the lowest unoccupied MO (LUMO) or higher orbital of the anionic state. As a competitive process, the AD describes the reverse process of the vertical attachment process. After passing the crossing point R_C the excited state reaches the ground state of the anionic state and a negative and a neutral fragment is generated. To allow the relaxation beyond R_C, the lifetime of the TNI must be long enough. After this point, only AA and DEA are the possible reaction pathways. The dissociation energy $BDE(A-B)$ of the bond A-B and $EA(B)$ the electron affinitiy of B yield the thermochemical threshold ΔH_0.

$$\Delta H_0 = BDE(A-B) - EA(B) \tag{2.12}$$

In experiments ϵ is measured which is composed of the thermochemical threshold and the excess energy E^* in form of translational and internal energy of the fragments.

$$\epsilon = BDE(A-B) - EA(B) + E^* \tag{2.13}$$

The so formed negative fragment can re-eject its extra electron, for which the vertical detachment energy (VDE) is needed.

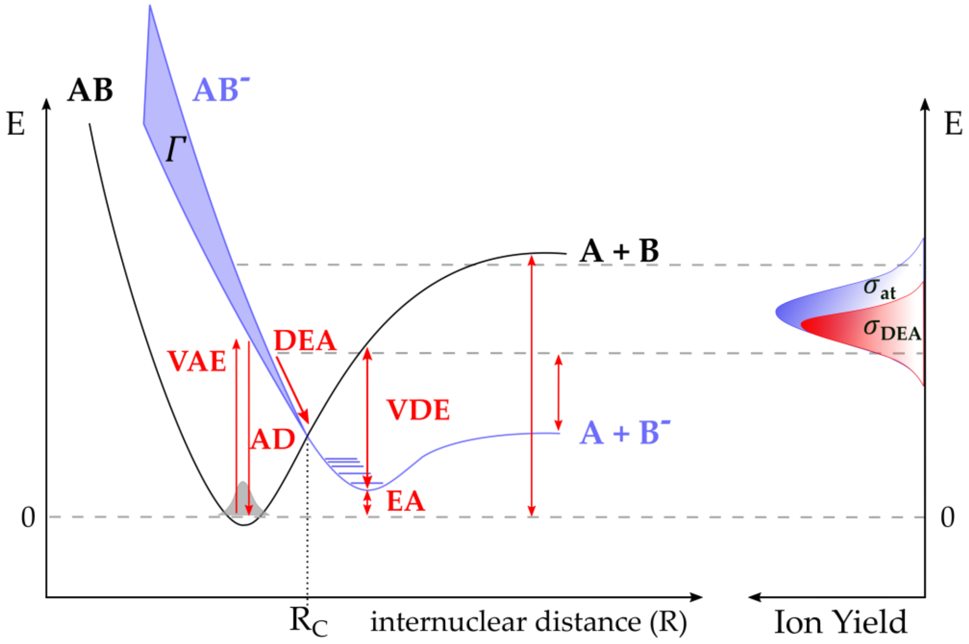

Figure 2.7 Schematic two-dimensional potential energy diagram illustrating the formation of a transient negative ion. The ion yield on the right side reflects the initial Franck-Condon transition.

2.2.4 Cross section (CS)

The cross section σ is a function of the impact energy E where a number of reactions N_R per projectile particle N_P in a given area Z with a specific number of targets N_T occurs. The cross section is given in cm² and thus simply describes an area.

$$\sigma_{\mathrm{tot}} = \frac{N_{\mathrm{R}} \cdot Z}{N_{\mathrm{P}} \cdot N_{\mathrm{T}}} \tag{2.14}$$

In other words, σ describes in general the probability that a certain interaction occurs; here this is a scattering process between an electron and the target atoms or molecules. Including all scattering interactions like elastic scattering σ_{el}, ionization σ_{ion}, excitation σ_{ex} and electron attachment σ_{at} gives the total cross section σ_{tot}.

$$\sigma_{\mathrm{tot}} = \sigma_{\mathrm{el}} + \sigma_{\mathrm{ion}} + \sigma_{\mathrm{ex}} + \sigma_{\mathrm{at}} \tag{2.15}$$

During DNA radiation damage (chapter 2.3) the DEA process is a pivotal process occurring between DNA and LEEs. The effectivity of a DEA process can be expressed by the DEA cross section σ_{DEA}. It can be calculated from σ_{at} and the probability P that the TNI dissociates, where P is a survival probability of the formed TNI.

$$\sigma_{\mathrm{DEA}} = \sigma_{\mathrm{at}} \cdot P \tag{2.16}$$

If the extra electron is not auto detached until the dissociating system has reached the crossing point R_{C}, the system can no longer return to its ground state again and will dissociate. R represents the bond distance between two atoms from where the bond dissociation takes place. The dissociation is favored by a stable TNI, since R_{C} is usually reached within a vibrational period in tens of femtoseconds (10^{-14} s for a vibration). Therefore P can be calculated from the time τ_{DEA} the TNI needs to dissociate and the autodetachment lifetime τ_{AD}.

$$\sigma_{\mathrm{DEA}} = \sigma_{\mathrm{at}} \cdot e^{-\frac{\tau_{\mathrm{DEA}}}{\tau_{\mathrm{AD}}}} \tag{2.17}$$

2.3 DNA radiation damage

2.3.1 DNA Radiation stability and damage by LEEs

The DNA is subject to many endogenous and exogenous insults that affect the DNA replication and transcription. Radiation damage to DNA comprises complex molecular mechanisms of physical, chemical and biological events that are not completely understood yet. Especially DNA double strand breaks are one of the most severe forms of DNA damage and must be detected by enzymes [54] and repaired afterwards to prevent cell death [55]. For a long time, it was expected that only photons and electrons above the ionization threshold of molecules contribute to the damage of biological tissue. However, many scientific studies have proven the opposite, i.e. electrons below the ionization threshold can cause a considerable amount of damage via DEA to the DNA in the cell nucleus. The initial events of energy deposition and production of SE within the chemical stage determines the effectivity of DNA strand cleavage. Hence, it is crucial to investigate low energy electron interaction with DNA and the surrounding molecules that occur at an early time of radiation damage.

DNA as the main target of radiation damage is packed to chromosomes surrounded by water and various ions in the cell. Inside of the chromosomes, the DNA is stacked by hydrogen bonds to double helices, bundled with proteins to complex structures. Due to the many different biologically relevant systems, different methods for LEE-induced DNA strand breaks have to be developed. Various methods have been established in research that allow access to different DNA radiation damage. The usage of complex biologically relevant systems like animals or cells yields important, but limited information [56]. In comparison to biological systems, the study of idealized model systems like DNA subunits in the gas phase, prohibits the information of the biological relevance and is limited by the molecule size in the gas phase. Instead, detailed fragmentation mechanisms under specific irradiation conditions can be studied. A large gap in the information about DNA damage between the analysis of small molecules such as DNA subunits and the greater molecules such as cells is present. Due to the low penetration depth of LEEs, there is a need for highly sensitive physico-chemical experiments to quantify LEE-induced strand breaks. For this purpose, several methods have been developed that try to close this gap. Previous studies used supercoiled plasmid DNA with several thousand base pairs and irradiation with LEE. After irradiation the supercoiled DNA changes its conformation from supercoiled (undamaged) over circular (SSB) to longer linear (DSB) and shorter linear (MSB; multiple strand breaks) fragments [57]. The DNA strand breaks can be analyzed with agarose gel electrophoresis (AGE) [58]. Gas phase experiments of isolated DNA components show a similar energy dependency in the resonance behavior as for the SSB and DSB yields in the condensed phase (fig. 2.8). Both in gas and condensed phase all nucleobases undergo DEA within two resonant features at higher energies between 6 and 12 eV [58] and at very low energies between 0 and 4 eV [59].

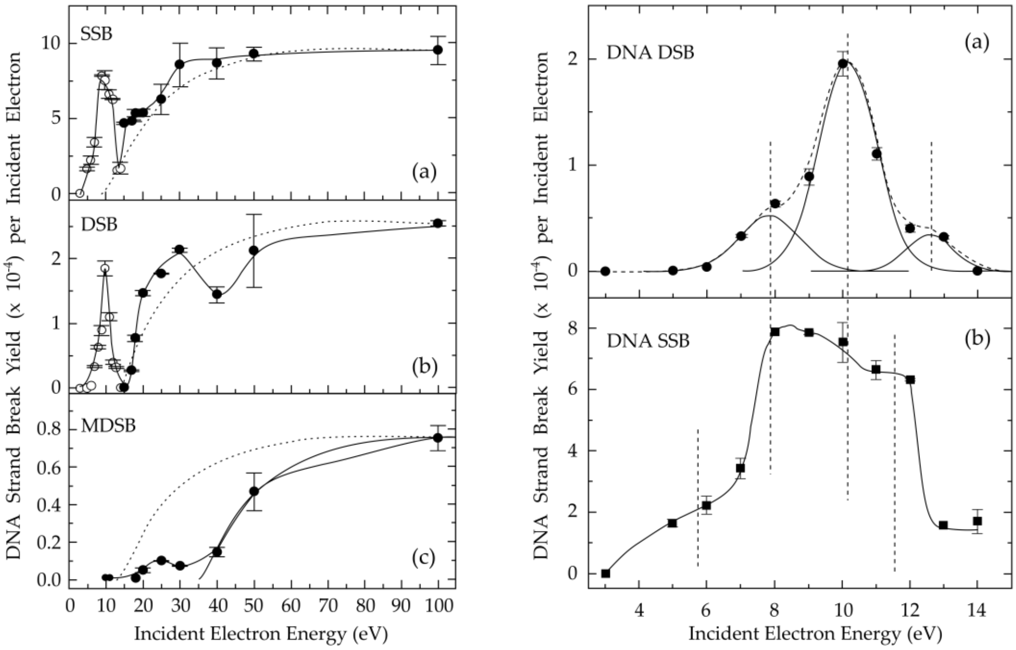

Figure 2.8 Left: Quantum yields per incident electron for SSB (a), DSB (b) and MDSB (c) in DNA films by LEEs as a function of incident electron energy between 0 and 100 eV. Right: DSBs (a) and SSBs (b) in dependence of the incident electron energy below 15 eV. A strong anionic resonance at 10 eV for DSBs and a broad resonance maximum between 7 and 13 eV for SSBs is observed. Both images are reprinted with permission from ref. [56].

The study with supercoiled plasmid DNA does not yield any specific information about sequence dependences, the influences of secondary structure or the enhanced effect of DNA modification with radiosensitizers. Consequently, it is advantageous to use shorter oligonucleotides with specific sequence in which also radiosensitizers can be incorporated. With the help of high-performance liquid chromatography (HPLC) sequence-specific strand breaks in short oligonucleotides up to tetramers can be studied [60]. Going to higher numbers of nucleotides, the detection limit of HPLC is reached. For longer oligonucleotides, fluorescence spectroscopy with self-assembled monolayers (SAM) of well-defined DNA oligonucleotides can give on the one hand results on DNA strand breakage, but is on the other hand limited to DNA single strands [61]. To close the information gap, a novel approach was established in 2012 and is based on Atomic force microscopy (AFM) analysis of well-defined oligonucleotides attached to DNA origami templates [10] (chapter 3.1). This method allows to determine effective and absolute CS for DNA strand cleavage and to study the effect of tumor therapeutics.

2.4 Cancer therapy

Interaction of radiation with matter is always present and can have a different outcome. Depending on the energy, type and dose of radiation, it can be harmful for the human body leading to DNA mutations and cell death. In addition to natural cosmic radiation, we also expose ourselves to artificial radiation, such as in radiotherapy. It is one of the three traditional cancer therapy methods (in addition to surgery and chemotherapy) with the aim to kill malignant cells. Half of the patients diagnosed with cancer are treated at least once with radiotherapy [62]. During hadron therapy the cancer cells and surroundings are illuminated with megaelectron volt (MeV) proton radiation to treat the cancer cells in a highly selective way [63], [64], [65]. The penetration depth and thus the effectiveness can be changed by varying the energy and its dose rate. A fast and charged particle ionizes atoms of the material when moving through matter and deposits a dose along its path. When plotting the energy loss of this particle during its travel, a peak occurs called Bragg peak. The Bragg peak occurs just before the particle speed is down to zero, because the energy loss of charged particles is inversely proportional to the square of their velocity [66]. Whereas ions can penetrate up to 30 cm deep into the tissue, photons lose too much of their energy to the surrounding tissue on the way to the tumor and are most effective at a depth of approx. 3 cm [67]. Depending on the type, size and location of the tumor and also the constitution of the patient, each radiation therapy is adapted to the patient. The deposition of a certain amount of radiation into matter induces different types of reactions depending on the type and energy of radiation. The DNA in the cell nucleus can be damaged *directly* and *indirectly* as described in chapter 2.2.1. Treatment with radiation affects healthy and malignant tissues, but the sensitivity can be increased towards tumor cells. A combination of chemo- and radiotherapy can increase the DNA radiation damage by using tumor therapeutics administered at the same time, which show an additive effect in combination with radiation. Since cancer cells have a faster metabolism and a higher nutrient uptake than healthy cells, these cells tend to accumulate the drug. Whereas, the most common clinically applied therapeutics are DNA intercalators and halogenated nucleosides. There are various DNA binders like platin (Pt) based drugs or small planar aromatic molecules, which bind noncovalently to the DNA and interrupt natural biological functions. The halogenated nucleotides, especially the fluorinated therapeutics, have proven to be another chemotherapeutic with enhanced radiosensitivity of hypoxic cells [68].

2.4.1 Fluorinated Radiosensitizers

DNA has a well-organized secondary structure and every change in molecule structure can vary the DNA conformation. For this reason, chemotherapeutics must be similar in structure to the usual DNA components in order to be integrated into the natural DNA. In medical studies, the fluorinated nucleosides *Fludarabine* (F- ara) [69], 5-*Fluorouracil* (^{5F}U) [70] and *Gemcitabine* (Gem) [71] are one of the main chemoradiotherapeutic drugs.

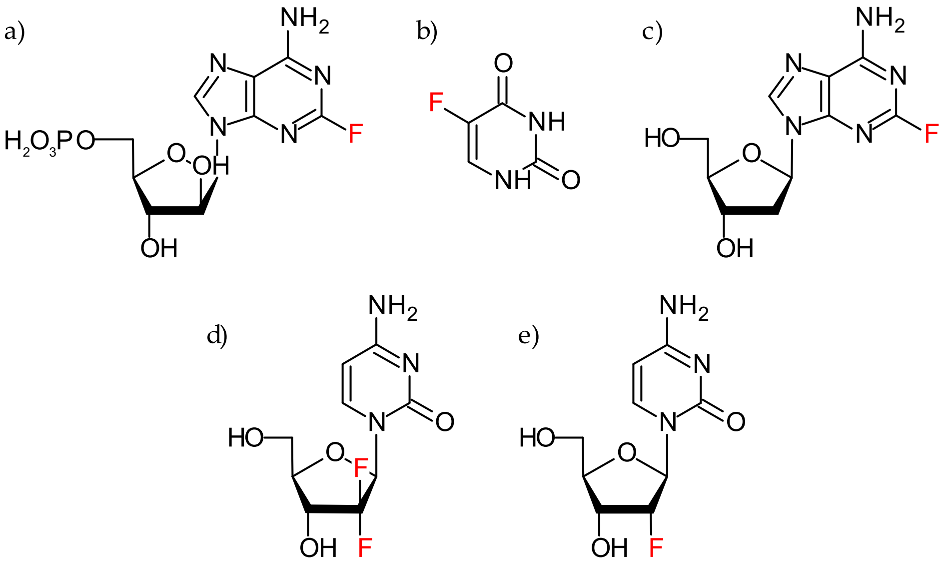

Figure 2.9 Chemical structures of a) Fludarabine (F-ara), b) 5-Fluorouracil (^{5F}U), c) 2- Fluoroadenosine (^{2F}A) see chapter 4.4, d) Gemcitabine (Gem) and e) 2'-fluoro-2'-deoxycytidine (^{dF}C).

The fluorine substitutions mimic uptake and metabolism of natural nucleosides, but ultimately cause cell death [72]. As fluorine (F) is the second smallest atom, it can simply be substituted for hydrogen (H) or hydroxyl group (OH) on the nucleobase or sugar unit and imitate them. With attaching an F atom to the 2'- or 3'-position of the sugar unit, the chemical stability in an acidic environment is increased [73]. Fluorinated nucleosides are considered as good electron scavengers due to the fluorine atom with its high electronegativity (electrophilic). After intracellular uptake, the effect of these radiosensitizers is the inhibition of DNA replication by various reaction mechanism. Gemcitabine in particular is metabolized to active mono-, di- and triphosphate and is incorporated into the DNA competitively to deoxycytidine triphosphate [68], [74]. Using low-energy electrons close to 0 eV, it was shown that mainly the N-glycosidic bond is cleaved and the remaining anions are stabilized by the fluorine substitution on the sugar unit [75]. Moreover, DNA is stabilized by hydrogen bonds, with F being a good hydrogen acceptor and forming a strong C-F bond.

Fluorouracil (^{5F}U) is a listed (WHO) anti-cancer drug for over 60 years [76]. It is a thymidine synthase inhibitor by stopping the 5'-C-methylation of 2'-deoxyuracilmonophosphate to 2'-deoxythyminemonophosphate. Since the conversion is blocked, the DNA replication is inhibited and the accumulation of cells in the early S phase of the cell cycle is prevented [68]. The much greater effect of ^{5F}U comes from preventing DNA double strand break repair, which usually leads to cell death.

In addition, *Fludarabine* (F-ara) is one of the most important anti-cancer drug with an arabinose sugar unit [69]. It is a water-soluble prodrug and can be easily transported into the cell, where it is then activated by the deoxycytidine kinase to the triphosphate derivative. Further, they can incorporate into newly synthesized DNA resulting in chain termination. After activation it inhibits DNA synthesis by inhibiting DNA polymerase, DNA ligase, DNA primase and ribonucleotide diphosphate reductase [77]. The modification of F-ara to *Clofarabine* (Cl-ara) is a new-generation nucleoside analog with stronger enzyme inhibition and longer intracellular retention for acute lymphoblastic leukemia [78]. The phosphorylation of Cl-ara by deoxycytidine kinase in the cell is substantially more efficient than that of F-ara and results in more efficient cell death by blocking the DNA synthesis [79].

Halogenated nucleobases show intense DEA resonances at various electron energies in the gas phase, but it is inherently difficult to investigate the influences of halogenated nucleobases on the DNA strand breakage towards electron energies in which DEA can take place. Therefore, the DNA origamis are used as platforms to introduce halogen modified DNA nucleotides, which are examined towards low-energy electron induced DNA strand breakage. In DEA studies with DNA building blocks a transfer mechanism of the excess charge from the nucleobase to the DNA backbone was proposed [80]. Calculations on cytosine nucleotide predict a coupling of the π^* orbital of the cytosine with a σ^* orbital of the deoxyribose phosphate C-O bond [81]. This means, that an electron captured by the nucleobase causes a strand break between the sugar and the phosphate group (fig. 2.10). However, the reaction rate of the DNA strand break induced by the electron deposition in the π^*orbital in the base is rather low compared to autodetachment. Therefore, electron attachment directly to the DNA backbone is more likely and more effective at very low energies [82]. The investigation of vertical and adiabatic potential surfaces of water solvated 5′- thymidine monophosphate anions suggest strand breaks by directly electron attachment to the phosphate group [83].

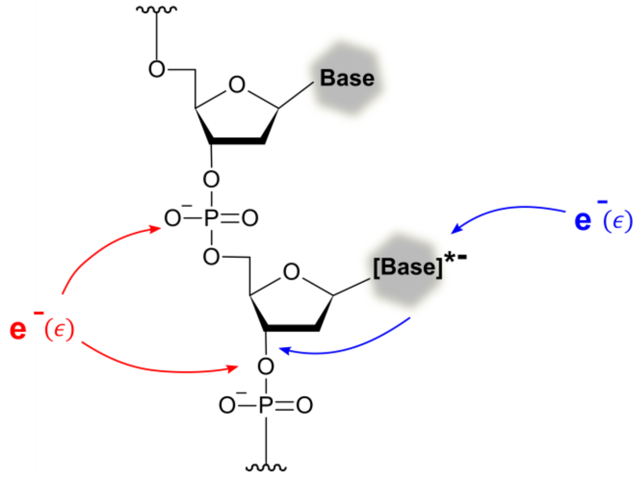

Figure 2.10 Single stranded DNA containing two arbitrary nucleobases. A possible DNA single strand break can either be induced by a low energy electron captured directly by the backbone (red) or by attachment to the nucleobase (blue) with subsequent charge transfer to the C-O bond in the backbone.

Therefore, a radiosensitizer with a modification close to the C-O bond in the DNA backbone is beneficial. Both, ^{5F}U and F-ara are fluorine substituted nucleotides with modification on the DNA base. For this reason, radiosensitizers such as *Gemcitabine* (2',2'-difluoro-2'-deoxycytidine) have been developed that have the fluorine substitution directly on the deoxyribose in the DNA backbone (fig. 2.9d). Gem is actually used as a medication to treat breast, ovarian, non-small cell lung, pancreatic and bladder cancer [71] without tissue irradiation. Hydrophilic Gem is transported into cells for nucleosides and is then catalyzed by the enzymes to gemcitabine triphosphate and can mimic deoxycytidine triphosphate [84] to inhibit the DNA reproduction [85]. However, it can also be used as radiosensitizer and cell toxic agent in medicine [86]. It has become the standard treatment choice for locally advanced and metastatic pancreatic cancer [87]. In this work 2'-fluoro-2'-deoxycytidine (^{dF}C) was used (fig. 2.9e) as a Gem analogue. In contrast to Gem, ^{dF}C is singly fluorinated on the deoxyribose sugar. Additionally, it can be easily introduced into customized DNA oligonucleotides and therefore be investigated by the DNA origami technique.

2.4.2 DNA binders

The DNA can directly harmed by ionizing radiation, where two thirds of the DNA radiation damage is caused by secondary species (*indirect damage*) generated through the radiolysis of water molecules in the cells [88]. A variety of experiments, like gas phase DEA setups and condensed phase with DNA monolayers on gold surface [89], DNA building blocks and plasmid DNA [90] and well known DNA single and double strands attached to DNA origamis nanostructures [10] show the major DNA damaging effect of generated LEEs. In addition to LEEs, singlet oxygen $^1O_2$ [91], the first excited electronic state of molecular oxygen $^3O_2$, is a significant molecule studied in organic synthesis, due to its characteristic oxygenation reactions. Its key role in cell death mechanisms led to its use in photodynamic therapy (PDT) for several types of cancer and other disease. Cancer cells are often hypoxic in comparison to healthy oxic cells, which results in a lower sensitivity to ionizing radiation than normal tissue [92]. Hypoxic cells are characterized by a low level of oxygen with less amount of $^1O_2$ during the irradiation in PDT [93]. PDT is a method for the treatment of tumors and other tissue changes such as new vascular formations with light in combination of a light-activated substance, named as photosensitizer (PS), and oxygen present in the cell. The high concentration of oxygen in air is a perfect source that can be excited to the reactive singlet state. Therefore, the concentration of oxygen in the cells is increased by exposing oxygen-rich air to the patient before radiation treatment. Generation of singlet oxygen in a controlled manner presents some challenges because of the highly forbidden electric dipole process. *Tørring et al.* studied the generation, lifetime and reactions of singlet oxygen with DNA based systems on DNA nanostructures by selectively controlling the generation of $^1O_2$ [94]. The authors placed a DNA oligonucleotide attached to a porphyrin-based PS on a DNA nanostructure to convert $^3O_2$ to $^1O_2$ upon UV-Vis irradiation. Attaching a complementary DNA strand modified with a quencher can effectively quench the production of singlet oxygen.

Many PS have been synthesized to target the DNA grooves for the use in medically approved PDT. The photodynamic therapy is suitable for large and deep tumors in the human body and relies on the bioavailability of PS with photophysical, chemical and biological properties such as non-toxicity to induce cellular and tissue effects, water solubility and a high DNA groove binding affinity. The photocytotoxicity of DNA binding agents especially against cancerous cells is due to the transformation from its singlet ground state into a relatively long-lived excited triplet state by light absorption. During its lifetime it can undergo direct reaction with a substrate, such as cell membrane components or DNA compounds to form radicals. Alternatively, the excited triplet state can be quenched by triplet oxygen $^3O_2$ forming $^1O_2$ by energy transfer. The highly reactive radical is formed close to the light absorbing PS and the biological response to the PS evolves only in those areas of tissue that have been exposed to radiation. This aspect accounts for less side effects of PDT than those of other chemotherapies. The right choice of the PS is of great importance, since the formation of the reactive oxygen species and the binding to the DNA grooves within the cells must be ensured. *Ray et al.* investigated the light-induced oxidative damage of DNA origami nanostructures by coupling photoactive C_{60} to the DNA [95]. They covered the DNA nanostructures with C_{60} aqueous solution and observed a morphology change of the substrates upon visible light irradiation via time-laps AFM imaging. By using the DNA origami technique, the damaging effect of PS can be examined on single and double stranded DNA in aqueous solution and in dry state (chapter 4.6). In the present work, two photosensitive DNA anthracene derivatives (non-planar (ANT994) [96], [97], [98] and planar (ANT1083) 9,10- methylpyridiniumanthracene derivatives) and a chromium-(III)-complex ($[Cr(ddpd)_2][BF_4]_3$ (ddpd = N,N′-dimethyl-N,N′-dipyridin-2-ylpyridine-2,6-diamine) [99], [100], [101]) are examined to observe its damaging effect to DNA oligonucleotides (fig. 2.11).

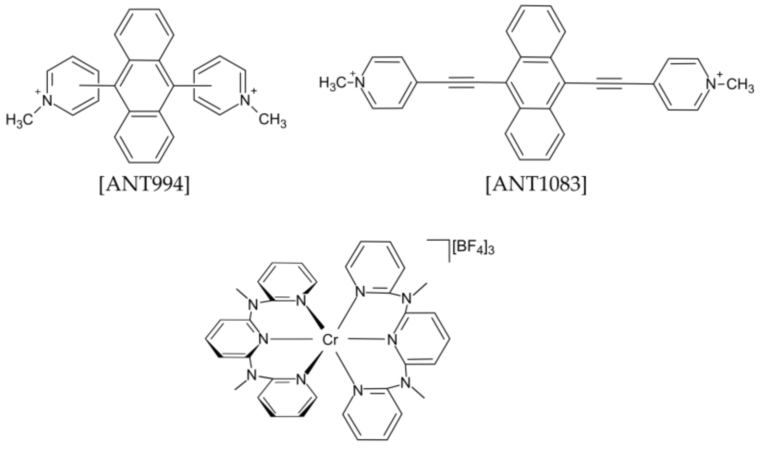

[ANT994]

[ANT1083]

$[Cr(ddpd)_2][BF_4]_3$

Figure 2.11 Molecular structures of the DNA binders a) [ANT994], b) [ANT1083] and c) $[Cr(ddpd)_2][BF_4]_3$.

3 Determination of LEE induced strand break cross sections by AFM

The combination of DNA origami nanostructures with AFM analysis [10] allows electron irradiation experiments of single and double stranded oligonucleotides with a maximum of 20 – 30 nucleotides at specific electron energies. Chapter 3 describes the experimental details of the sample preparation of DNA origami nanostructures (chapter 3.1), the irradiation setup in a high vacuum chamber (chapter 3.2), the irradiation procedure (chapter 3.3) the imaging via AFM (chapter 3.4) and the evaluation and comparison of manual and software analysis (chapter 3.5).

3.1 Sample preparation

The preparation of the DNA origami triangle is a one pot synthesis in a self-assembly process. A stock solution is prepared by mixing 3 µL of each of the 206 staple strands (*metabion GmbH*, HPLC purity) having a concentration of 100 nM. For the DNA origami preparation, 30 µL of stock solution, 5 µL of 100 nM viral scaffold strand (M13mp18, *tilibit nanosystems GmbH*) and 10 x TAE (TRIS(0.4 M)-Acetate(0.2 M)-EDTA(0.01M))-buffer with 150 mM $MgCl_2 \cdot 6\ H_2O$ (*Sigma-Aldrich*) are added to 55 µL of deionized water (purified with a *MilliQ*). TRIS is known as tris(hydroxymethyl)aminomethane and the hexadentate ligand EDTA as ethylenediaminetetraacetic acid. The stock mixture with a total volume of 100 µL is heated up to anneal from 80 °C in a stepwise manner over 2 h to 6 °C with a 5-Prime thermocycler (*Techne*). Subsequently, the DNA origami solution was filtered three times with 300 µL of 1 x TAE-buffer with 15 mM $MgCl_2 \cdot 6\ H_2O$ at 3.5 g for 6 minutes in a 0.5 mL Ultracel-100 kDa centrifugal filter (*Amicon*) in a Herafus Fresco 17 centrifuge (*Thermo scientific*). The filtrate was isolated afterwards in a new tube with 4.7 g over 3 minutes. After filtration, the DNA origami solution has a concentration between 30 and 60 ng/µL and was deposited on a silicon substrate. Silicon wafers (*Siegert wafer*), p-type, boron doped, (100) orientation, were cut in 8 x 8 mm^2 pieces marked with a central cross and cleaned with air plasma (*diener scientific*) for 5 minutes. Subsequently, 1 µL of the freshly prepared DNA origami nanostructures were deposited in the middle of the cross marker on the silicon substrate together with 15 µL of 10 x TAE-buffer with 150 mM $MgCl_2 \cdot 6\ H_2O$ and incubated for 1 h at room temperature. To prevent additional drying effects, the substrates are placed in a chamber containing 10 mL of 96 % ethanol (EtOH) (*Sigma Aldrich*) to maintain high humidity. Afterwards, the samples are cleaned once with 1:1 mL deionized H_2O/EtOH and instantly placed in 96 % EtOH for 1 h to get rid of the remaining water in the DNA origami structures. The remaining solution on the samples are blown dry with compressed air and are then ready for the irradiation in the vacuum chamber (chapter 3.3).

3.1.1 Modification of the DNA origami triangle

For the DNA origami technique two aspects are important: First, the modification of the DNA origami triangle with different DNA oligonucleotide target sequences plays a major role. The modification is done by exchanging the original staple strand with an extended and biotinylated oligonucleotide target sequence before the self-assembly process in the thermocycler. Figure 3.1 illustrates the different modifications of the DNA origami triangle (grey) with the different single strands (purple, turquoise and red) and double stranded DNA hairpins (black) with the terminal (green) and intrastrand attachment of the biotin (Bt) molecule (light blue). The latter is very important for the detection of the intact DNA strands in the AFM analysis (chapter 3.4).

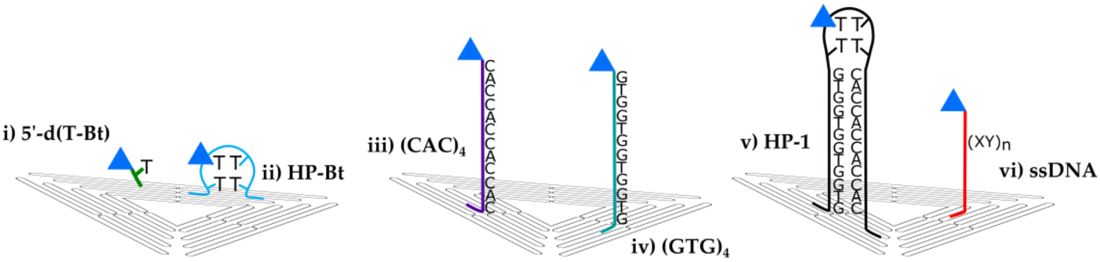

Figure 3.1 Scheme of the used modifications of the DNA origami triangles with i) terminal biotin modification of T-Bt, ii) intrastrand biotin modification of the DNA hairpin loop HP-Bt, iii) ssDNA 5'-d(CAC)$_4$, iv) ssDNA 5'd(GTG)$_4$, v) dsDNA HP-1 5'-d((CAC)$_4$T(Bt-dT)(GTG)$_4$) and vi) variation of the sequence length n of ssDNA XY. The arrangement of the DNA modifications on the DNA origami triangle is only shown arbitrarily.

Second, the identification of the two different target sequences on the DNA origami triangle in a single irradiation experiment is very important. Since the triangle is made out of three connected trapezoids with a symmetric geometry the identification is not self-explanatory. Figure 3.2 shows one trapezoid of the original Rothemund triangle with the unmodified staple strands (orange) and its direction from 5' → 3', the scaffold strand M13mp18 (blue) and the modified positions for the ssDNA and dsDNA (green and black circle). The triangular nanoarray can carry a maximum of six target sequences, whereby there are always two different DNA sequences on one trapezoid of the triangle. To distinguish each side of the triangle in the AFM images, the target oligonucleotides are placed in an asymmetric shape. On one trapezoid two protruding strands are attached, whereas one is placed in the *middle* (black) and one on the *side* position (green) with a distance of approximately 30 nm. The side position can be either on the left or on the right side, depending on the orientation of the triangle. The asymmetric pattern is identical for all trapezoids in the DNA origami triangle (fig. 3.2). This makes it easy to identify the DNA oligonucleotide spots at any time.

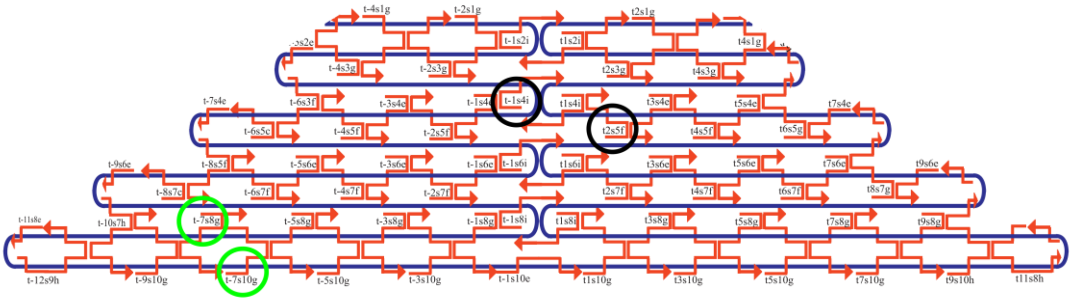

Figure 3.2 Schematic map of one of the three trapezoids of the original Rothemund DNA origami triangle with the staple (orange) and scaffold strand (blue) after the self-assembly process. The circled areas mark the positions of the modifications with ssDNA and dsDNA for the irradiation experiments on the side (green) and the middle positions (black).

3.2 High vacuum chamber setup for LEE irradiation

A vacuum chamber with an electron gun suitable for these applications was manufactured and used for the irradiation experiments of DNA oligonucleotides [16].

3.2.1 Setup

The LEE irradiator consists of a DN100 six-way cross housing with CF flanges and copper sealings to prevent degassing (fig. 3.3f red). The chamber is constructed as small as possible, to reduce the evacuation and venting time. A dual stage rotary vane pump (*Agilent DS 102*) generates a pre-vacuum with a circular rotor located offset in a circular cavity. The rotation transports silicon oil from the inlet towards a chamber of increased volume through the outlet with the same volume and creates a pre-vacuum in this setup up to $1.0 \cdot 10^{-2}$ mbar. This pre-vacuum can start the turbomolecular pump (*Agilent TwissTorr 304 FS*) on the backside of the chamber, which generates the necessary pressure for the irradiation experiments to a minimum of $4.0 \cdot 10^{-8}$ mbar within 24 h (fig. 3.3f dark blue). The principle of the turbomolecular pump is based on a rapidly spinning set of rotor fans (fig. 3.3b) at the inlet giving the gas molecules a momentum towards the exhaust. The particle-surface interactions between the gas molecules and the moving fans generates the high vacuum inside the chamber. To control the pressure during the measurement, a pressure gauge is connected through a T-flange at the bottom of the table. The pressure gauge consisting of a combination of a pirani and ionization pressure gauge (*Agilent FRG-700 CF35*) must be placed as far away as possible from the electron gun (chapter 3.2.2), because of the surrounding magnetic field of the gauge (fig. 3.3f dark green). A magnetic field, even if it is very small, can influence the properties and effectiveness of the electron gun. By thermal conductivity of a platinum filament in a wheatstone bridge inside of the chamber, the pirani gauge measures the pressure up to 10^{-4} mbar. Going to lower pressure values, the pressure gauge is switching automatically to the ionization gauge and is able to detect pressure values up to 10^{-9} mbar by a cold cathode. Within four hours, the whole chamber can be carefully vented via ultra high vacuum (UHV) dosage valve with a gas inlet and sapphire seal (*Vacom 11LVM-4016CF-MS-S*) connected to the DN40 T-flange (fig. 3.3f light blue). The soft ventilation is ensured by two 90° angle connections to avoid fast entering of gas molecules and hitting the DNA origami sample too hard. A custom-built octagonal sample holder (fig. 3.3d and e) is vertically aligned to the electron gun. It is insulated with a ceramic between two metal rods and electrically connected via a copper sliding contact and a BNC feed through (fig. 3.3f light green) with a picoamperemeter (PIA) (*Keithley 6485E*). This connection enables a real-time measurement of the current during irradiation of different samples. The z-translator (fig. 3.3f yellow) and 360° rotator (fig. 3.3f orange) enables a perfect alignment of the electron beam on the sample. For sample analysis, the beam profile is essential and has to be characterized (chapter 3.2.3) for each electron energy. With the sample stage, only the entire current (I_{S}) can be measured and the beam characterization is not possible. Therefore, a Faraday cup (FC) (fig. 3.3c) was constructed by *Miloš Lj. Ranković* to measure the beam profile in detail [16]. Compared to the sample stage, the inside of the FC is isolated with two teflon rings and has a grounded housing. An 8 mm diameter hole in the aluminum housing allows to collect the complete electron beam (I_{FC}). To determine the beam profile, a cover with a central hole of 1 mm diameter can cover the FC to measure parts of the whole beam (I_{i}) (chapter 3.2.3 and 3.2.5).

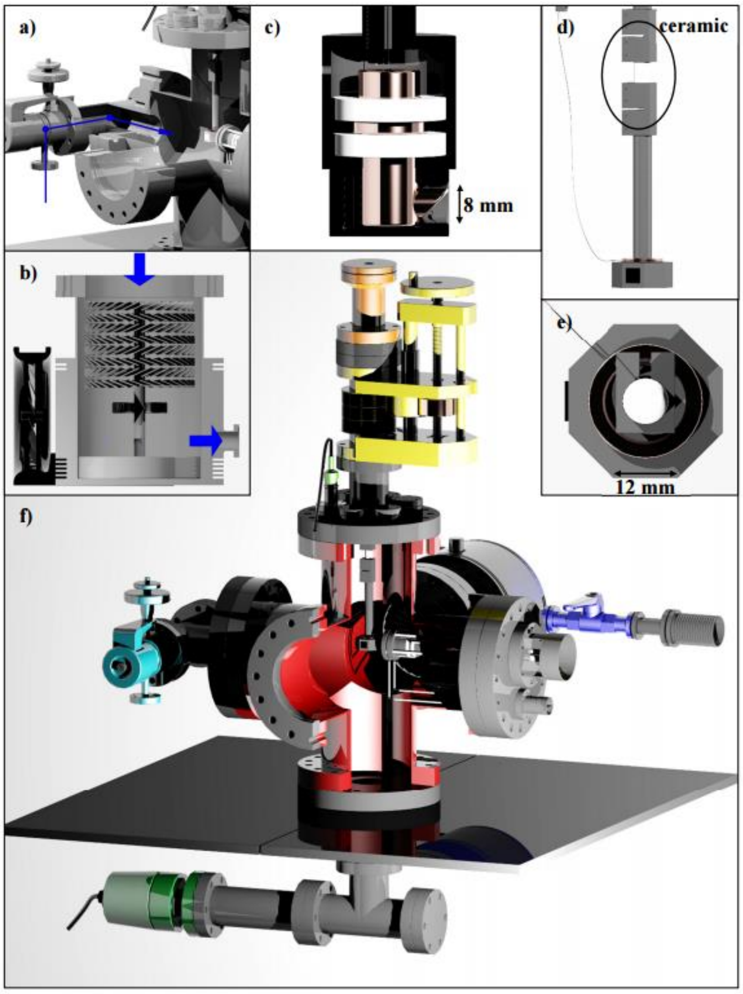

Figure 3.3 Model of the vacuum chamber (f) from *Rackwitz et al.* with the z-translator (yellow), 360° rotator (orange), the valve (light blue) and the pressure gauge (green). The gas inlet for soft ventilation (a), cross section of the turbomolecular pump (b), the Faraday cup (c) and the isolated sample holder from side (d) and top view (e). Image is adopted from ref. [15].

3.2.2 Electron gun

In general, a flood gun is intended to provide a steady flow of high electron currents of LEEs resulting in a large electron distribution. However, an almost uniform electron beam with a current in the nanoampere (nA) range is required for the present DNA irradiation experiments. For this reason, a conventional flood gun (*Omnivac FS100*) was modified to prevent excessive electron flow and the resulting charge of the sample (chapter 3.2.4) [102]. The flood gun is fixed via an asymmetric reduction flange (DN100 to DN40 and DN16) to the vacuum chamber and pointing to the sample holder. Figure 3.4 shows the model of the customized electron gun with a tungsten filament (FIL) (white) and its four electrostatic lenses. A technical drawing of the circuit of the electron gun is shown with all values (tab. 7.3) in figure 7.2. The FIL is a hot cathode and emits electrons due to thermionic emission. It is operated at 2.1 A and is powered by a *GW Instek GPD-2303S* power supply. To control the emission current from the FIL, a multimeter (EMS) is connected. A hollow cylinder, called Wehnelt cylinder (WEH) (fig. 3.4 dark blue), with an aperture encloses the FIL. It is a convergent lens that suppresses emission of electrons from most areas of the cathode and is biased to a negative voltage relative to the FIL. The extractor (EXT) (fig. 3.4 light blue) as the second electrostatic lens is focusing the electron beam again and is set to 65 V voltage. EXT is fixed and isolated with two ceramic rings from the WEH and anode (ANO) (fig. 3.4 green). In order to accelerate the electrons to the sample and defocus the beam again, a small potential was applied to the third electrostatic lens ANO. Defocusing is necessary to enable a homogeneous electron beam on the sample. With decreasing kinetic energy of the thermionically emitted electrons, the voltage at ANO needs to be reduced to decrease the defocusing effect. This results in an increasing number of electrons on the sample. Therefore, the potential of ANO has to be adjusted for every kinetic energy of the electrons to keep the current on the sample constant. The last electrostatic lens represents the shutter (SHT) (fig. 3.4 red) and is positioned in front of the electron gun with two ceramic spacers. By applying a voltage of 14 V (*Voltcraft VSP 2653*) to the SHU, the electron beam can be completely defocused. In result, electrons can no longer reach the sample, which is important for the irradiation time of the individual samples. If the SHU is grounded, all electrons can pass through the opening hole (4 mm) as desired. So, the beam is shaped according to the selected settings of the individual components.

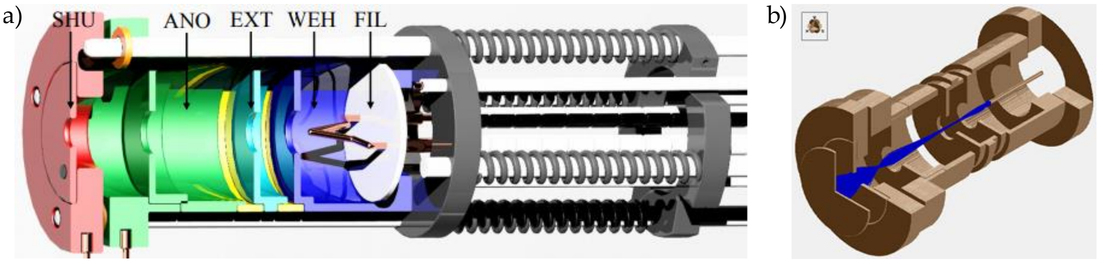

Figure 3.4 a) Model of the customized electron gun with the filament (white), Wehnelt cylinder (blue), extractor (light blue), anode (green) and the shutter (red). SHU is isolated with a ceramic ring (orange). Image is adopted from ref. [15] b) Scheme of the simulated electron beam through the electrostatic lenses in the flood gun.

3.2.3 Characterization of the electron beam

Another important aspect besides the selected settings for the electrostatic lenses is the electron beam characterization. For sample analysis, the current determination of the silicon substrate in a total area Z_{total} is necessary. Therefore, the beam profile must be determined and characterized with a modified FC in the vacuum chamber. The FC is mounted to the rotator/translator and its opening (0.8 cm) is covered by a panel with a centered hole with a diameter of 0.1 cm. Thus, parts of the beam at a defined area Z_{i} can be determined by moving the FC vertically through the beam with increments of 0.2 mm height h. The measured current I_{i} is averaged at each h for 15 seconds. Figure 3.5 shows the plot of the corresponding current and error as a function of the h coordinate of the FC position (settings for 7 eV electron energy). Due to the Gaussian shape of the electron beam, more electrons reach the sample at the central region (fig. 3.5 green) than the outer region (fig. 3.5 light blue). The position h = 0 mm represents the center of the beam with the maximum current value. Due to the very short exposure times, the current on the samples can be assumed to be constant and homogeneous within one area Z_i, what makes the following assumptions and calculations possible. The 2D beam profile (fig. 3.5a) is assumed to have rotational symmetry with a total area Z_{total} and can be divided into discrete, non-overlapping areas Z_{i} (fig. 3.5b). Due to the 0.1 cm hole of the aperture on the FC, each Z_{i} is defined as a discrete circle with a diameter d_{i} of 0.1 cm resulting in a radius r_{i} of 0.05 cm. Each area is small enough to assume a homogeneous current I_{i}, which is necessary for the fluence calculation in chapter 3.2.5. The center of each circle has a distance k_{i} to the center of the total beam area Z_{A} . With the help of the coordinates y and z and the Pythagorean theorem (eq. 3.1) the corresponding k_{i} of each circle can be calculated. The distance calculation enables the determination of the current I_{i} within each associated area Z_{i}.

$$k_{\mathrm{i}} = \sqrt{y_{\mathrm{i}}^2 + z_{\mathrm{i}}^2} \tag{3.1}$$

Nevertheless, the subdivision of the beam profile into discrete circles does not cover the entire beam profile and has not considered areas in-between the circles. Hence, the circles are transferred into squares with the area $Z_{\mathrm{i}}^{\mathrm{s}} = d_{\mathrm{i}}^2$ (eq. 3.2). The area of the circle Z_{i} is defined as $Z_{\mathrm{i}} = \pi r_{\mathrm{i}}^2$, with $2r_{\mathrm{i}} = d_{\mathrm{i}}$. Accordingly, the current value of the circle I_{i} can be transformed to the current value of the square $I_{\mathrm{i}}^{\mathrm{s}}$ by multiplying with $\frac{4}{\pi}$ (eq. 3.3).

$$Z_{\mathrm{i}}^{\mathrm{s}} = Z_{\mathrm{i}} \cdot \frac{4}{\pi} \tag{3.2}$$

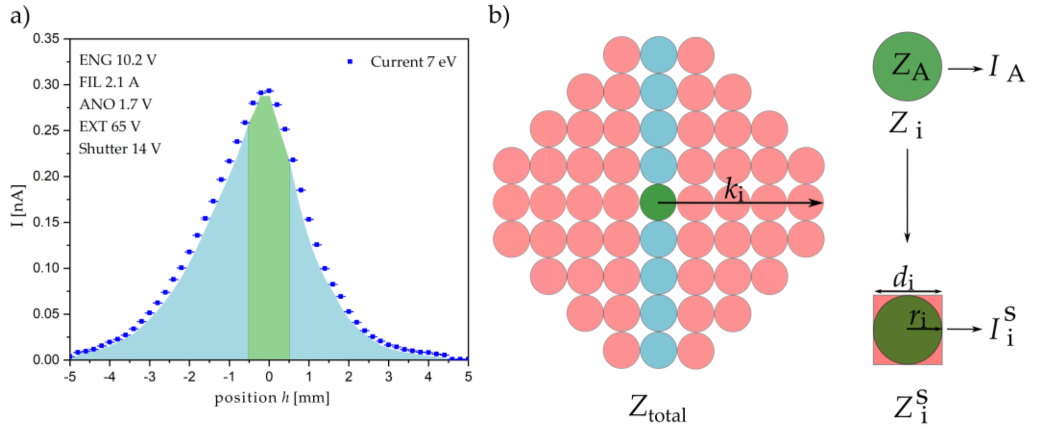

Figure 3.5 a) Measured current $\boldsymbol{I_\mathrm{i}}$ as a function of h in 0.2 mm steps with the faraday cup gives the 2D beam profile at 7 eV electron energy. The measured current $\boldsymbol{I_\mathrm{i}}$ averaged at each $\boldsymbol{h}$ for 15 seconds. b) Schematic drawing of the total beam profile $\boldsymbol{Z_\mathrm{total}}$ on the sample with one discrete area $\boldsymbol{Z_\mathrm{i}}$ with a distance of $\boldsymbol{k_\mathrm{i}}$ to $\boldsymbol{Z_\mathrm{A}}$. Blue circles represent the measured current $\boldsymbol{I_\mathrm{i}}$ along the z-axis of the FC. Green circle shows the area $\boldsymbol{Z_\mathrm{A}}$ with a homogeneous current for the fluence calculation. The conversion from a circled area $\boldsymbol{Z_\mathrm{i}}$ to a square are $\boldsymbol{Z_\mathrm{i}^\mathrm{s}}$ with a diameter of $\boldsymbol{d_\mathrm{i}}$.

$$I_\mathrm{i}^\mathrm{s} = I_\mathrm{i} \cdot \frac{4}{\pi} \tag{3.3}$$

The total current I_total is obtained by summing up all I_i in all Z_i and multiplying with the factor $\frac{4}{\pi}$ (eq. 3.4).

$$I_\mathrm{total} = \sum_{\mathrm{n}=0}^{\mathrm{i}} I_\mathrm{i}^\mathrm{s} \tag{3.4}$$

Due to the Gaussian shape and the rotational symmetry of the electron beam, the current percentage $I_\%$ in any Z_i^s can be calculated from the total current I_total and the current I_A^s in area Z_A^s.

$$I_\% = \frac{I_\mathrm{A}^\mathrm{s}}{I_\mathrm{total}} \tag{3.5}$$

In this work, irradiation experiments were made with an electron energy between 5 and 20 eV. Since the profile slightly changes during the lifetime of the filament, the beam profile is measured several times.

3.2.4 Settings of the electrostatic lens

For the electron irradiation experiments it is of great importance to determine the electron beam on the silicon sample in detail. According to that, the settings of each electrostatic lens (WEH, EXT, ANO) and the beam voltage (ENG) have to be set.

The settings should be optimized for each electron energy (5 – 20 eV), to obtain an electron beam with a small current (2-4 nA) measured at the sample.

When the electrons hit the silicon surface, a repulsive potential is generated by a charging of the sample substrate, which lowers the actual electron energy. By measuring the current on the sample I_S while increasing the voltage of ENG, the charging of the silicon surface can be detected (fig. 3.6).

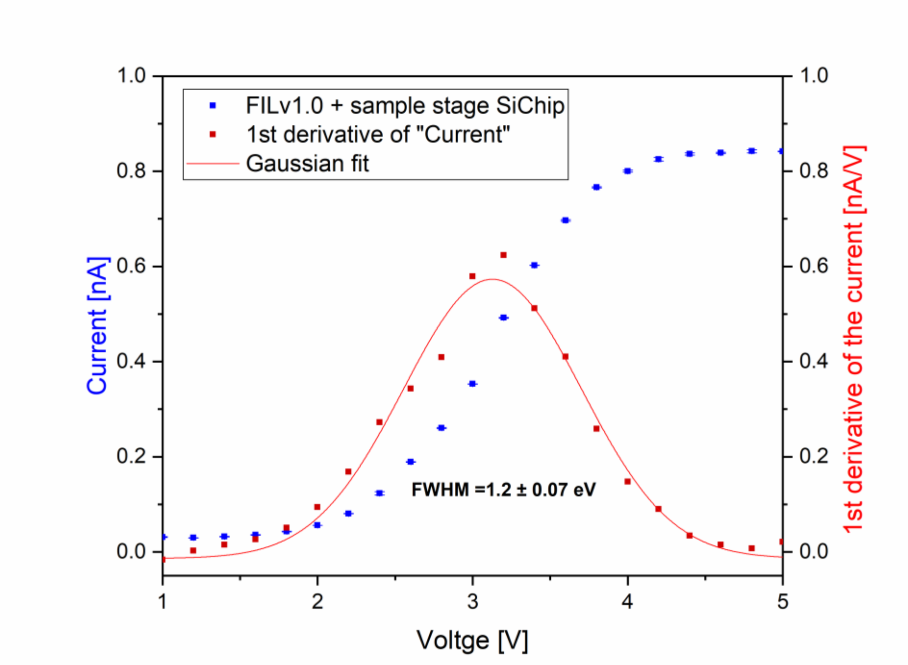

Figure 3.6 Plot of the charging effect of a silicon surface measured with a silicon sample attached to the sample holder (blue). From the first derivative of the current (red) the energy distribution of $\mathbf{1.2\ \pm 0.07\ eV}$ of the electron beam.

Due to the charge of the substrate, no electrons can be detected below 2 V. Above 2 V, electrons can pass the silicon surface and a current can be measured. Furthermore, increasing of ENG results in a gradual increase of the current implying a finite energy distribution of the electrons. The maximum of the 1st derivative of the current-energy curve represents the point of zero energy. This value was changed from 2 V to 3.2 V from previous experiments [16]. The energy distribution can be obtained from the full width at half maximum (FWHM) of the gauss fit of the 1st derivative of the measured current (fig. 3.6). The used setup and the corresponding settings give rise to an electron energy distribution of 1.2 ± 0.07 eV. This electron resolution must be considered in the experiments and discussion of the results.

3.2.5 Fluence determination

The fluence F of the electron beam describes the total number of electrons n_e in a certain irradiation area of the circle Z_i (eq. 3.6). n_e is given by the irradiation time t and the current I and the elementary charge e (eq. 3.7).

$$F = \frac{n_\mathrm{e}}{Z};\,[F] = \frac{1}{[cm^2]} \tag{3.6}$$

$$n_\mathrm{e} = \frac{I \cdot t}{e};\,[n_\mathrm{e}] = \frac{[A] \cdot [s]}{[C]} \tag{3.7}$$

$$F = \frac{\frac{I \cdot t}{e}}{Z_\mathrm{i}};\ [F]\,\frac{\frac{[A] \cdot [s]}{[c]}}{[cm^2]} = [cm^{-2}] \tag{3.8}$$

The elementary charge e is the magnitude of the negative electric charge carried by a single electron transported by a constant current of 1 ampere (A) in 1 second (SI unit 1C = 1 As). It is a fundamental physical constant under the 2019 redefinition of the SI base units and is exactly $1.602 \cdot 10^{-19}$Coulomb (C). For the calculation of the relative fluence F, the measured current has to be converted into the elementary charge per second (eq. 3.10). Consequently, 1 nanoampere ($1\,nA = 10^{-9}\frac{C}{s}$) corresponds to $6.242 \cdot 10^9$ electrons illuminating the surface per second (eq. 3.11).

$$1A = 1\frac{C}{s} \tag{3.9}$$

$$1C = \frac{1}{1.602} \cdot 10^{19}e \tag{3.10}$$

$$1\,nA = 10^{-9}\frac{C}{s} = 10^{-9} \cdot \frac{1}{1.602} \cdot 10^{19}\frac{e}{s} = 6.242 \cdot 10^{9}\frac{e}{s} \tag{3.11}$$

$$F = \frac{I \cdot 6.242 \cdot 10^{9} \cdot t}{Z_\mathrm{i}};\ [F] = \frac{[nA] \cdot \left[\frac{e}{s}\right] \cdot [s]}{[cm^2]} = [cm^{-2}] \tag{3.12}$$

Some electrons hitting the surface might get reflected and are not detected by the current measurements. To accurately determine F not only the measured current I_Si must be considered, but the absolute current $I_\mathrm{FC} = I_\mathrm{Si} + I_\mathrm{R}$, where I_R is the current which is reflected from the substrate and I_FC is the current measured by an FC. In order to obtain I_FC from I_Si measurements, a factor f is determined for each electron energy (5-20 eV) (tab. 7.3).

$$f = \frac{I_\mathrm{FC}}{I_\mathrm{Si}} \tag{3.13}$$

The reflected current I_R can even get larger than I_FC when the incident electrons generate enough secondary electrons from the metal surface. In our case a value for f close to 1 is determined for 20 eV electron energy. Presumably, the coefficient for the secondary electron emission becomes greater 1 from higher electron energies. In result, the factor f represents the ratio between the measured electrons by an FC and the transmitted electrons through a silicon chip and gives the absolute fluence F_{FC}.

$$F_{\mathrm{FC}} = F \cdot f \tag{3.14}$$

During irradiation, the total current I_{total} is measured in real time and is corrected by the electron energy dependent factor f. If F is obtained with the total current I_{total} from the total square area $Z^{\mathrm{s}}_{\mathrm{total}}$, an average value for F results because of the Gaussion shape of the electron beam. The sample surface is only analyzed using AFM images of $4\,x\,4\,\mu m^2$ within the area Z_{A}. Since only a small fraction out of the total irradiation area Z_{total} can be analyzed a precise determination of F at the AFM position is necessary. Therefore, the current percentage $I_{\%}$ must be included in the fluence calculation. The final equation 3.15 to determine the absolute fluence F takes the current percentage $I_{\%}$ from the area $Z^{\mathrm{s}}_{\mathrm{A}}$ and the factor f for the reflecting electrons into account.

$$F_{\mathrm{FC}}[cm^{-2}] = \frac{I_{\%} \cdot [6.242 \cdot 10^{9}] \cdot t}{Z_{\mathrm{i}}} \cdot f \tag{3.15}$$

3.3 Irradiation of samples

The custom-built sample stage is made out of a metal block with an octagonal base and is insulated from the chamber with a ceramic between two metal rods. For real-time current measurements, the sample stage is electrically connected via a copper sliding contact (DN16 ring) and a BNC feed-through to a picoamperemeter (*Keithley 6485E*). A maximum of eight Si/SiO$_2$ (8 x 8 mm^2) samples can be fixed with copper conductive tape. In order to place the electron beam in the middle of the samples, the sample holder is aligned vertically and horizontally using a z-translator (50 mm maximum travel distance) and a 360° rotator. The current I_{Si} is measured in real-time during irradiation of each sample.

The irradiation experiments always follow the same pattern, in which at least one series of each DNA origami sample modified with two different target DNA sequences is irradiated. Each series contains eight samples, six of these samples are irradiated at different fluences (10 s, 20 s, 30 s, 40 s, 50 s and 60 s irradiation time) and two non-irradiated control samples, whereas one is located inside of the vacuum chamber. This gives us the opportunity to investigate the vacuum effect and that of the scattering electrons. The respective number of irradiated samples strongly depends on the quality of the samples and the population density of the DNA origamis on the silicon surface (chapter 3.5). During irradiation procedure, fluences below $3 \cdot 10^{13}\ cm^{-2}$ are used to avoid saturation of DNA strand breaks at higher fluences. Saturation is caused by interstrand crosslinks between DNA target sequences and the DNA origami, which can no longer be detected as DNA strand break.

3.3.1 Irradiation procedure

The electron beam is controlled by a custom-built electron beam shutter (SHU) with a 4 mm diameter aperture positioned in front of the electron gun with ceramic spacers (fig. 3.4a). By applying a voltage of 14 V to the electrostatic lens, the electron beam will be completely defocused and no electrons can pass. If SHU is grounded, the blocked electrons can pass through the shutter to the samples again. The SHU is necessary to block the beam path for positioning a non-irradiated sample in front of the electron beam by rotating the sample stage. A strong decrease of the current was measured within the first few seconds on the sample after grounding the SHU again (fig. 3.7a). This drop is caused by the jammed electrons, which pass through the SHU after opening. In order to prevent this case, irradiations were carried out with the SHU open and a 2 s window for the sample change was accepted in which the current measurement was interrupted. Since all samples go through the same procedure, these additional electrons can be neglected and the effect of the scattering electrons on the fluence is higher for shorter irradiation times. In result, a more constant and homogeneous electron current is measured (fig. 3.7b).

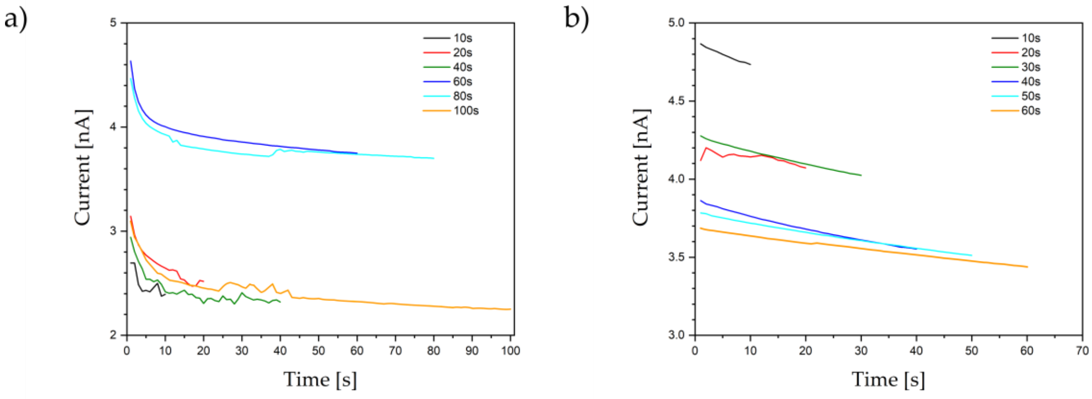

Figure 3.7 Measured current on the sample stage with closed (a) and open (b) SHU during rotation of the sample holder to a non-irradiated sample.

For the electron irradiation experiments, currents in the low nanoampere range of $2-4\,nA$ are required. The filament FIL (hot cathode) is operated with a current of 2.1 A and is immediately at operating temperature after switching on. The other electrostatic lenses (EXT, ANO, WEH and FIL) and the surroundings warm up slowly. Figure 3.7 shows the real-time beam current during a long period of the electron gun. Very high electron currents of up to $25\,nA$ are obtained at the beginning of the warm-up period, whereas a rapid drop in the beam current from around $20\,nA$ to $2-5\,nA$ occurs and remains stable for hours. This is caused by the thermal evaporation of residues on the FIL and surroundings. In order to obtain a stable and focused electron beam, a warm-up period of exactly 30 minutes is used. Longer periods are not recommended as scattering electrons and heat emitted by the electron gun can damage the DNA origami nanostructures without being noticed.

3.4 The DNA origami technique

According to the original protocol by *Rothemund* [30], DNA origami triangles were used for the DNA origami technique established 2012 by *Keller et al.* [10] with specially designed oligonucleotides as target sequences. The DNA origami technique is used to determine absolute cross sections of LEE induced DNA strand breaks. This method has several advantages compared to other experimental approaches: (i) Maximum sensitivity can be achieved with only small quantities of material. (ii) Within a single irradiation experiment, two different oligonucleotide sequences can be directly compared under the same experimental conditions. (iii) The determination of absolute DNA strand break cross sections for arbitrary DNA sequences. (iv) The DNA nanoarrays can be modified with ssDNA [12], dsDNA or higher-order DNA structures like DNA telomer sequences [13]. (v) Application with many different radiation sources such as UV radiation [11], X-rays and especially LEE radiation is possible. These properties give us the opportunity to study interactions of different well-defined DNA molecules with LEEs of varying electron energies. DNA origami nanostructures are available in almost arbitrary shapes, with the triangular shaped DNA origami being particularly favorable for the method, since they adsorb very well on the silicon substrates with high stability in shape. They have also a small tendency to form clusters, because there are no blunt ends pointing out of the nanostructure. A good and precise addressability can be achieved, which facilitates modification with multiple DNA strands.

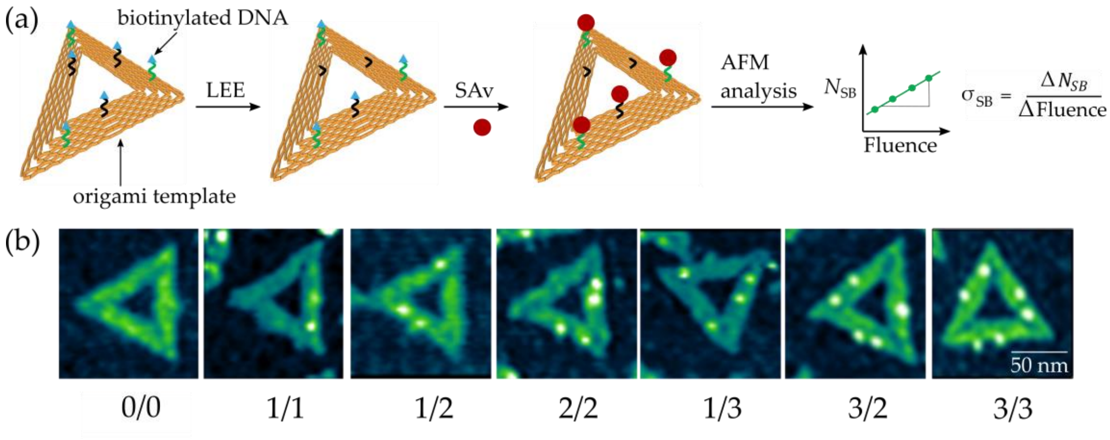

Figure 3.8 (a) Scheme of the DNA origami structure (yellow) and the experimental procedure to determine absolute DNA strand break cross sections. Each DNA origami triangle can carry two different (black and green) biotinylated target sequences. The samples are treated with streptavidin (SAv) to visualize the intact DNA sequences (red). b) Examples of AFM images for DNA origami nanostructures irradiated at 7 eV electron energy with up to six bright spots on top. Bright spots indicate SAv molecules attached to intact target sequences.

Figure 3.8 shows the experimental procedure to determine the absolute cross section of DNA strand breakage with DNA origami nanostructures carrying the DNA target sequences. Depending on the selected electron energy and irradiation time, more or less DNA strands are broken during the irradiation process in the vacuum chamber. The damaged DNA strands are shown as short green and black lines, which no longer have the terminal Bt molecule (light blue triangle). The intact DNA target sequences are visualized for AFM images by incubation with streptavidin (SAv). The streptavidin-biotin-bond is one of the strongest known non-covalent interactions in nature, which exhibits a dissociation constant K_d of $10^{-14} - 10^{-15}\ M$ [103]. Therefore, SAv binds specifically to Bt and only interacts with the unbroken DNA oligonucleotides. Figure 3.8b shows AFM images of DNA origami nanostructures with a different state of damage. The (3/3) DNA origami represents a non-irradiated control sample where all six target positions stay intact and the SAv-Bt binding efficiency is 100% on this DNA origami. The first number in brackets represents the amount of intact DNA strands in the *middle* position while the second number represents the *side* position. The two different positions on each side of the triangle can be clearly distinguished in AFM images, because of a 30 nm distance between both DNA sequences. This gives us the opportunity to study two different DNA sequences under the same irradiation conditions. AFM measurements are performed in the center of the electron beam within a circle area Z_A with a diameter of $d = 1\ mm$, a current percentage $I_{\%}$ and a factor f depending on the electron energy. Each sample can be analyzed by counting the triangles manually or using a software (*Phythagoras_v2.0)*. It is a graphic analysis software specially developed for this application and can recognize the DNA origami triangles and the bright SAv spots on top. The software analysis and its comparison to the manual analysis is described in chapter 4.5 in more detail. By counting all intact DNA strands on the AFM images the relative number of strand breaks N_{SB} in comparison to a non-irradiated control sample is obtained. N_{SB} is calculated by the ratio of the maximum possible number of intact oligonucleotides N_0 and the number of intact oligonucleotides after irradiation N_{t} for a specific irradiation time t (eq. 3.17). N_0 is calculated from the number of counted DNA origamis N_{origami} times the maximum number of target sequences on the *middle* or *side* position (3) of the DNA origami triangle (eq. 3.16).

$$N_0 = N_{\mathrm{origami}} \cdot 3 \tag{3.16}$$

$$N_{\mathrm{SB}} = 1 - \frac{N_{\mathrm{t}}}{N_0} \tag{3.17}$$

The number of strand breaks N_{SB} increases with the absolute fluence F (eq. 3.18) according to the strand break cross section.

$$N_{\mathrm{SB}} = \sigma_{\mathrm{SB}} \cdot F + N_{\mathrm{SB0}} \tag{3.18}$$

This results in a dose-response curve with a linear part at low fluences. The crossing point with the y-axis at a value of $F = 0$ represents the number of strand breaks of a non-irradiated control sample N_{SB0}. In the case of a non-irradiated sample, the value for intact DNA oligonucleotides is approximately 10-20% and reflects the binding affinity of SAv-Bt. From the slope of the instrumental weighted linear fit, we determine the absolute SB cross sections σ_{SB} for the respective DNA sequence and electron energy.

$$\sigma_{\mathrm{SB}}\ [cm^2] = \frac{N_{\mathrm{SB}}}{F} \tag{3.19}$$

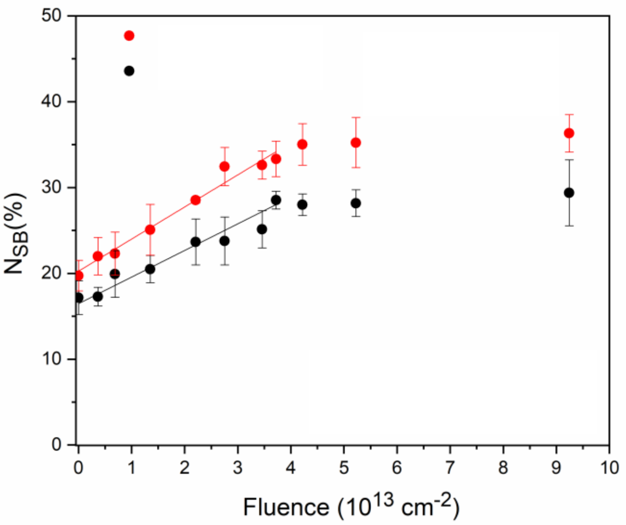

Figure 3.9 Example of an exposure-response curve for two different target sequences red and black. The DNA strand break cross section can be determined from the linear fit of the low fluence regime below 4 x 10^{13} cm^{-2}.

Figure 3.9 shows an example of an exposure-response curve to determine the absolute DNA strand break cross section. At high fluences a saturation of N_{SB} is reached due to formation of DNA cross links [10]. Hence, only the low-fluence regime is used for linear fitting. This way, the cross section for SB can be obtained in dependency of the DNA sequence, the radiation type and the radiation energy. The technique is highly reproducible, which yields uncertainties of typically 10% to 20%.

3.5 AFM analysis of irradiated DNA origami

Atomic force microscopy was invented in 1986 by Gerd Binnig, Christoph Gerber and Calvin Quate [104] and is based on the concept of scanning probe microscopy (SPM), in which the image is not generated with an optical or electron-optical lens. The information is gained by mechanical interaction between a probe and the sample surface. In conventional light microscopes the resolution depends on the wavelength, while the resolution in AFM mainly depends on the shape and diameter of the tip of the scanning probe. Therefore, AFM is a suitable technique to analyze the DNA origami samples, since it has only a few-nanometer resolution and can visualize small surface structures below the optical diffraction limit. Additionally, only a very small amount of material immobilized with sub-monolayer coverage is necessary.

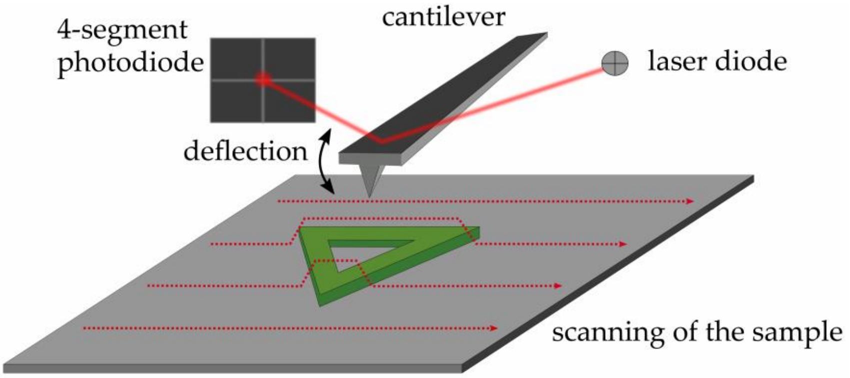

Figure 3.10 Scheme of the AFM measurement principle. A laser is focused on a cantilever and is reflected to a 4-segment photodiode. By scanning the sample surface, the cantilever bends by interacting with obstacles. The position change of the laser spot is translated into a topography image.

A cantilever with a sharp pyramid tip (apex radius < 10 nm) serves as a probe and is moved over the sample by piezoelectric elements scanning the surface with high lateral precision point by point [105]. Approaching the surface, the cantilever is bent by attractive and repulsive forces depending on the distance between both. Attractive forces are predominantly Van-der-Waals forces (VdW) and capillary action at distances of 1 – 10 nm and electrostatic forces up to 100 nm. The repulsive forces are described by the coulomb repulsion (Pauli-principle) at atomic distances of 0.1 nm. A macroscopic bending of the cantilever towards the sample for attractive forces and away from the sample for repulsive forces is the result. A laser is focused on the backside of the cantilever and is reflected to a 4-segment photodiode (fig. 3.10). Depending on the position and bending of the cantilever, the position of the reflected laser on the photodiode changes simultaneously and allows the determination of the cantilever in x and y spatial direction. The bending can be plotted as force measurement that can be approximated with the Lennard-Jones potential $V(k_{\mathrm{s-p}})$ (eq. 3.20), with the potential depth ε, the distance between the surface and probe $k_{\mathrm{s-p}}$ and the finite distance k_0 at which the interparticle potential is zero.

$$V(k_{\mathrm{s-p}}) = 4\varepsilon\left[\left(\frac{k_0}{k_{\mathrm{s-p}}}\right)^{12} - \left(\frac{k_0}{k_{\mathrm{s-p}}}\right)^{6}\right] \tag{3.20}$$

A software calculates the translation of the cantilever into a relative height of each measurement point and generates a digital image. Depending on the investigated sample and substrate material different operation modes are possible with AFM. Usually they are divided in *static* and *dynamic* modes. The first one is a *contact* mode, where the cantilever tip is in close contact to the sample surface and in the range of the Pauli-repulsion with constant distance to the sample surface during the scanning process. Therefore, the tip height changes according to the sample height (fig. 3.10). This method might be harmful for the sample and the tip, because of the close and direct contact of both. A less destructive method is the *dynamic* mode or *tapping* mode, where the tip is oscillating near its resonance frequency with a constant amplitude while scanning over the surface. Due to the change of the sample height, the amplitude and phase of the oscillation changes according to the surface topography. To keep the amplitude and phase constant, a control circuit is applied to correct these changes. The values for the amplitude and phase adjustment provide the information for the digital image. This method is particularly suitable for samples with a small difference in sample height or very soft materials, such as DNA samples.

After irradiation, the samples are removed from the sample holder in the vacuum chamber and are incubated with 15 µL of 50 nM streptavidin (SAv) solution for 2 minutes. Afterwards, they were rinsed with 500 µL 1:1 H_2O/EtOH and dried with compressed air to clean and remove the remaining impurity. Depending on the configuration, SAv has a size of 4.5 x 4.5 x 5 nm^3 and can be visualized with AFM. If a DNA strand break occurs, it no longer carries a terminal Bt molecule and no SAv can bind to the DNA strand. The SAv is detected by a bright spot on the DNA origami in the AFM image, which is caused by the height difference (fig. 3.11 left).

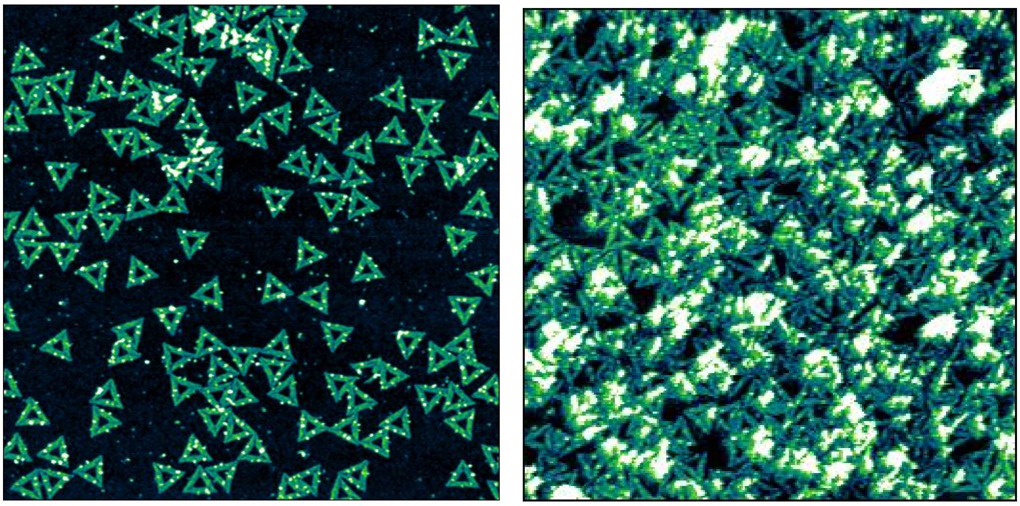

Figure 3.11 Left: Triangular shaped DNA origami nanostructures with streptavidin attached to intact DNA strands in the middle and side position. Each triangle can carry up to six target sequences (3/3) Right: Well-formed DNA origami nanostructures covered with high concentration of streptavidin and buffer residues. This type of sample image is not included in the statistics.

As discussed in chapter 3.1 and 3.3, all silicon samples are marked with a cross in the center of which the electron beam is focused. The central area Z_{A} and the associated current I_{A} covers an area of $0.0079\ cm^2$ with a radius $r = \ 0.05\ cm$. It is of great importance to analyze the central area Z_{A} of irradiation in order to obtain a correlation to the current I_{A} and with that the calculated fluence F. The AFM used in this thesis is an Agilent 5500 (*Keysight; former Agilent Technologies*) operated in the *tapping* mode and a cantilever Tap 150 Al-G (*Budget Sensor*) with a resonance frequency of 150 kHz and a spring constant of 5 N/m. Images are recorded with a size of $4\ x\ 4\ \mu m^2$ and a resolution of 1024 pixels/line. Typical software parameters for scan speed (1.0 - 2.4 lines/s) and P-gain (proportional gain, 1000-2000) and I-gain (integrational gain, 1000-2000) vary for each AFM image. Using the top view camera of the AFM, at least four images (one in each quadrant) were taken at $(250 \pm 100)\ \mu m$ from the center of the marked cross on the silicon substrate. Depending on the density of the immobilized DNA nanostructures, each AFM image usually contains 1000 - 2000 DNA origami triangles.

3.5.1 Evaluation of the data set

The manual analysis is characterized by a high precision of the detection of intact DNA strands with a low error for cross section values of approximately 10-15%. A high resolution of the AFM image is necessary to visualize the SAv molecules on the DNA origami. The manual analysis is carried out using certain criteria: The most important criterion is the assessments of the constitution and conformation of the DNA origami triangle itself. Strongly deformed or destroyed DNA origami with a deviation of the original triangular shape are not included in the statistics. Furthermore, contaminated DNA origamis, e.g. covered with salt or remaining solution are not analyzed (fig. 3.11 right). Another important criterion is the determination of the number of SAv molecules on the DNA origami. The number of intact strands on each DNA origami must be identified, corresponding to their position (*middle* and *side*) on each trapezoid. A maximum of six protruding strands, whereas three SAv molecules at the *middle* and three at the *side* position of the DNA origami can be present. There are always the same DNA target sequences in the *middle* and *side* position, what gives us the opportunity to examine two different DNA sequences under identical experimental conditions. Depending on the orientation of the triangle (face up or face down) on the silicon substrate, the *side* position is always to the left or always to the right of the *middle* position on each trapezoid. In addition, SAv has an affinity to blunt-end ssDNA with open binding sites, which can be found on the edges of the triangle. Each data point in the exposure-response curves represents at least four $4\,x\,4\,\mu m^2$ (1024 pixel/line) AFM images from one series. Usually three series are required for sufficient statistics of identical target sequences and electron energy. However, this depends heavily on the quality of the nanostructures and density on the samples. The results of different irradiation experiments of different series with a certain electron energy for the same target sequences presented here agree very well and show the good reproducibility of the DNA origami technique.

Good statistics always require a large set of data in order to get a meaningful result. The analysis and evaluation of the AFM images is very time-consuming and can be improved by using a graphical analysis software. *Pythagoras* was developed in cooperation with Dr. Phillip Wagner and is perfectly adapted to the DNA origami method in order to reduce processing time. In chapter 4.5 a comparison between manual and software analysis is made in terms of the quality of the result and time saving aspect.

4 Results and Discussion

By deposition of ionizing radiation in cells most of the energy is channeled into the production of abundant LEE with energies between 1 and 20 eV. It was postulated that reactions of LEE with biomolecules can induce high yields of single and double strand breaks well below the ionization threshold [58]. The DNA damage is caused via the DEA mechanism by rapid decay of the TNI localized on the DNA components. According to the traditional notion of DNA radiation damage genotoxic damage from LEE only occurs at energies above the onset of ionization threshold. To address this aspect explicitly, chapter 4 discusses fundamental experiments with well-defined DNA oligonucleotides illuminated with LEE radiation (5 to 20 eV) in the range below, close to and above its ionization threshold. The obtained DNA strand break cross sections are compared for a range of DNA sequences, DNA lengths, DNA radiosensitizer modifications, DNA binders and radiation energy. In addition, the modification of DNA with radiosensitizers gives the opportunity to determine enhancement factors (EF) compared to unmodified DNA oligonucleotides with the same sequence. All data are compared with the results of other groups working in this field and put into context.

4.1 LEE-induced strand breaks in single stranded poly(A) DNA

Recently, it was shown that low-energy electron-induced DNA strand breaks depend, to some degree, on the specific DNA sequence and length [11]. Chapter 4.1 focuses on the effect of LEE-induced DNA strand break cross section on the oligonucleotide length at various irradiation energies. Preliminary studies shown that the effect towards LEE-induced DNA strand breakage is the highest for adenine rich DNA oligonucleotides. The DNA strand break CS for four homo-oligonucleotides (5'- d(A_{12}), 5'-d(G_{12}), 5'-d(C_{12}), and 5'-d(T_{12})) have been compared upon electron irradiation with 8.8 eV. The differences in σ_{SSB} were very small, but the authors showed the highest σ_{SSB} for the A_{12} sequence. A slight trend of ($A_{12} > T_{12} > C_{12} > G_{12}$) with $\sigma(d(A_{12})) = (3.9 \pm 0.4) \cdot 10^{-15}$ cm² and $\sigma(d(T_{12})) = (3.7 \pm 0.2) \cdot 10^{-15}$ cm² as the highest values and $\sigma(d(G_{12})) = (3.1 \pm 0.2) \cdot 10^{-15}$ cm² as the lowest value was observed. Therefore, poly-adenine sequences (5'-(A_4), 5'-(A_8), 5'-(A_{12}), 5'- (A_{16}), and 5'-(A_{20})) were systematically studied and irradiated with 5.0, 7.0, 8.4 and 10.0 eV electrons [12].

Similar experiment with guanine (G)-rich telomer sequences (5'-(GGG ATT)$_x$ with X = 2,3 and 4) on DNA origami platforms are exposed to low-energy electrons of 8.8 eV [13]. A higher sensitivity towards LEEs for longer DNA sequences (going from 5'-(GGG ATT)$_2$ over 5'-(GGG ATT)$_3$ to 5'-(GGG ATT)$_4$) was observed. This effect can either result from the increased amount of G bases or the increased number of nucleobases for the different oligonucleotides. Previous experiments studied the different amount of G bases in DNA oligonucleotides of the same length. A clear increasing sensitivity towards 1 eV electrons with higher G content was observed [89]. Various lengths of polyadenine ssDNA (4, 8, 12, 16, and 20 nucleotides) are studied to systematically investigate the effect of the oligonucleotide length on the SB cross section upon LEE irradiation with electron energies of 5.0, 7.0, 8.4, and 10.0 eV. This covers the energy range of secondary electrons produced in water radiolysis and which are close to typical energies at which SSBs have been observed before [57]. These experiments yield information about resonant formation of DNA strand breaks for specific ssDNA and a presumed additivity of SB cross sections.

Table 4.1 Overview of the absolute cross sections for SBs (σ_{SSB}) for the different DNA sequences upon electron irradiation at different energies compared to the geometrical cross sections (σ_{geo}).

Sequence	**ssDNA SB Cross Section σ_{SSB} [10^{-15} cm^2]**				**σ_{SSgeo} [10^{-15} cm^2]**
	5 eV	**7 eV**	**8.4 eV**	**10 eV**	**/**
A_4	1.03 ± 0.12	4.79 ± 1.04	3.27 ± 0.51	2.25 ± 0.15	11.04
A_8	0.93 ± 0.17	5.59 ± 0.66	5.09 ± 0.92	2.42 ± 0.33	22.08
A_{12}	1.34 ± 0.17	6.95 ± 1.12	6.32 ± 0.59	3.10 ± 0.54	33.12
A_{16}	1.94 ± 0.36	7.69 ± 1.02	7.62 ± 0.95	3.88 ± 0.34	44.16
A_{20}	0.85 ± 0.13	5.06 ± 0.28	4.72 ± 0.32	2.73 ± 0.42	55.20

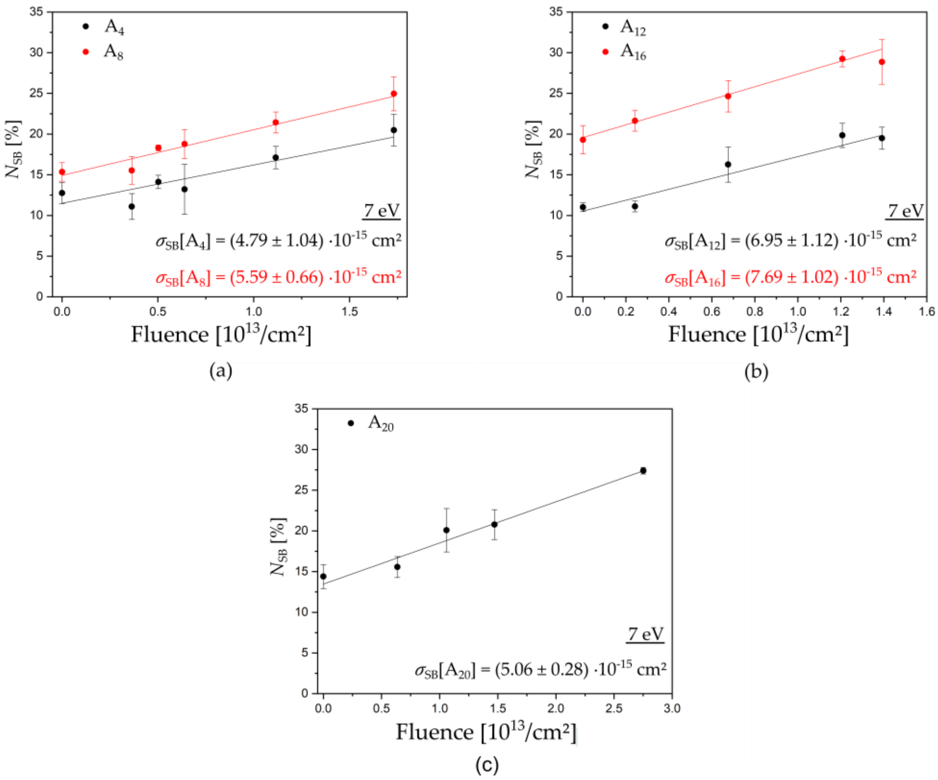

(a) (b)

(c)

Figure 4.1 Examples of exposure response curves to determine the absolute DNA strand break cross section for ssDNA. The diagrams show the results of the irradiation at 7 eV electron energy for the five oligonucleotide sequences (**a**) A_4 (black) and A_8 (red), (**b**) A_{12} (black) and A_{16} (red), and (**c**) A_{20} (black). The absolute strand break cross section σ_{SSB} can be obtained from the linear fit of the fluence F and the dependence of strand breakage N_{SB}.

a) Electron energy dependence of strand break cross sections

All determined SB cross sections σ_{SSB} are shown in figure 4.1 as a function of electron energy between 5 and 10 eV. The highest σ_{SSB} is determined for A_{16} in the regime of 10^{-15} cm² in all electron energies. Possible DNA base damages below the ionization threshold can occur either by pulsed lasers (~4.6 eV), which results in oxidative damage to the DNA, or at specific electron energies through anion resonances, i.e., TNI states, which can either decay by autodetachment of the extra electron or via dissociation (DEA) [106], [107]. The latter is more likely with longer lifetimes of the generated TNI and dominates over AD [53]. Electrons with certain energy can attach e.g., to base π^* orbitals, which can serve as antennas for low-energy electrons. The formed shape resonances at low electron energies result in a transfer of the extra electron to the DNA backbone and can eventually cleave the sugar-phosphate C-O bond (σ orbital) [80]. The investigated σ_{SSB} for A_4, A_8, A_{12}, A_{16}, and A_{20} exhibit a broad resonant structure peaking at 7.0–8.4 eV. In this energy regime gives rise to various resonant fragmentation pathways to all DNA subunits. Between 7.0 and 8.4 eV, the reactions are mediated by core excited resonances in which the electron attachment is accompanied by an electronic excitation. The low-energy threshold for a core excited resonance in DNA is represented by a π-π* transition at about 4.7 eV, which is the lowest-energy electronic excitation [52]. In the present experiment, the lowest cross sections are observed at 5.0 eV. A similar and strong electron energy dependent signature of SB yield was shown in several studies using plasmid DNA [57], [58], [108]. Compared to the single stranded poly(A) oligonucleotides, plasmid DNA is a double stranded DNA with several thousand base pairs and a complex secondary structure. Authors used several nm thick film of plasmid DNA and exposed them with LEEs. A broad resonance maximum between 7.0 and 13 eV for SSBs is observed, which is comparable with the poly(A) DNA experiments. DNA strand break yields are slightly decreasing at higher electron energies and have a minimum at 14.0 to 15.0 eV. The pronounced peak signature is very characteristic and has been previously observed below 15 eV for condensed phase DNA bases [109], from single-stranded oligonucleotides adsorbed on gold surfaces [110] and immobilized on DNA origamis [14].

The vertical ionization energy (IE) of adenine is 8.4 eV [41]. Therefore, irradiation with LEEs above 8.4 eV, DNA strand breakage could also result from initial ionization of the DNA subunits. Irradiation of the same poly(A) DNA with vacuum ultraviolet (VUV) radiation at 8.4 eV, similar tendencies of the SB cross sections have been observed: $A_4 \approx A_8 < A_{12} < A_{16} \approx A_{20}$. VUV induced strand breaks are initiated by dissociative photo ionization and excitation in the order of 10^{-16} cm^2 [11]. However, irradiation with LEEs yields DNA strand break cross sections, which are one order of magnitude higher (10^{-15}cm^2) than for VUV radiation. This demonstrates the high efficiency of DEA compared to dissociative photo excitation and ionization. Therefore, other processes than DEA are unlikely to contribute to the DNA strand break cross section using LEEs up to 10 eV.

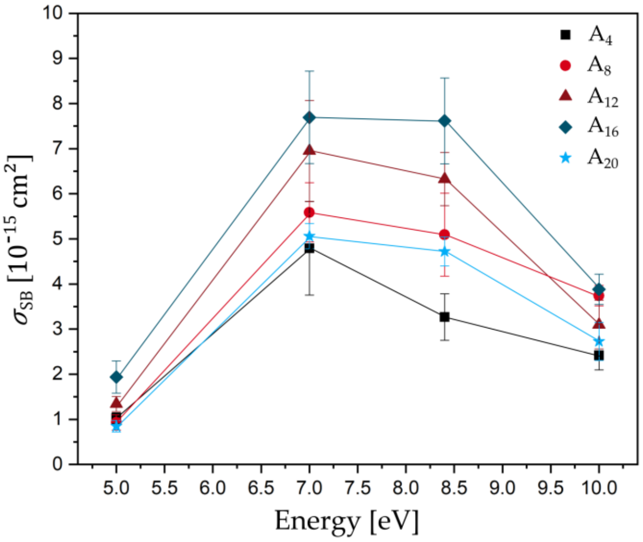

Figure 4.2 Plot of absolute DNA strand break cross section σ_{SSB} for the single stranded polyA DNA sequences A_4 (black-square), A_8 (light red-circle), A_{12} (dark red-triangle), A_{16} (dark blue-diamond), and A_{20} (light blue-star)) as a function of the electron energy. Solid lines connect the data points to guide the eye.

b) Oligonucleotide length dependence of strand break cross sections

Low-energy electron-induced DNA strand breaks strongly depend on the specific oligonucleotide length. It is assumed, that the DNA is likely to be present as A-DNA configuration under the high-vacuum and high-salt conditions during LEE irradiation. The geometrical cross section $\sigma_{N\text{-geo}}$ for each investigated sequence can be estimated by the length of the linear single stranded A-DNA per base (0.24 nm) and a width of 1.15 nm [20] and is compared with the SB cross sections obtained in the LEE irradiation experiments (fig. 4.3). Independently of which molecular model of DNA conformation is used, an increase of the DNA strand break cross section with the oligonucleotide length is expected. This is because of a greater number of possible DNA bond breakages and a higher probability of attaching a LEE. Strand breakage is only one possibility of several different reaction pathways upon electron attachment to DNA. Consequently, the estimated geometrical cross section is about one order of magnitude higher than the experimentally determined SB cross sections. Figure 4.3 shows the plot of the experimentally determined DNA strand break cross sections σ_{SB} as a function of the number of nucleotides. Only a slight change of σ_{SB} at 5.0 and 10.0 eV with the oligonucleotide length, according to the following row is observed: $A_4 \approx A_8 \approx A_{20} < A_{12} < A_{16}$. The shortest DNA sequences with four and eight nucleotides have an almost identical cross section and only a moderate increase from eight over 12 to

16 nucleotides is determined. A stronger effect for σ_{SB} is observed for electron energies to the maximum of negative ion resonances at 7.0 and 8.4 eV. There is a clear dependence in σ_{SB} of the oligonucleotide length with the following tendency: $A_4 < A_8 \approx A_{20} < A_{12} < A_{16}$, with an initial slope similar to the geometrical cross section $\sigma_{N\text{-geo}}$. Nevertheless, the SB cross sections per nucleotide σ_N (table 4.1) vary strongly for the irradiation energy and each sequence length from 0.43 to $11.98 \cdot 10^{-16}$ cm². σ_N should be the same for all DNA sequences under the assumption that each nucleotide is equivalent. This indicates no additive effect of the specific nucleotides and the DNA strand break cross section can be calculated for each electron energy.

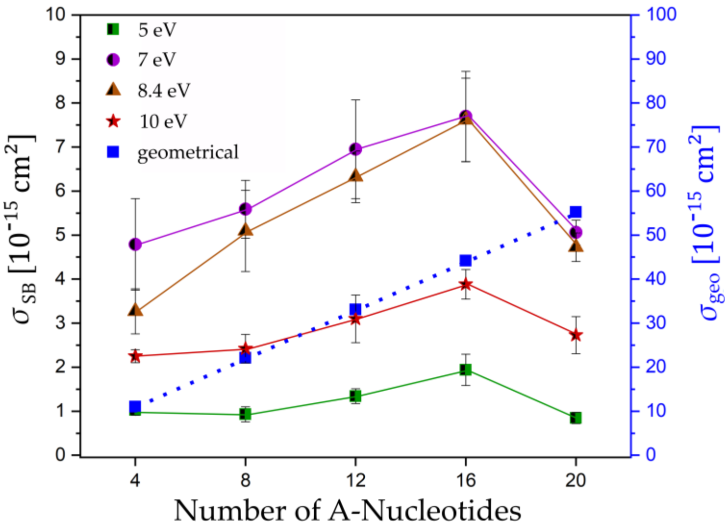

Figure 4.3 Absolute cross section for SBs σ_{SB} (black) and the estimated geometrical cross section $\sigma_{N\text{-}geo}$ (blue) for all poly(A) DNA sequences 5′-d(A_n) $n = 4, 8, 12, 16, 20$ irradiated at 5.0, 7.0, 8.4, and 10 eV plotted against the number of nucleotides. Solid and dotted lines connect the data points to guide the eye.

Table 4.2 Summary of absolute SB cross sections per nucleotide for experimental data σ_N and geometrical cross section $\sigma_{N\text{-geo}}$ calculated from the determined values in table 4.1.

Sequence	SB CS per nucleotide σ_N (10^{-16} cm^2)				$\sigma_{N\text{-geo}}$ (10^{-16} cm^2) per nucleotide
	5 eV	7 eV	8.4 eV	10 eV	/
A_4	2.58	11.98	8.18	5.63	27.60
A_8	1.16	6.99	6.36	3.03	27.60
A_{12}	1.12	5.79	5.27	2.58	27.60
A_{16}	1.21	4.81	4.76	2.43	27.60
A_{20}	0.43	2.53	2.36	1.37	27.60

The cross section for the longest DNA sequence A_{20} does not continue the increasing trend, but decreases significantly in all electron energies. Tentatively, we assume that this can be ascribed to a conformational change occurring in the longer DNA sequences by forming a symmetric base pair by two A nucleotides. Previously it was shown, that adenine-rich RNA and DNA can form under nearly neutral pH and ammonium ions strong A-duplexes [111] with a basic binding motif for a parallel double-stranded helix (fig. 4.4a). The A-A base paring is mediated by two hydrogen bonds (dotted line) between the amino groups of the A (green) bases, as well as the formation of one hydrogen bond between the oxygen of the phosphate group (yellow) in the DNA backbone and each A base. In total, the A-A base pairing is mediated by four hydrogen bonds supported by the stabilization through the present cations (purple). For DNA sequences with a certain length, the Coulomb repulsion of the DNA backbone becomes too weak to further establish a linear structure. Due to the presence of 150 mM Mg^{2+} and a pH of 8.0 in the present experiment, the A_{20} DNA reaches a certain length where a conformational change is feasible. Based on this assumption, the conformational change of A_{20} results in a formation of a DNA hairpin with at least three to four nucleotides in the loop and eight A-A base pairs. An illustration of the conformational change if the DNA reaches a certain length is given in figure 4.4b. Calculations of the salt adjusted melting point T_m from the postulated DNA hairpins would be close to room temperature and is therefore stable [112]. Going to shorter DNA sequences with a lower number of nucleotides, T_m is too low to be stable in this conformation. One can assume in the first approximation that σ_N for the A_{20} increases compared to the shorter DNA sequence A_{16}. The decrease of the SB cross section can be explained by the higher stability of the DNA hairpin due to the additional hydrogen bonds and the cation stabilization. In the event of a possible SSB process in the DNA hairpin, the broken sequence with the biotin label could remain on the DNA strand and subsequent AFM analysis is then not able to detect this SSB. This results in a smaller DNA strand break cross section for coiled ssDNA. *Rackwitz et al.* already examined DNA length dependencies of SB cross section of G-rich telomere sequences with two (5'-d(GGG ATT)$_2$), three (5'-d(GGG ATT)$_3$), and four repeat units (5'- d(GGG ATT)$_4$) upon LEE irradiation with 10 eV electron energy. The authors found a length dependence with increased sensitivity for longer oligonucleotides with more repeat units. G-rich telomer sequences are also able to change their conformation by forming G-quadruplexes in presence of cations. Different cations with different radii can influence the intermolecular shape of the G-quadruplexes. The DNA strand break cross sections in the telomer sequences do not follow exactly a linear function due to the change in the secondary structure. It can be expected that the probability of folded structures is lower for shorter sequences (5'- d(GGG ATT)$_2$ and 5'-d(GGG ATT)$_3$), than for longer sequences like 5'-(GGGATT)$_4$.

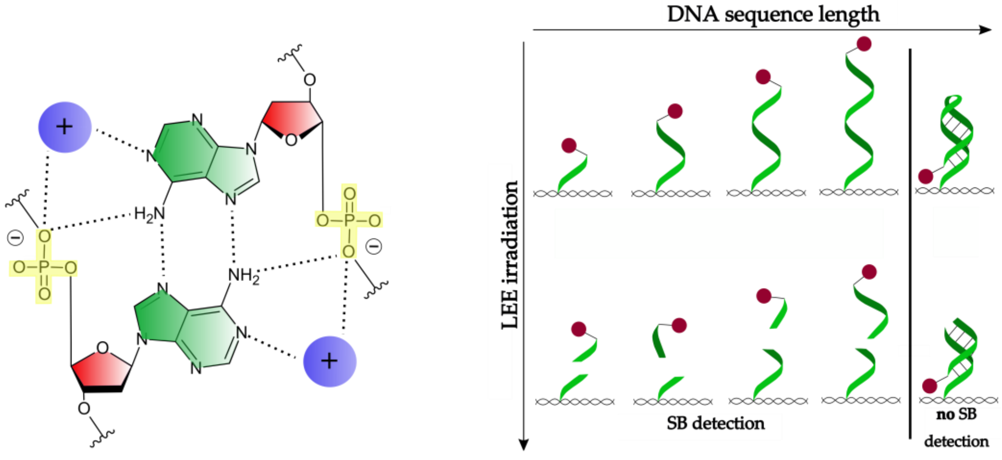

(a)

(b)

Figure 4.4 Illustration of the A-A (green) base pair attached to the deoxyribose sugar unit (red) that builds the A-A duplex in the presence of cations (purple). The phosphate groups (yellow) are driven toward the axis of the helix and form two of the total four hydrogen bonds (dotted lines) [25]. (b) Scheme of the conformational change of a single-stranded DNA with increasing length and SB formation. DNA origami is depicted as a pattern in black, the biotin label a spot in red, and the hydrogen bonding is labeled as a solid line in black.

In the following, we will discuss the magnitude of determined absolute cross section values σ_{SB}, which are in the order of 10^{-15} cm^2 for LEE-induced DNA breakage. *Panajotovic et al.* determined effective cross sections for the production of SSBs in supercoiled plasmid DNA upon irradiation with LEEs between 0.1 to 4.7 eV [113]. The associated effective SSB cross sections per nucleotide σ_N are in the order of 10^{-18} cm^2/nucleotide at 1 and ~2 eV electron energy. A similar value for σ_N was obtained afterward for the absolute cross section for loss of supercoiled DNA upon irradiation with 10 eV electrons (3.0×10^{-14} cm^2 for the whole plasmid corresponding to 4.8×10^{-18} cm^2/nucleotide) [114]. The main assumption in these studies is, that every nucleotide has the same DNA strand break cross section. This would lead to a linear dependence of the total SSB cross section with the length of the plasmid DNA. In the irradiation experiments with polyA DNA, we use DNA strands with 4 to 20 nucleotides, with resulting σ_N values in the order of 10^{-16} to 10^{-17} cm^2/nucleotide. This is one to three orders of magnitudes higher than the previous results obtained using plasmid DNA.

While the present results indicate that a linear length dependence of SB cross sections can be assumed at the maximum of the negative ion resonances and within a certain length regime of the DNA sequence, the SB cross sections per nucleotide still vary strongly. In result, a simple additivity of SB cross sections per nucleotide is not valid (tab. 4.2). Recently, similar observations for absolute vibrational excitation cross section values for thymidine was made and do not correspond to the sum of the cross sections of its constituents [115]. Further experiments are required using e.g., double-stranded DNA, to elucidate the discrepancy in the SB cross sections. The higher conformational stability of the dsDNA over a longer range of strand lengths could support the plasmid DNA results. Furthermore, when comparing the cross section values obtained from the different DNA systems, the potentially different surrounding cations (concentrations and species) and solvating water molecules need to be considered.

4.2 Radiation stability of biotin

a) Bt marker covalently bound to the DNA backbone T-Bt

Biotin is a water-soluble B vitamin (vitamin B_7) and plays a major role in gene expression, is involved in a wide range of metabolic processes and in the cellular response to DNA damage. The heterocyclic ring structure of biotin forms strong intermolecular hydrogen bonds and Van der Waals interactions with proteins such as SAv. The strong non-covalent bond with high affinity is used in the DNA origami technique, which labels the intact DNA target sequences after the irradiation. It was shown, that DEA to biotin results in a decomposition of the ring structure and the carboxyl group in the electron energy range of 0 – 12 eV [116]. In a dry environment by using the DNA origami technique, a dissociation yield of $(1.1 \pm 0.2) \cdot 10^{-14}\ cm^2$ at ≈ 18 eV electron energy was observed by comparing the damage to N_{SB} of a reference sequence 5′-d(SSTT) [116]. The authors considered a Bt damage using the DNA origami technique not only in the energy regime where ionization takes places (>10 eV) but also where DEA mechanism is present (< 1 eV). Since the LEE-induced DNA strand breaks are determined at energies between 5 and 20 eV in this work, a high stability of biotin in this energy and fluence range is required. In view of these results, the biotin damage is observed as a function of the electron energy.

Table 4.3. Overview of the absolute cross sections for SBs (σ_{SSB}) for the DNA sequence T-Bt upon electron irradiation between 5 eV and 20 eV

	DNA SB Cross Section σ_{SSB} [10^{-15} cm^2] of T-Bt					
Energy	**5 eV**	**7 eV**	**8.4 eV**	**10 eV**	**11 eV**	**12 eV**
T-Bt	0.14 ± 0.09	0.25 ± 0.97	0.23 ± 1.93	0.25 ± 1.38	0.50 ± 1.38	0.24 ± 2.93
Energy	**14 eV**	**16 eV**	**18 eV**	**19 eV**	**20 eV**	
T-Bt	0.31 ± 0.62	0.32 ± 2.81	0.38 ± 1.94	0.55 ± 2.04	0.51 ± 0.94	

The DNA origami triangles are modified with a single stranded DNA sequence containing a thymine base and a covalently bound Bt molecule at the 3′ DNA backbone end (5′-d(T-Bt)) denoted as T-Bt. Thymine is used as a spacer to ensure that the biotin is not embedded in the DNA origami triangle and is not covered by the surrounding DNA. The use of the target sequence T-Bt also includes possible DNA single-strand breaks at the thymidine spacer nucleotide. Table 4.3 shows an overview of absolute strand break cross sections for the LEE exposed DNA sequence T-Bt with electron energies between 5 and 20 eV. Compared to longer DNA sequences the σ_{SSB} of the DNA sequence 5′-(T-Bt) are very small. The lowest σ_{SSB} is determined at 5 eV with $(0.14 \pm 0.09) \cdot 10^{-15}\, cm^2$ and the highest at 19 eV with σ_{SSB} $(0.55 \pm 2.04) \cdot 10^{-15}\, cm^2$.

Figure 4.5 shows examples of exposure-response curves for the electron irradiation of T-Bt modified DNA origami nanostructures at energies of 7 eV, 12 eV and 19 eV. A fluctuation of N_{SB} between 10 and 20% is observed independently of F. Non-irradiated control samples show similar values of N_{SB}. This is due to limited purity of the synthesized DNA target sequences, with some of the strands not carrying a Bt marker. Additionally, the binding probability of Bt and SAv is between 80 and 90% on the entire sample. There is no linear dependency between N_{SB} and F in all electron energies from 5 to 20 eV is observed. Linear fitting results in low σ_{SSB} with high error bars. This indicates no Bt damage in the used energy regime between 5 and 20 eV when Bt labels single stranded DNA using the DNA origami technique for determination of absolute DNA strand break cross sections.

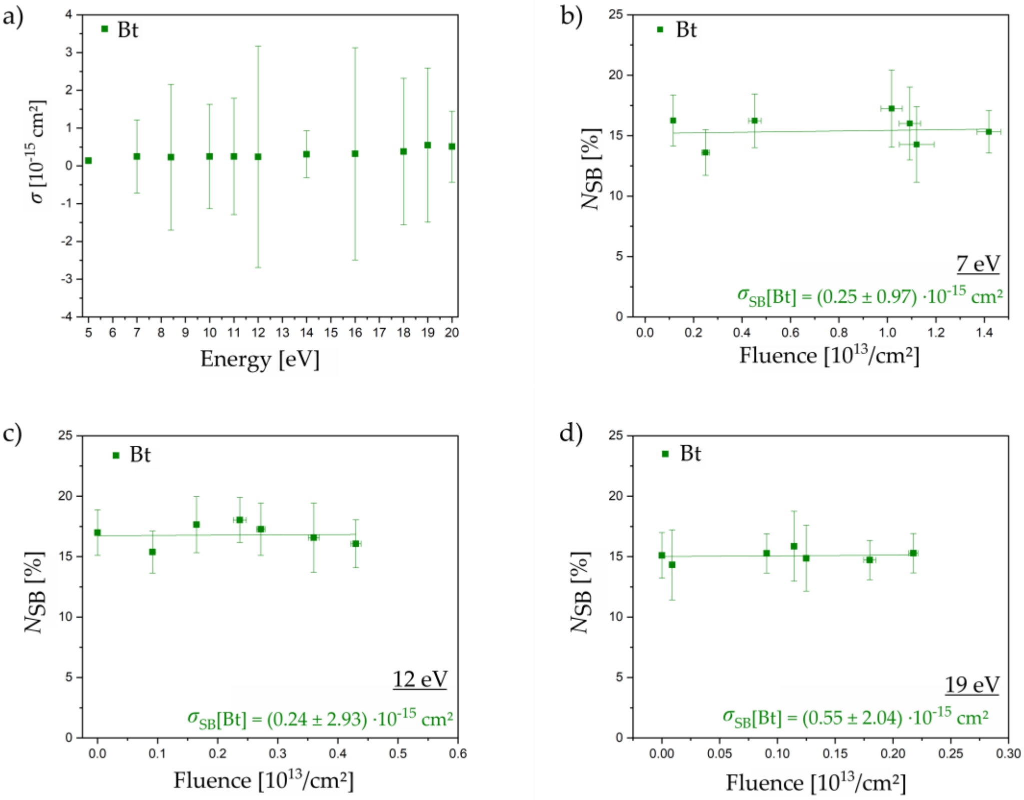

Figure 4.5 a) Plot of absolute DNA strand break cross section σ_{SSB} for the single stranded DNA target sequence T-Bt upon electron irradiation between 5 eV and 20 eV. b-d) Examples of exposure-response curves for the irradiation of T-Bt at electron energies of 7 eV (b), 12 eV (c) and 19 eV (d).

b) *Bt marker covalently bound to the DNA base thymine in HP-Bt*

For ssDNA irradiation experiments, the Bt is bound to the DNA backbone at the 3′ end. In comparison, DNA double strand break experiments use DNA hairpins (chapter 4.3) in which the Bt labeling is required within the DNA strand with Bt bound to the DNA base in the loop. The loop consists of four thymine bases, where the Bt marker was covalently bound direct to one of the DNA bases. Additional control experiments with 5′- d(T_2(Bt-dT)T) have to be made in order to characterize the damage to the hairpin loop and the Bt conjugated to the base. In the following this DNA strand is referred to as HP-Bt (fig. 4.6) and represents the unhybridized loop of a DNA hairpin. The loop consists of four thymine bases, where the Bt marker was covalently bound direct to one of the DNA bases. This modified target sequence is implemented into the DNA origami triangle and irradiated at the same electron energies as in chapter 4.3.

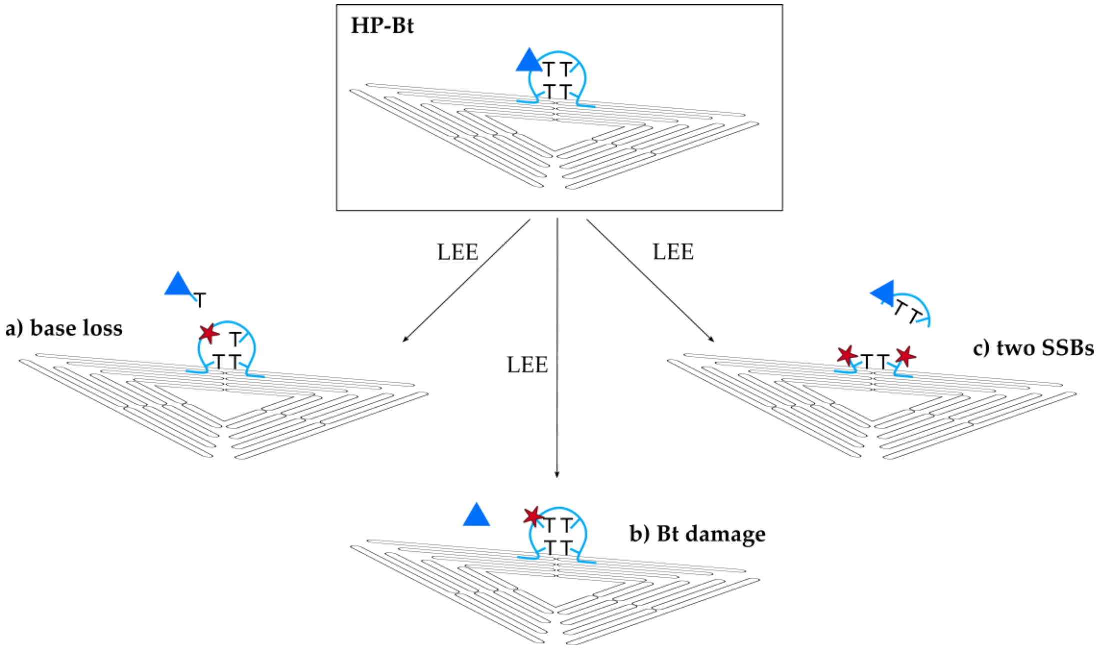

Figure 4.6 Schematic shows various types of HP-Bt damage caused by low energy electrons. a) base loss of the DNA base with Bt label, b) damage of the Bt label, c) two single strand breaks in different positions.

These experiments are intended to determine the stability of the thymine-bound Bt upon the irradiation with LEEs. Possible Bt damage can occur from the loss of the thymine base to which the Bt marker is bound (fig. 4.6a), LEE induced damage to the Bt label (fig. 4.6b) or damaging the DNA hairpin loop via two SSBs (fig. 4.6c). All processes are indistinguishable in the AFM analysis using the DNA origami technique. Whereas the two-electron process from path c results in an exponential dependency of N_{SB} with increasing F due to a lower probability of events.

Table 4.4. Overview of the absolute cross sections for SSBs (σ_{SSB}) for the DNA sequence HP-Bt upon electron irradiation between 5 eV and 20 eV.

	DNA SSB Cross Section σ_{SSB} [10^{-15} cm^2] of HP-Bt					
Energy	**5 eV**	**7 eV**	**8.4 eV**	**10 eV**	**11 eV**	**12 eV**
HP-Bt	0.12 ± 0.12	0.22 ± 0.15	0.25 ± 0.12	0.33 ± 0.16	0.27 ± 0.16	0.19 ± 0.16
Energy	**14 eV**	**16 eV**	**18 eV**	**19 eV**	**20 eV**	
HP-Bt	0.24 ± 0.13	0.21 ± 0.23	0.19 ± 0.17	0.20 ± 0.13	0.23 ± 0.16	

Table 4.4 shows the DNA strand break CS of HP-Bt irradiated at electron energies between 5 and 20 eV. The associated exposure-response curves show a slight

linear increase in N_{SB} with F, whereby σ_{SSB} was found in the range from $(0.12 \pm 0.12) \cdot 10^{-15}\ cm^2$ for 5 eV up to $(0.33 \pm 0.16) \cdot 10^{-15}\ cm^2$ for 10 eV electron energy. This indicates some damage to HP-Bt and is considered in the following irradiation experiments of dsDNA hairpins HP-1.

4.3 LEE-induced strand breaks in dsDNA

The ultimate cell killing by ionizing radiation is not fully understood and hence predictable with the currently available models. For a detailed research, the DNA origami technique is helpful to investigate the mechanism of low energy-electron induced DNA DSBs for well-defined DNA sequences. This enables a direct comparison between LEE induced damage to DNA single and double strands with respective sequences. By using LEEs below 20 eV the DSBs are highly dependent on the initial kinetic energy below 15 eV and an intense peak near 10 eV was observed [58]. Therefore, studying the interaction of double-stranded DNA with LEEs below 20 eV is of great importance for a better understanding of DNA damage. In this work absolute CS of dsDNA are determined with the DNA origami technique for the first time.

Studying the LEE induced DNA double strand breaks, the successful formation of a double strand must be ensured. Therefore, dye labeled DS_{dye} (5'- d$(CAC)_4$-Cy3 and 3'- d$(GTG)_4$-FAM) are placed directly next to each other on the DNA origami triangle (fig. 4.7a). The dye functionalization enables the observation of Förster resonance energy transfer (FRET) [117] between a donor (fluorescein; FAM) and an acceptor dye (cyanine3; Cy3) attached to the ends of the complementary single strands. FRET is a mechanism describing an energy transfer via nonradiative dipole-dipole coupling between two light-sensitive chromophores, which is highly distance-dependent. An overlap of the emission spectrum of the donor with the absorption spectrum of the acceptor dye is required to guarantee an energy transfer. The formation of a DNA double strand of DS_{dye} allows an energy transfer resulting in a characteristic FRET signal in fluorescence emission spectra by exciting the donor dye (450 nm). Figure 4.7c shows the emission spectra of the ssDNA $(GTG)_4$-FAM excited at 450 nm with a maximum at 515 nm (yellow line) and $(CAC)_4$-Cy3 excited at 500 nm with a maximum at 565 nm (red line). Both, free in solution and attached to the DNA origami, no differences in the emission spectra of $(GTG)_4$-FAM and $(CAC)_4$-Cy3 are observed. In contrast to this, the dsDNA DS_{dye} free in solution (fig. 4.7c black dotted line) and attached to the DNA origami (fig. 4.7d black dotted line) show different emission spectra. By exciting the free DS$_{dye}$ at 450 nm, the emission of Cy3 increases at 565 nm. This indicates a successful energy transfer over small distances (1 to 10 nm) between the donor and acceptor dye. If the DS$_{dye}$ is bound to the DNA origami triangle, only a weak energy transfer is observed. This is ascribed to the fact that the two ssDNA did not hybridize when attached to the DNA origami triangles. Moreover, the two single stranded DNA can hinder each other in the folding process because of their close proximity. As a result, only one of the two single stranded DNA could be bound to the DNA origami. Additionally, electron induced DNA strand break experiments of single stranded DNA (5'-d(CAC)$_4$-Bt and 3'-d(GTG)$_4$-Bt; named in the following as (CAC)$_4$ and (GTG)$_4$) and double stranded DNA using complementary single stranded DNA DS (5'- d(CAC)$_4$-Bt/3'-d(GTG)$_4$-Bt) (fig. 4.7a.i) supports the FRET experiments. Almost identical σ_{SB} are obtained for irradiated DNA oligonucleotides (CAC)$_4$, (GTG)$_4$ and DS at an electron energy of 10 eV (fig. 4.7b).

Therefore, the formation of the DNA double strand is ensured by a DNA hairpin HP-1 (5'- d(GTG)$_4$T(Bt- dT)T$_2$(CAC)$_4$). During the annealing process, the DNA hairpin forms a double strand consisting of twelve DNA base pairs and a loop of four non-hybridized thymine bases. The Bt label is covalently bound to one of the thymine bases in the DNA hairpin loop. As shown in chapter 4.2 the Bt label is subject to LEE induced DNA damage itself, which has to be considered in the final strand break yield. Table 4.5 summarizes all experimentally determined DNA strand break CS of dsDNA HP-1 and the two associated ssDNA (CAC)$_4$ and (GTG)$_4$. Due to the instability and the possibility of LEE-induced DNA damage in HP-Bt from chapter 4.2b, σ_{DSB} for HP-1 has to be corrected to consider only the damage of the double stranded sequence. Therefore, σ_{SSB} of HP-Bt is subtracted by σ_{DSB} of HP-1 for each electron energy and is shown as HP-1$_{corr}$.

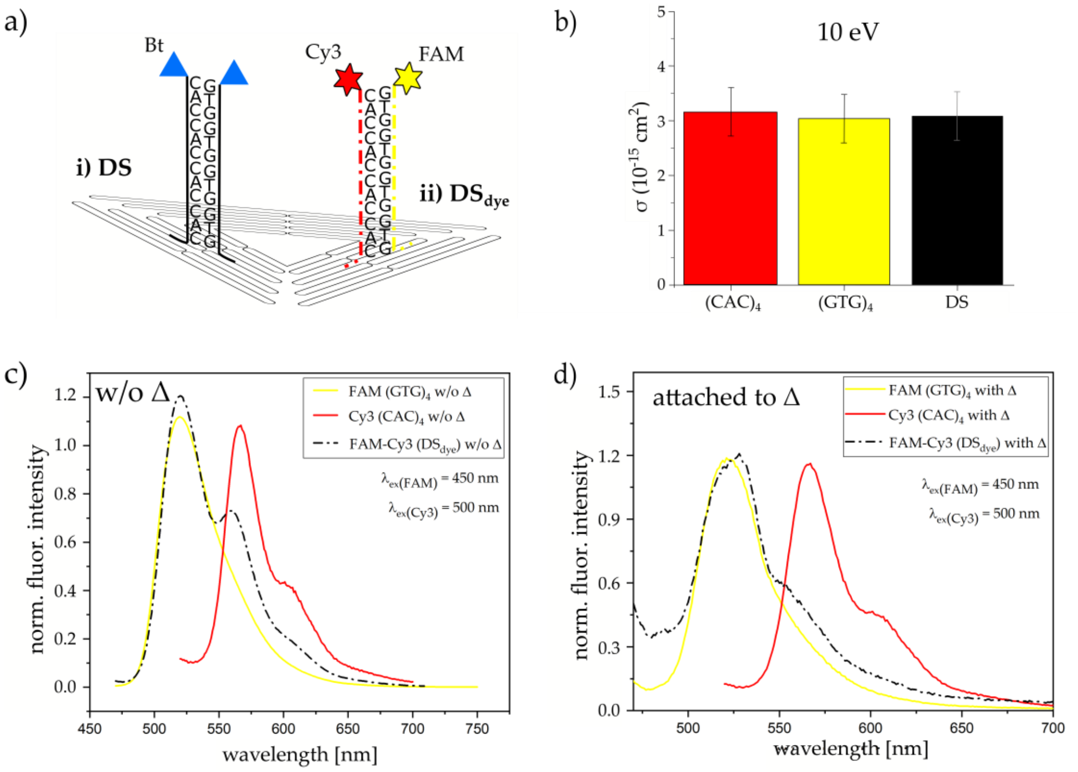

Figure 4.7 a) Illustration of the DNA origami triangle modification with i) DS (5'-$(CAC)_4$-Bt / 3'-$(GTG)_4$-Bt) and ii) DS_{dye} (5'-$(CAC)_4$-Cy3 /3'-$(GTG)_4$-FAM). DS modification is used in the LEE induced DNA irradiation experiments. b) Absolute DNA strand break cross sections σ_{SB} for the DNA single strands (5'-$(CAC)_4$-Bt and 3′-$(GTG)_4$-Bt) and the DNA double strand DS (5'- $(CAC)_4$-Bt / 3'- $(GTG)_4$-Bt). Determined σ_{SB} [10^{-15} cm^2] for LEE irradiation at 10 eV: $(CAC)_4$ (3.10 ± 0.41), $(GTG)_4$ (3.00 ± 0.32) and DS (3.08 ± 0.36). c) Results of the two-dye FRET system with FAM and Cy3 as donor and acceptor not attached to the DNA origami triangle. The normalized fluorescence emission spectra of the single stranded DNA $(GTG)_4$-FAM (yellow; excited at 450 nm; maximum at 515 nm) $(CAC)_4$-Cy3 (red; excited at 500 nm; maximum at 565 nm) and the hybridized double stranded DNA DS_{dye} (black dashed line; excited at 450 nm). The emission spectra of DS_{dye} show the emission of FAM and Cy3 due to energy transfer from donor to acceptor dye. d) Two-dye FRET system with FAM and Cy3 modified DNA target sequences $(GTG)_4$-FAM and $(CAC)_4$-Cy3 as donor and acceptor attached to the DNA origami triangle. The emission spectra of DS (dashed line; excited at 450 nm) show the emission of FAM at 515 nm and only a small increase of Cy3 emission at 565 nm. This indicates a less favorable hybridization of DS compared to DS_{dye} when not attached to the DNA origami triangle.

Table 4.5 Summary of σ_{SSB} for the ssDNA $(CAC)_4$ and $(GTG)_4$, as well as σ_{DSB} for the dsDNA HP-1, which are corrected to HP-1$_{corr}$ by σ_{SSB} of HP-Bt from chapter 4.2b upon electron irradiation between 5 eV and 20 eV.

DNA SB CS σ_{SSB} and σ_{DSB} [10^{-15} cm^2] of $(GTG)_4$, $(CAC)_4$, HP-1 and HP-1$_{corr}$

Energy	**5 eV**	**7 eV**	**8.4 eV**	**10 eV**	**11 eV**	**12 eV**
$(CAC)_4$	2.58 ± 0.37	2.80 ± 0.19	2.60 ± 0.17	3.10 ± 0.41	2.80 ± 0.35	2.10 ± 0.31
$(GTG)_4$	2.44 ± 0.37	2.52 ± 0.36	2.43 ± 0.27	3.00 ± 0.32	2.70 ± 0.27	1.90 ± 0.23
HP-1	0.98 ± 0.29	1.27 ± 0.27	1.32 ± 0.30	1.88 ± 0.17	1.52 ± 0.22	0.80 ± 0.19
HP-1$_{corr}$	0.86 ± 0.29	1.05 ± 0.27	1.07 ± 0.30	1.50 ± 0.17	1.25 ± 0.22	0.61 ± 0.19
Energy	**14 eV**	**16 eV**	**18 eV**	**19 eV**	**20 eV**	
$(CAC)_4$	1.80 ± 0.39	2.20 ± 0.27	2.55 ± 0.40	3.50 ± 0.39	3.55 ± 0.37	
$(GTG)_4$	1.53 ± 0.36	2.07 ± 0.37	2.44 ± 0.49	3.00 ± 0.24	3.20 ± 0.32	
HP-1	0.60± 0.29	1.42 ± 0.27	1.47 ± 0.29	1.52 ± 0.30	1.51 ± 0.36	
HP-1$_{corr}$	0.36± 0.29	1.21 ± 0.27	1.28 ± 0.29	1.32 ± 0.30	1.28 ± 0.36	

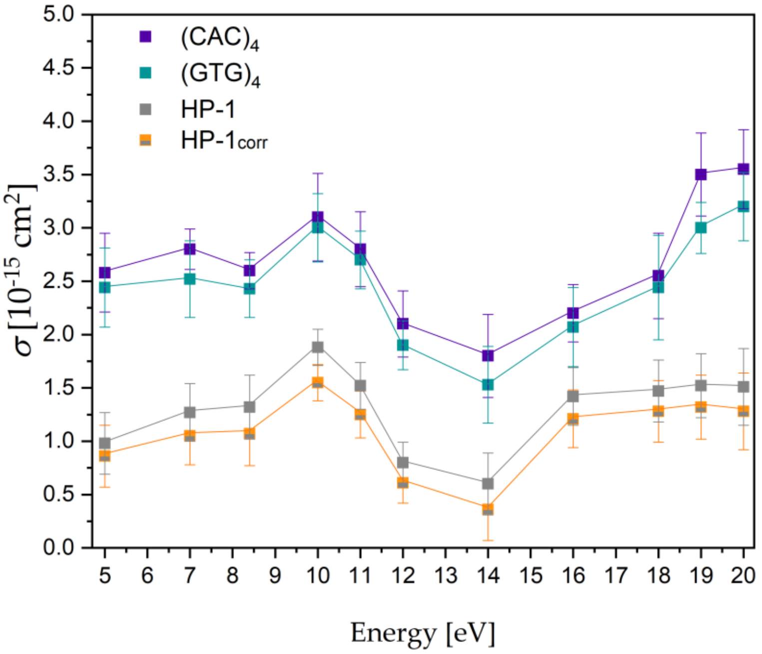

Figure 4.8 Plot of absolute DNA strand break cross section σ_{SSB} for the single stranded DNA sequences $(CAC)_4$ (purple) and $(GTG)_4$ (turquoise) and the absolute DNA strand break cross section σ_{DSB} for double stranded DNA HP-1, which are corrected to HP-1$_{corr}$ by σ_{SSB} of HP-Bt from chapter 4.2b upon electron irradiation between 5 eV and 20 eV.

Table 4.5 gives a summary of the DNA strand break CS for the ssDNA $(CAC)_4$ and $(GTG)_4$ as well as the dsDNA HP-1 and HP-1$_{corr}$. Figure 4.8 shows all obtained values for σ_{SSB} of ssDNA ($(CAC)_4$; purple and $(GTG)_4$; turquoise) and σ_{DSB} for dsDNA (HP-1; grey and HP-1$_{corr}$; orange) at different irradiation energies between 5 eV and

20 eV electrons. There is a clear difference between σ_{SSB} and σ_{DSB} of DNA single and double strands, where the CS for ssDNA are always higher in all electron energies compared to dsDNA. It is known that ionizing radiation produces about 1000 SSBs and 25-40 DSBs per diploid cell per gray (Gy) [118]. Investigation of LEE induced DNA damage with plasmid DNA (pGEM 3Zf(-); 3199 base pairs) also show a four times higher yield of DNA SSBs compared to DNA DSBs [57]. A similar yield is observed in the DNA origami irradiation experiments, in which the probability of a DNA single strand break is a factor of three higher than for a DNA double strand break. This is basically expected, since the probability of breaking a single stranded DNA by a single electron is higher than for a double stranded DNA. *Sanche et al.* proposed possible electron pathways yielding a local multiply damage site (LMDS) with two or more damages within a few helical turns [119], [120]. The LMDS include oxidized purines and pyrimidines, abasic sites and strand breaks induced by a single electron [121], [122], [123]. The initial step is the capturing of the electron by a positive EA of an electronically excited state of a base followed by the formation of a core-excited TNI on the base. The TNI can decay by DEA or autoionization. The latter leaves the base in an electronically excited state resulting in a separation of the additional electron and the electronic excitation. Both can cause a damage on each of the complementary DNA single strands. Path 1 (fig. 4.9) shows the electron transfer from the initial base^{*-} to the base on the opposite strand by forming two adjacent base damages. This electron can further transfer to the phosphate group (path 2) causing rupture the C-O bond via DEA. The electron transfer to the complementary strands (paths 1 and 2) leaves the initial base in a dissociative state leading to C-O bond scission within the same strand (path 3) [124]. An LMDS can still be created by transferring the electron to other bases along the complementary strand within 20 base-pairs from its initial capture (path 4).

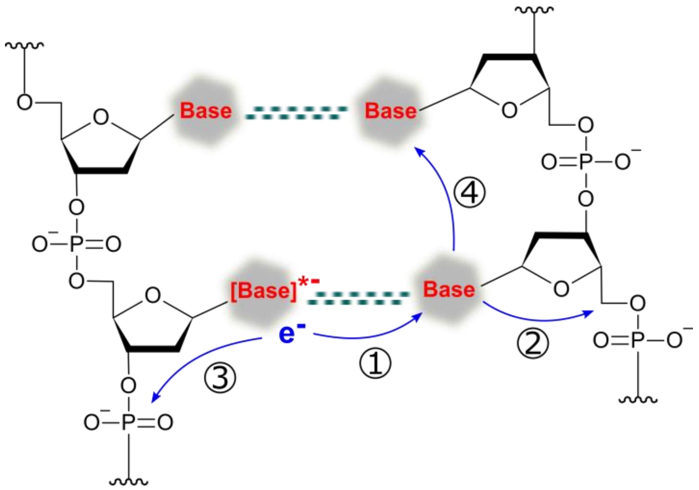

Figure 4.9 Single electron attachment to the base induces a reaction pathway leading in a DNA double strand break. Autodetachment of the initial electron allows it to transfer the electron to the base on the opposite strand (path 1) forming two adjacent base damages. It is further transferring to the phosphate unit, causing a C-O bond rupture (path 2 and 4). The initial base stays in a dissociative state leading to C-O bond scission within the same strand (path 3).

However, the fragmentation mechanism of a DNA double or single strand is not fully understood. DEA studies support the proposed reaction mechanism of *Sanche et al.* with a most likely strand breakage in the C-O phosphodiester bond in the DNA backbone by transferring the excess energy from the nucleobase to the DNA backbone [80]. This energy transfer is due to coupling of the π^* orbital of a cytosine base with a σ^* orbital of the deoxyribose phosphate C-O bond. This is the most fragile bond in the DNA backbone and has been studied intensively by *Simons et. al.* [81], [125], [126], [127]. They investigated the DNA bond breakage induced by LEE whereby the π^* orbital of the nucleobase is only about 1 eV higher than that of the neutral ground state of the glycosidic C-O σ bond with an equilibrium bond length of 1.45 Å.

Additionally, *Wang et al.* concluded by comparing transient photon absorption in solution of DNA bases with that of solutions of nucleotides an attachment of prehydrated electrons specifically to the DNA base. The authors used femtosecond time-resolved laser spectroscopy to study the interaction of prehydrated electrons with deoxyribonucleotide building blocks dXMP (with X = T, A, G, C) consisting of one of the four DNA bases attached to a phosphate unit [128]. The prehydrated state of electrons last for less than a picosecond. Therefore, the free electrons are generated by a pulsed laser in aqueous solution consisting of dXMP. Authors found out that, before hydration of electrons occurred, some of the prehydrated electrons reacted with dXMP to form dXMP$^-$ anions. dGMP and dAMP are more efficient at capturing prehydrated electrons than dTMP and dCMP. Additionally, the generated anions dAMP$^-$ and dCMP$^-$ are stable, whereas dTMP$^-$ and dGMP$^-$ dissociate up to 60% of the total generated anions. Nevertheless, it is unclear how the secondary structure of double stranded DNA affects the formation of base anions. The short DNA sequence in HP-1 enables a maximum of one helical turn formed by twelve base pairs and is held together by hydrogen bonds and stacking interaction. The change of the secondary structure increases the complexity and stability of the DNA strand and could make the electron attachment with a resulting DNA bond breakage more difficult. An alternative hypothesis of a DSB is the formation of two independent, closely opposed SSBs within one helical turn. But in fact, this would lead to a non-linearity in N_{SB} dependency with the fluence F because of a two-electron process. However, this behavior could not be observed in the low energy electron-induced DNA damage experiments using DNA origami nanostructures.

σ_{SSB} and σ_{DSB} have an almost identical shape in terms of energy dependency regardless of the actual value. Electron attachment occurs at specific electron energies below about 12 eV. Anion resonances appear as large changes in σ_{SB}. The strand break cross section for all sequences investigated in this section exhibit a broad resonant structure peaking at 10 eV for $(CAC)_4$, $(GTG)_4$, HP-1, and HP-Bt. A clear shift of resonance to higher electron energies compared to the 7.0-8.4 eV resonance peak of 5'-(A_{12}) ssDNA (chapter 4.1) with the same number of nucleotides is observed. A similar and strong electron energy dependent signature of SB yield was shown in several studies using plasmid DNA [58], [57], [108].

The choice of the nucleotide sequence and its neighboring bases influences the resonance peak position and its absolute value. When comparing different ssDNA with the same nucleotide length, clear differences were found in the absolute σ_{SSB} ($A_{12} = (6.95 \pm 1.12) \cdot 10^{-15}$ cm^2 for 7 eV and $(CAC)_4 = (3.10 \pm 0.41) \cdot 10^{-15}$ cm^2 for 10 eV) within their resonance peak. σ_{SSB} for DNA sequences with the same type of DNA nucleobases (A_{12}) is about double as high than for DNA sequences with alternating bases $(CAC)_4$ with respect to their resonance energy. The electronic properties of dsDNA can be strongly influenced by π-π stacking interactions of the same neighboring bases [129]. *Sugiyama et al.* demonstrated for N-methylated stacked nucleobases, where the interaction between two HOMO (highest occupied molecule orbital) orbitals of adjacent nucleobases in the neutral DNA create an energy splitting by generating a new HOMO of lower and a second HOMO-1 of higher energy [130]. Especially in telomer sequences [131] a charge transfer from a guanine stack to a neighboring adenine is proposed, resulting in a slightly positively charged G, which then can act as an electron antenna [132]. This increases the strand break cross section by a higher affinity towards LEE with increasing DNA sequence length [133]. The π - π stacking interactions strongly dependent on the geometry and the orientation of the DNA bases to one another. Therefore, the stacking interactions in dsDNA are significantly higher than in the more flexible ssDNA. However, there is an influence on the electronic properties of the same neighboring bases even if the bases are not perfectly aligned in ssDNA. This indicates a sequence dependence because of stacking interactions of the stacked adenine bases (A_{12}) compared to the alternating $(CAC)_4$ or $(GTG)_4$ oligonucleotides. Furthermore, the type of DNA bases does not seem to make any difference for σ_{SSB} as long as there are no stacked neighboring bases of the same type.

In LEE experiments with double stranded plasmid DNA on several nm thick films a very strong electron energy dependent signature of SBs is observed. The authors show a broad resonance between 7 and 13 eV for DNA single strands, followed by a minimum at energies of 14 to 15 eV [57]. In contrast to the SSB yield, the DSB yield drops totally to zero at this energy. In the DNA origami experiments the DSB yield is still non-zero in this energy regime and the smallest σ_{DSB} for HP-1 $(0.60\pm 0.29)\cdot 10^{-15}$ cm² is observed. The DNA damage above 14 eV corresponds to the non-resonant mechanisms of DNA strand breakage. Figure 4.8 shows a rise of both the SSB and DSB yields above 14 eV. σ_{DSB} reaches a plateau at 16 eV with similar values as at 10 eV, whereas σ_{SSB} is rising monotonically and no plateau is observed within the studied energy range for the SSBs. Within these energies, single ionization (eq. 4.1) with dissociation can lead to formation of reactive transients (eq. 4.2).

$$e^- + RH \rightarrow (RH)^{*+} + 2e^- \tag{4.1}$$

$$(RH)^{*+} \rightarrow R^+ + H^\bullet, \text{or } R^\bullet + H^+ \tag{4.2}$$

One positive ion is formed in a highly dissociative state $(RH)^{*+}$, then a radical and a cation are formed which may induce further damage to DNA components. The thermodynamic reaction threshold depends on the bond dissociation energies D^0 of DNA and is at about 10 eV [134]. Cross sections are expected to be in the order of 10^{-16} cm² for electron-impact ionization of CH_4 molecules [135]. The same σ_{SSB} were found in previous work for vacuum-UV induced DNA damage in DNA origami experiments for various DNA oligonucleotides [136]. Although multiple ion fragmentations (eq. 4.3) are possible, which are formed at electron energies below 100 eV with CS even two orders of magnitude lower than reactions in equation 4.2 [137].

$$e^- + RH \rightarrow R^+ + H^+ + 3e^- \tag{4.3}$$

The possibility to form a neutral excited transient in a non-resonant direct scattering excitation of a DNA component (eq. 4.4) leads to the formation of two neutral radicals or a cation and anion (dipolar dissociation) (eq. 4.5).

$$e^-(\epsilon_1) + RH \rightarrow (RH)^* + e^-(\epsilon_2 < \epsilon_1) \tag{4.4}$$

$$(RH)^* \rightarrow R^\bullet + H^\bullet, \text{or } R^+ + H^-, \text{or } R^- + H^+ \tag{4.5}$$

The lowest dissociation energy of the electronically excited state (RH)* indicates the energy threshold for subsequent dissociation. D^0 in DNA components is on average at least 4 eV and requires the ionization potential IP subtracted by the electron affinity EA. All mentioned reactions may lead to bond cleavage above the thermodynamic threshold, which results in a signature similar to that for ionization processes with a monotonical rise of σ_{SB} for energies above 14 eV [138]. This typical shape is due to the direct excitation of the neutral or its cation at any energy above the threshold in the Franck-Condon region. In DEA only a specific Franck-Condon overlap between neutral and anionic state for the initial electron capture is allowed for specific electron energies resulting in a sharp peak of σ_{SB}.

4.4 2'-fluoro-2'-deoxycytidine ^{dF}C

In addition to molecules that protect DNA from electron radiation, e.g. ectoine [139], there are also a group of radiosensitizers that intensify the harmful effects of radiation. Gemcitabine is an established drug in medicine and creates an irreparable error that leads to inhibition of further DNA synthesis and thereby leading to cell death when incorporated into DNA strands. The cytotoxic effect of Gem can be additionally increased by simultaneous irradiation of the cells or tissue [140], [141], whereas the precise mechanism of this potential radiosensitization remains unknown. Nevertheless, therapy with Gem is associated with a wide range of adverse effects, including loss of white and red blood cells, suppressing bone marrow function, loss of thrombocytes and difficult breathing. Therefore, new potential drugs, especially radiosensitizers, are always being researched. A commercially available analogue to Gem is 2'-fluoro-2'-deoxycytidine (^{dF}C) (fig. 2.9). In this work, well defined DNA tetramers with (5'- d(GC^{dF}CC)-Bt and 5'- d(^{dF}CGCC)- Bt) and without fluorine modification (5'- d(GCCC)-Bt and 5'- d(CGCC)- Bt) are attached to DNA origami triangles. The DNA oligonucleotides are named by their DNA base sequences as follow GC^{dF}CC, ^{dF}CGCC, GCCC and CGCC. These experiments provide information about the reactivity of the tetramers towards LEEs with 7 and 10 eV electrons. By comparing absolute DNA strand break cross sections, the enhancement factors EF between fluorinated (GC^{dF}CC and ^{dF}CGCC) and non-fluorinated (GCCC and CGCC) sequences are determined.

The sequences GCCC and ^{dF}CGCC are placed on the same DNA origami, as well as CGCC and GC^{dF}CC. At least three series were irradiated with LEEs in the low fluence regime to avoid saturation of N_{SB}. The experiments from chapters 4.1 and 4.3 show resonances at 7 eV (poly(A) DNA) and 10 eV ((GTG)$_4$, (CAC)$_4$ and HP-1). Therefore, all samples were irradiated with 7 and 10 eV electrons in order to generate the greatest possible effect. The exposure response curves (fig. 4.10) of the various tetramers show a linear increase of N_{SB} in dependence of the fluence. From the slope of the linear fit the absolute strand break cross section at 7 eV for GCCC is determined to be $(3.29 \pm 0.25) \cdot 10^{-15}\ cm^2$. The modified nucleotide ^{dF}C increases the strand break cross section of the oligonucleotide GC^{dF}CC towards 7 eV electrons to $(6.80 \pm 0.34) \cdot 10^{-15}\ cm^2$. If the DNA base order is changed to CGCC (σ_{SSB} = $(2.80 \pm 0.15) \cdot 10^{-15}\ cm^2$) and ^{dF}CGCC ($\sigma_{SSB}$ = $(7.03 \pm 0.71) \cdot 10^{-15}\ cm^2$) only a slight change of the DNA strand break cross section is observed.

Table 4.6 Summary of σ_{SSB} for the fluorinated ssDNA GC^{dF}CC and ^{dF}CGCC compared to the unmodified ssDNA GCCC and CGCC upon electron irradiation of 7 eV and 10 eV. The calculated enhancement factors EF and their average EF$_{avg}$ are between 2.07 and 2.51.

Sequence	**ssDNA SB Cross Section σ_{SSB} [10^{-15} cm^2], EF and EF$_{avg}$**				
	7 eV	**EF**	**10 eV**	**EF**	**EF$_{avg}$**
GC^{dF}CC	6.80 ± 0.34	2.07	11.06 ± 0.49	2.31	2.19
GCCC	3.29 ± 0.25		4.78 ± 0.25		
^{dF}CGCC	7.03 ± 0.71	2.51	11.54 ± 0.47	2.28	2.40
CGCC	2.80 ± 0.15		5.07 ± 0.42		

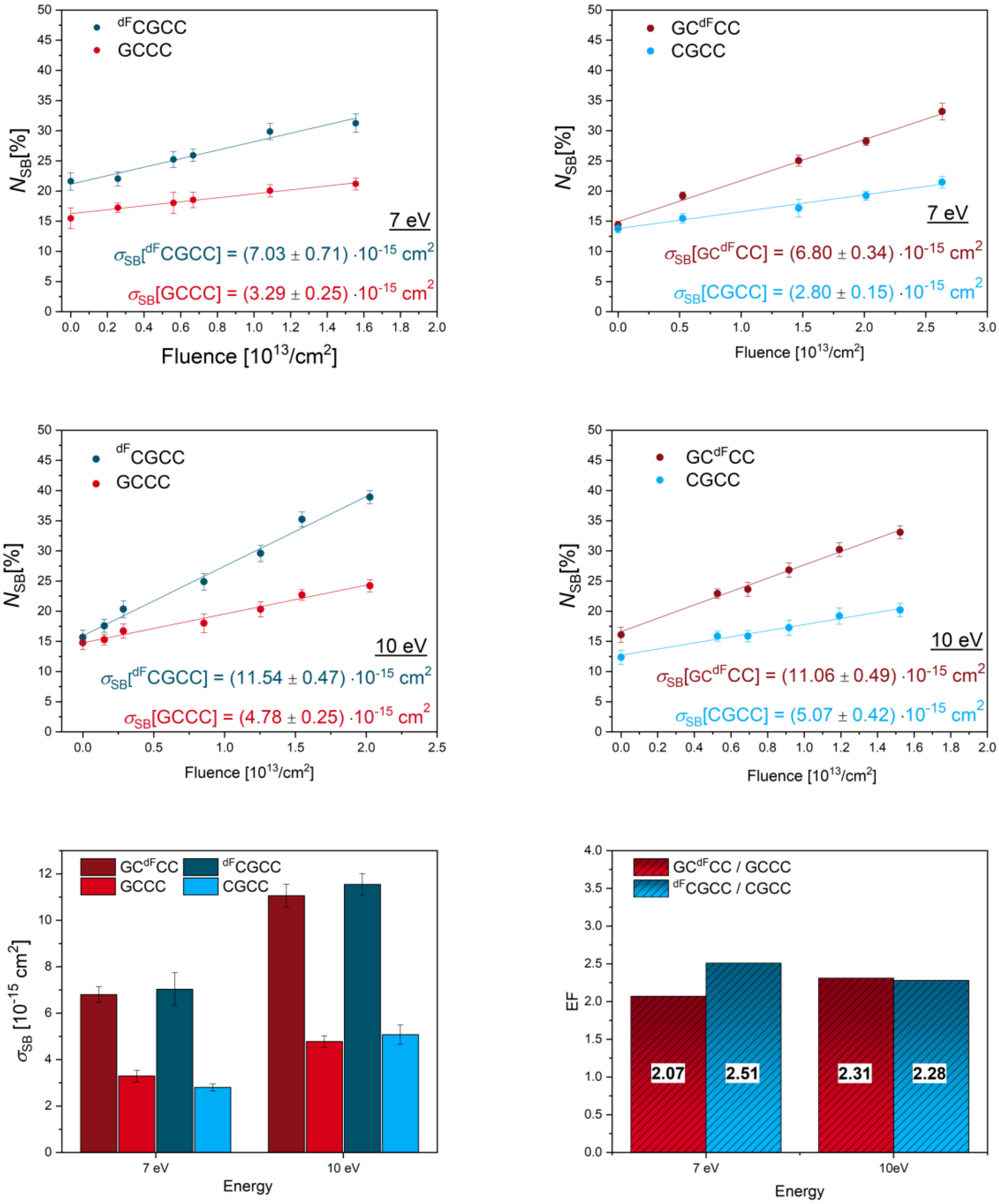

Figure 4.10 Summary of the irradiation experiments with fluorinated (GC^{dF}CC, ^{dF}CGCC) and unmodified (GCCC, CGCC) ssDNA upon 7 and 10 eV electron energy. The determined DNA strand break cross sections σ_{SSB} for the fluorinated sequences are compared to the non-fluorinated sequences. From the ratio of the cross sections, the enhancement factor EF and their averaged EF$_{avg}$ are determined. The highest EF is determined for the sequences ^{dF}CGCC/CGCC with 2.51 at 7 eV electrons.

This indicates that there is no difference in which order the DNA bases are arranged. Choosing an electron energy of 10 eV shows a similar trend with even higher CS. σ_{SSB} for the DNA sequence GCCC is determined to be $(4.78 \pm 0.25) \cdot 10^{-15}\ cm^2$ and its fluorinated oligonucleotide GC^{dF}CC is $(11.06 \pm 0.49) \cdot 10^{-15}\ cm^2$. By rearranging the order of the DNA sequence, σ_{SSB} is determined for the DNA sequence CGCC to be $(5.07 \pm 0.42) \cdot 10^{-15}\ cm^2$ and for ^{dF}CGCC it is $(11.54\ \pm\ 0.47) \cdot\ 10^{-15}\ cm^2$.

Mauracher et al. reported density functional theory studies on the length dependence of electronic properties of DNA single strands consisting of up to eight cytosine and one Gem nucleotide located either at the 5'- or 3'-end [142]. The authors calculated vertical electron affinities (VEA) and vertical ionization energies (VIA). They found an odd-even oscillation for the VEA and VIE for all systems in the gas phase and in a polarizable continuum. The oscillation can be explained by the nature of the closed- and open-shell neutral system of the DNA sequence. Open-shell, neutral single strands form closed-shell anions with lower electron affinity than closed-shell neutral systems. In the case of VIE the closed-shell, neutral molecules are associated with lower VIE than those of open-shell systems due to a stronger binding of the remaining single electron in the HOMO than each of the electrons in the pair occupying the HOMO of the neutral molecule. When introducing sodium counterions to the system according to the number of phosphate groups, the oscillation is completely vanished and only slight changes in comparison to polarizable continuum and gas phase is observed. Due to the high concentration of magnesium counterions in the DNA origami irradiation experiments, the electronic properties (VAE and VIE) of the used DNA sequences are in theory almost identical. This also results in similar σ_{SSB} for the fluorinated (GC^{dF}CC and ^{dF}CGCC) and unmodified (GCCC and CGCC) DNA sequences.

$$EF = \frac{\sigma_{SB}(modified\ DNA\ sequence)}{\sigma_{SB}(unmodified\ DNA\ sequence)} \tag{4.6}$$

The calculation of the enhancement factor EF (eq. 4.6) provides information about the increased sensitivity of the fluorinated DNA sequence towards LEEs of a certain electron energy. Table 4.6 shows the calculated respective EF and its average EF$_{avg}$ between the modified ^{dF}C and unmodified C DNA sequence towards 7 eV and 10 eV electrons. The sensitivity of the oligonucleotide GC^{dF}CC containing the fluorinated nucleobase ^{dF}C is increased by an average factor of 2.19 compared to the unmodified oligonucleotide GCCC. A slightly higher EF$_{avg}$ of 2.40 is obtained for the oligonucleotide ^{dF}CGCC compared to the unmodified DNA sequence CGCC. So far, EF_{avg} for oligonucleotide modification with 2-fluoroadenine ^{2F}A of 1.5 – 1.6 (5.5, 10 and 15 eV) [16] is determined with the same DNA origami technique. The authors used 13mer ^{2F}A modified DNA strands (5'-d(TT(XTX)$_3$TT); X = ^{2F}A) with the fluorine atom at the adenine nucleobase. If X is replaced by 5-fluorouracil ^{5F}U, enhancing effects towards LEE induced DNA damages are observed at specific resonances with values also between 1.5 – 1.6 [16]. However, the sensitivity towards LEEs only becomes clear when considering the energy dependency. Whereas the σ_{SSB} at 10 eV of ^{2F}A ($(13.40 \pm 2.20) \cdot 10^{-15}\ cm^2$) and ^{5F}U ($(13.10 \pm 2.50) \cdot 10^{-15}\ cm^2$)) modified DNA sequences are almost identical, the σ_{SSB} for ^{2F}A ($(21.20 \pm 0.90) \cdot 10^{-15}\ cm^2$) at 5.5 eV are significantly larger than for the ^{5F}U ($(11.70 \pm 1.10) \cdot 10^{-15}\ cm^2$) modified DNA. Therefore, the comparison of EF at specific electron energies is required. Overall, it can be concluded, that the halogenation on the DNA sugar unit increases significantly the sensitivity towards LEEs even with a low ratio between fluorinated and unmodified DNA nucleobases. The halogenation on the nucleobase is improving the antenna effect for the electrons by increasing the electronegativity compared to an H-atom and might draw electron density from the nucleobase leading to DNA backbone decomposition by electron delocalization. However, it must be proven whether the fluorine modification to the DNA sugar unit also leads to high enhancement factors at other energies (< 7 eV and > 10 eV).

4.5 Comparison between manual and software analysis

Using the DNA origami technique, a large data set is analyzed to obtain absolute DNA strand break cross-section at a certain electron energy with high precision. For a sufficient number of DNA origami nanostructures, three series (24 samples) with a total number of 96 AFM images ($4x4\ \mu m^2$, 1024 pixels / line) containing between 15000 – 25000 DNA origami nanostructures are recorded. The AFM images (fig. 4.11a) contain information about topographies on the sample surface, which are indicated by different colors. Black areas can be assigned to the surface background, whereas green areas correspond to the DNA origami triangles on top. *Pythagoras* is able to detect and mark the DNA origami nanostructures based on the triangular shape (fig. 4.11c purple squares) by color and contrast differences. Separated triangles can be detected more easily on the basis of their triangular shape, whereas touching and overlapping triangles are more difficult to detect. Therefore, DNA nanostructures that deviate from a triangular shape are automatically eliminated. *Pythagoras* cannot detect 100% of DNA origamis in the image, what means a sufficient number of AFM images for every sample should be available to ensure a high number of DNA origamis. An update in the software enables detection of triangles touching at the corners (bow tie) by reducing the contrast ratios between background and triangle (fig. 4.11c yellow squares). This increases the amount of detected triangles up to 80% in the entire image compared to only 35% in the first version of the software. Every detected (fig. 4.11d) and ignored (fig. 4.11e) DNA nanostructure is displayed as zoom-in with a masked overlay of the triangular shape and the bright spot of *middle* (m) and *side* (s) positioned streptavidin molecules (fig. 4.11f). However, there are always triangles that are rated as false positive due to incorrect detection of a fictitious triangle (fig. 4.11g) or to wrong SAv spot detection (fig. 4.11h). Therefore, the software has a self-editing function in which every single DNA origami is listed and the results can be edited by hand.

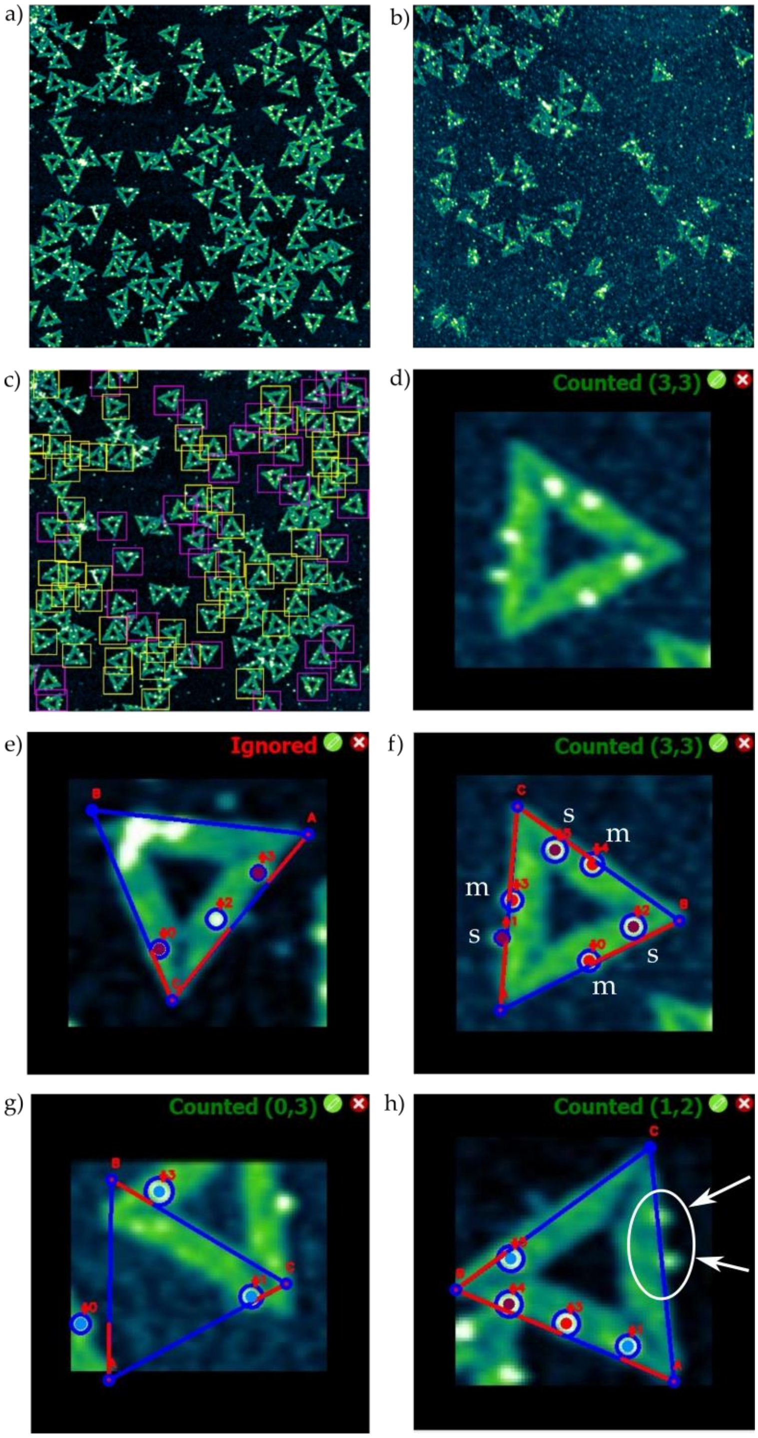

Figure 4.11 a) High quality AFM image. B) Low quality AFM image with damages DNA origami triangles. c) Software detected triangles (yellow and purple squares) with the software Pythagoras. d) Zoom-in of a well-formed DNA origami triangle. Bright spots represent intact DNA strands bound to streptavidin. e) Detected and automatically ignored triangle. f) Same triangle as in d) with a mask overlay, showing the detected SAv spots. The correct detection of the side and middle position results in (3/3) counting. g) Incorrect detection of a triangle. Additionally, the triangle is counted as (0/3). h) The low contrast between triangle surface and SAv spots leads to a failure in SAv spot detection (white circle).

Figure 4.12 shows exposure-response curves and the associated σ_{SB} for manual, software and manually editing of the software (edit) detected DNA single strand breaks N_{SB}. It is assumed, that the detection of the SAv spots is heavily dependent on the quality of the AFM image and that of the position of the target sequences on the DNA origami triangle. Therefore, the diagrams are subdivided in results for *middle* position with high (4.12a) and low quality (4.12c) and as well in *side* position with high (4.12b) and low quality (4.12d) AFM images. An example of a good quality AFM image is given in figure 4.11a with well-formed triangular DNA origamis and bright SAv spots on top. Damaged or destroyed DNA nanostructures with low contrast between triangle and SAv are characteristics of low quality images (fig. 4.11b). Randomly adsorbed SAv and salt crystals over the whole sample surface due to insufficient washing of the samples are also indices for low quality samples.

high quality images

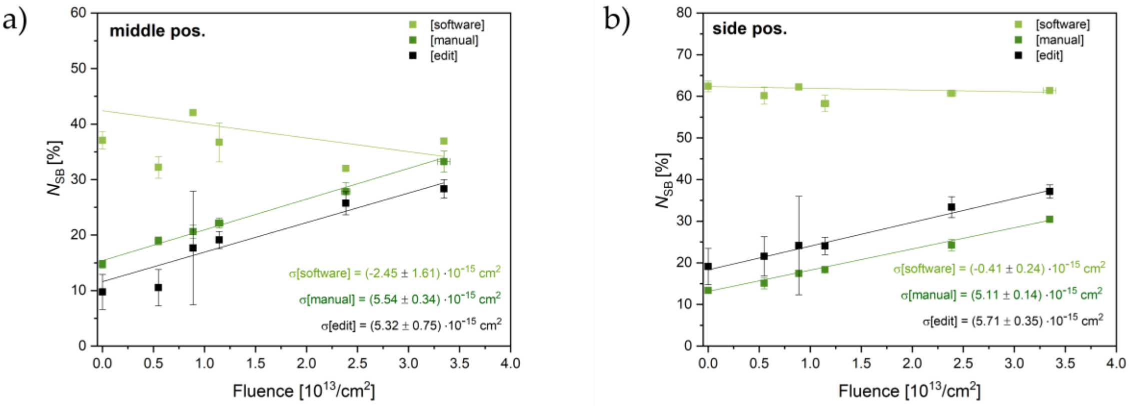

low quality images

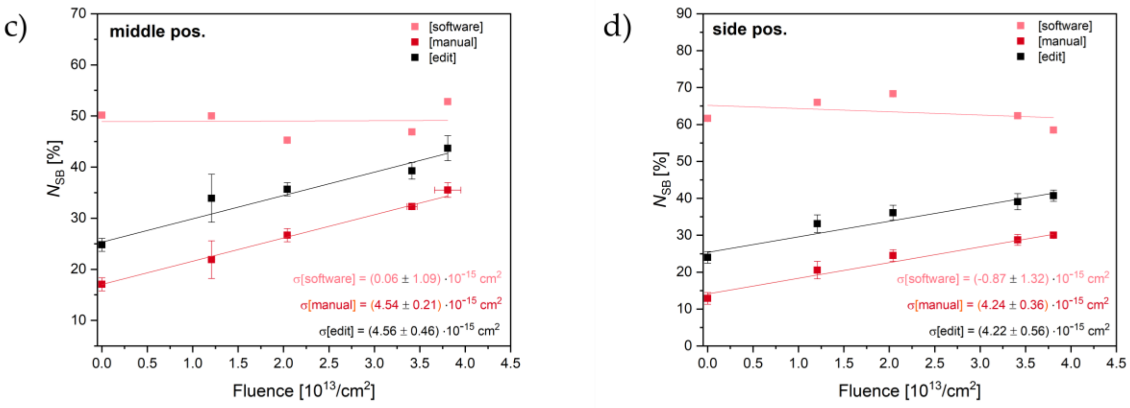

Figure 4.12 Exposure-response curves and the associated σ_{SB} for manual counting (green/red), software analysis (light green/light red) and manually editing (black) of the software detected DNA single strand breaks N_{SB}. The diagrams are subdivided in results for *middle* position with high (a) and low quality (c) and as well in *side* position with high (b) and low quality (d) AFM images.

Pythagoras_v2.0 simplifies the analysis by considering only the marked triangular areas, which eliminates randomly adsorbed streptavidin molecules on the sample surface. The detection of SAv is made by contrast differences of the green DNA origami nanostructure and the bright spots. Based on the fixed positions of the SAv molecules on the trapezoids, the software can distinguish between the *middle* and *side* position by measuring the distance between the centers of the detected SAv area and the closest corner of the triangle. Thus, the *side* position is characterized by a shorter distance to the nearest corner than for the central position to the same corner. If a certain distance between the *side* position and nearest corner is below a threshold value, the SAv spot is not included in the statistics. This occurs when SAv is bound non-specifically to blunt-ends in the gaps of the triangle corners. For this reason, it is expected that the detection of the *middle* position is more reliable.

Table 4.7 Summary of σ_{SSB} for random ssDNA determined manual, by the software Pythagoras, and manual edited software results for high and low quality AFM images, as well as for the side (s) and middle (m) position of the target sequences. The results show different number of detected and counted triangles for the three different analysis methods. The percentage in brackets relates to the software detected triangles.

High quality images			
	manual	**software**	**edit**
Detected triangles	24196	11256	7568
Counted triangles	24196	7568 (67%)	3344 (30%)
σ [10^{-15} cm²]	5.54 ± 0.34 (m) 5.11 ± 0.14 (s)	-2.45 ± 1.61 (m) -0.41 ± 0.24 (s)	5.32 ± 0.75 (m) 5.71 ± 0.35 (s)
low quality images			
	manual	**software**	**edit**
Total triangles	18458	10786	6412
Counted triangles	18458	6412 (59%)	3121 (29%)
σ [10^{-15} cm²]	4.54 ± 0.21 (m) 4.24 ± 0.36 (s)	0.06 ± 1.09 (m) -0.87 ± 1.32 (s)	4.56 ± 0.46 (m) 4.22 ± 0.56 (s)

Table 4.7 summarizes all data of manual, software and software edit analysis. The overall amount of software detected DNA origami triangles is between 45-60% compared to manual detection, depending on the quality of the AFM images. While with manual analysis all detected triangles are included in the statistics, in the software analysis a large part of the detected DNA origami tringles is automatically

removed from the statistics for both high (67%) and low quality (59%) images. Subsequent manual editing of the software detected triangles further reduces the number to only 30% of the usually detected nanostructures from the software regardless of the image quality.

The N_{SB} of the software analysis (light green and light red) is always significantly higher than that of the manual determination and changes slightly with increasing fluence independently of the image quality and positioning. These high values for the strand breakage yield are unusual, as the manual evaluation usually gives values between 10 and 40% with increasing fluence. A non-detection of the SAv spot and thus a higher yield of N_{SB} in the software can have various reasons: i) The contrast ratio between the DNA origami triangle surface and the SAv is too weak and is therefore not recognized by the software. ii) The SAv spot area must exceed a minimum value and fall below a maximum value in order to exclude detection of random contamination. iii) Due to the length of the DNA strand, the SAv spots are not fixed and can be shifted by a few nanometers when it dries on the surface. Since the *side* and *middle* positions are recognized by the software in a specific area, inconsistencies in the definition of the type of position can occur. A high degree of correspondence of the slope between manual and software editing is observed in all high and low quality images, as well as in *middle* and *side* position. This result is to be expected, since the analysis is also based on the manual analysis. The editing feature in the software not only enables the correction of all analyzed nanostructures, but also reduces the processing time of about 30% compared to the manual analysis.

A huge database is generated and enables machine learning in future versions of the software. Independent machine learning leads to an improvement in the software results and, without self-editing, could produce results similar to those of manual evaluation. Normally three weeks are required for the preparation, irradiation and analysis of approx. 25.000 DNA origami nanostructures modified with two different DNA target sequences. The use of fully automatic software without self-editing could reduce the processing time to a third in the future.

4.6 DNA groove binding agents as radiosensitizers

DNA origami nanostructures are considered to be very efficient drug delivery vehicles due to DNA minor groove binding [143]. This property can be used to load DNA origami triangles with different photosensitive DNA binders. Photosensitive DNA binders have a high affinity to the major or minor groove of the DNA double helix. Their affinity for DNA oligonucleotides is based on their non-covalent binding to the DNA strand by ion exchange. The binding is also dependent on the type of the DNA (single or double stranded) and the nucleotide sequence. Light-induced oxidative damage of DNA origami nanostructures modified with 5′-$(GTG)_4$ and HP- 1 covered with low concentrations of the photosensitive DNA groove binders [ANT994], [ANT1083] and $[Cr(ddpd)_2][BF_4]_3$ are analyzed by AFM imaging on the single molecule level. The molecules [ANT994] and [ANT1083] have been synthetized and partially characterized by *Dr. Werner Fudickar* and *Prof. Dr. Thorsten Linker* from the University of Potsdam, Department of Organic Chemistry. The chromium-(III)-complex has been synthetized and characterized *by Prof. Dr. Katja Heinze* from Johannes Gutenberg University of Mainz of the Institute of Inorganic Chemistry and Analytical Chemistry and *Dr. Ute Resch-Genger* and *Cui Wang* from the Federal Institute of Materials Research and Testing from the Division 1.2 Biophotonics. The measurements in chapter 4.6 (fig. 4.16) are made by *Cui Wang*.

a) [ANT994]

A new DNA groove binding agent of substituted 9,10-para-methylpyridiniumanthracen [ANT994] (fig. 2.11a) has been synthesized [96], [98] by *Fudickar et al.* [96]. Its strong minor groove binding mode [144] to DNA AT base pairs is confirmed by DNA melting studies, circular dichroism and the dependence of the binding affinity on ionic strength. The binding constants from poly(dA:dT) are in the range between $1 \cdot 10^4$ and $3 \cdot 10^5$ M^{-1}, whereas no binding occurs to GC sequences. Figure 4.13 shows the optimized docking geometries of [ANT994] to a Dickerson-Drew B-DNA dodecamer. From eight possible docking conformations, seven were found in the minor groove of the DNA with an affinity of -7.3 kcal/mol. [ANT994] has a very weak emission at 530-540 nm in aqueous solution. Upon titration with calf-thymus DNA the intensity increases strongly by the factor of 5 and the maximum emission intensity is blue-shifted compared to the free form. This is rather small compared to other DNA binders [145].

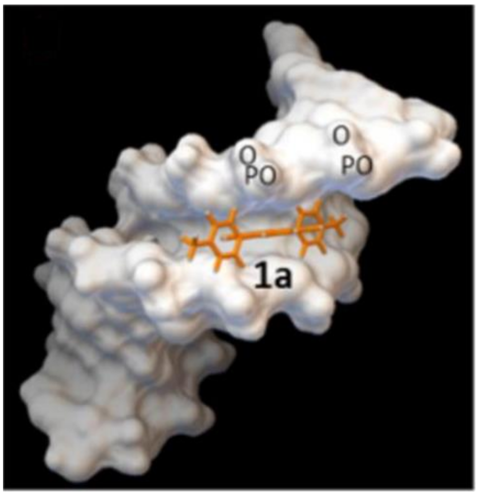

Figure 4.13 Optimized docking geometry of [ANT994] to a Dickerson-Drew B-DNA dodecamer. The letters O (oxygen) and P (phosphor) indicate the positions of phosphate groups. Figure is reprinted with permission from ref. [98].

The groove binding is also supported by DNA melting studies. Whereas intercalation of molecules between DNA base pairs usually enhances the stability of the double helix causing a noticeable rise of the melting temperature T_m, [ANT994] shows no change in the T_m and no intercalation is expected. By insertion into the DNA backbone, the DNA helix becomes lengthened and the diminished extensibility results in a higher melting temperature. Additionally, [ANT994] serve as oxygen carrier by photosensitization from ground-state O_2. It is a chemical source of $^1O_2$ by forming aromatic endoperoxides (EPO) in a defined quantity (fig. 4.14). EPOs achieve a clean release of excited oxygen without remaining oxidation reagents in aqueous solution and dry state, which also favors the determination of DNA damage with the DNA origami technique.

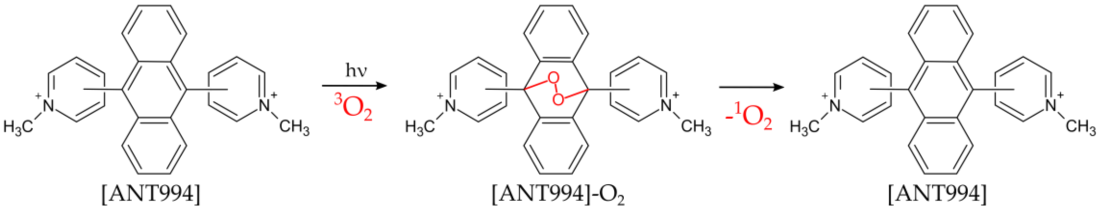

Figure 4.14 Concept of a chemically triggered release of oxygen from EPO [ANT994]-O_2.

DNA origami nanostructures modified with 5′-$(GTG)_4$ and HP-1 are adsorbed on silicon surface as described in chapter 3.1. In addition, 100 and 200 nM of the [ANT994] solution is added and incubated to the DNA triangles for one hour (h). DNA origami triangles modified with the target sequences covered with [ANT994] are irradiated at 530 nm UV-Vis light for one hour in dry state. Figure 4.15 summarizes the N_{SB} of the different target sequences $(GTG)_4$ and HP-1. UV-Vis irradiation of DNA origami triangles modified with the target sequences stay intact and no deformation is observed. By adding [ANT994] to the DNA origami nanostructures in concentrations of 100 and 200 nM, no significant DNA damage is observed independent of the DNA sequence. Only a slightly higher DNA damage is obtained for the 200 nM sample after exposure to UV-Vis light for one hour. However, the DNA damage in both ssDNA ($(GTG)_4$) and dsDNA (HP-1) is very low and can be neglected. If the concentration of [ANT994] is increased to maximize the DNA damaging effect, no intact DNA origami triangles can be obtained. This might be from the groove binding, where the secondary structure of the triangles is disturbed and a deformation occurs. In summary, [ANT994] is not suitable for investigating DNA damage using the DNA origami technique and might not serve as potential photosensitizer since it also has no strong DNA binding affinity.

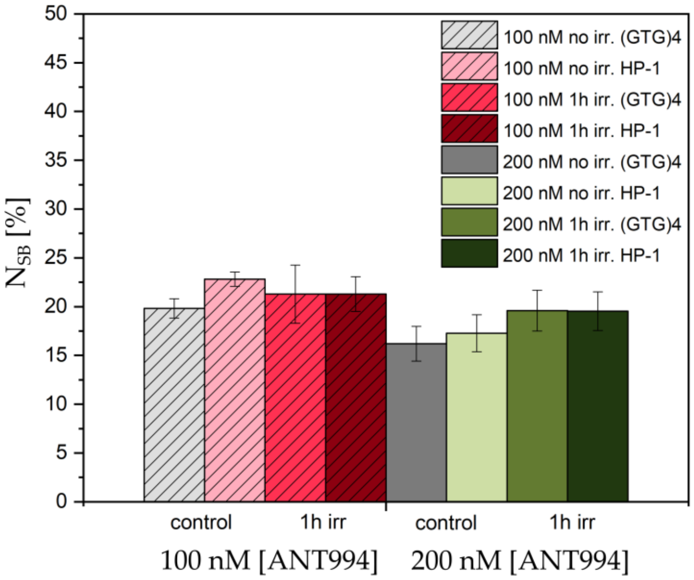

Figure 4.15 Diagram shows the number of strand break N_{SB} from $(GTG)_4$ and HP-1 modified DNA origami triangle covered without and with 100 and 200 nM [ANT994] illuminated for 30 minutes at 530 nm. [ANT994] shows no damaging effect on the target sequences either in 100 or 200 nM concentrations.

b) [ANT1083]

[ANT1083] is a potential new photosensitizer and there are no fundamental studies available at this point. It is expected that the binding strength to DNA increases with the size of the substituents attached at the anthracene site. Therefore, [ANT1083] (fig. 2.11) has a C-C triple bond (alkyne) between the anthracene and the methylpyrimidine substituents. This hinders the rotation of the substituents with a more linear shape than in [ANT994]. Modified DNA origami triangles with $(GTG)_4$ and HP-1 were incubated with 200 nM [ANT1083] and exposed to UV-Vis light (430 nm) up to ten minutes. Irradiated control samples without [ANT1083] incubation stay intact and no deformation was observed upon UV-Vis irradiation independent of the DNA target sequence. The damaging effect of the DNA target sequences are shown in figure 4.16 with a slight increase of N_{SB} over time. It is expected that the binding to double stranded DNA is favored compared to single stranded DNA based on the non-covalent binding due to ion exchange on the DNA backbone in the DNA grooves. As the number of photons from the irradiation source is unknown over time, a precise determination of the DNA strand break cross section is not possible. Additionally, it is unclear, if the photon beam is homogeneous on the analyzed surface area. The increase in strand breakage yield over the irradiation time alone provides information about the DNA damage caused by UV-Vis radiation in combination with [ANT1083]. However, there is no clear difference between the damage of ssDNA ($(GTG)_4$) and dsDNA (HP-1) upon UV-Vis irradiation over time. LEE-induced irradiation experiments proof the higher stability towards radiation resulting in a lower σ_{DSB}. The formation of reactive singlet oxygen is close to the light absorbing PS and in areas that have been exposed to radiation. Since, [ANT1083] binds favorably to dsDNA, the DNA damage of HP-1 increases compared to $(GTG)_4$. This explains the almost identical DNA damages in both target sequences due to randomly accumulated PS on the DNA origami triangle. Nevertheless, [ANT1083] represents a good PS, which is suitable for the investigation of DNA strand breaks with the DNA origami technique. Further experiments in aqueous solution on the sample surface can enhance the effect of the DNA strand breakage using UV-Vis light.

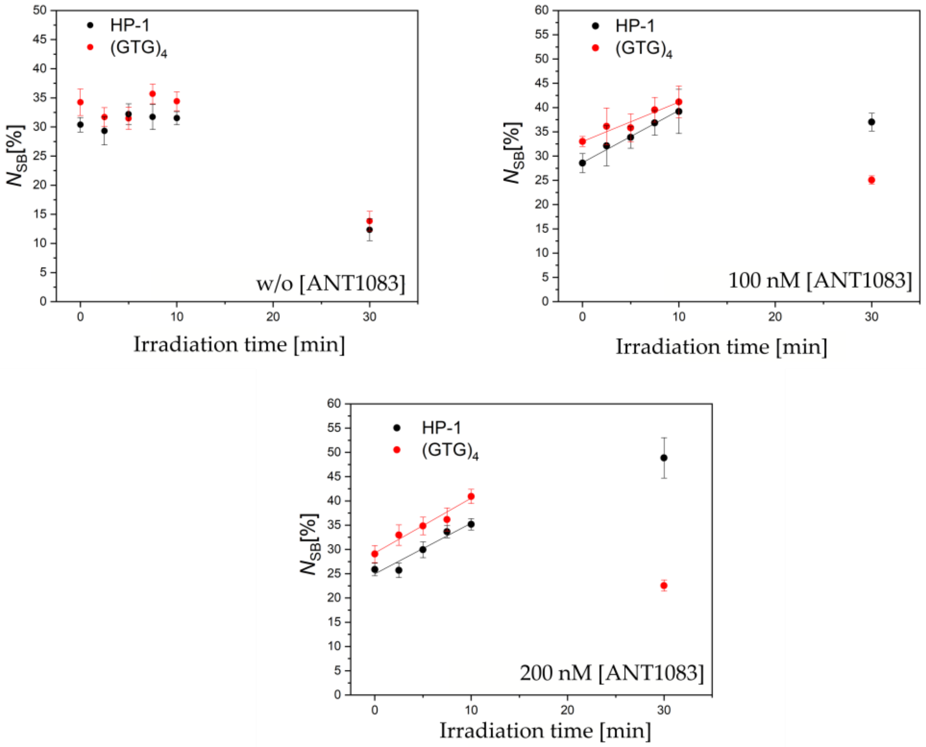

Figure 4.16 Diagram shows the number of strand breaks N_{SB} from $(GTG)_4$ and HP-1 modified DNA origami triangles covered without and with 100 and 200 nM [ANT1083] illuminated for 30 minutes at 430 nm in dry state. [ANT1083] shows a slight damaging effect on the target sequences either in 100 or 200 nM concentrations.

c) *$[Cr(ddpd)_2][BF_4]_3$*

The octahedral chromium-(III) complex is a phosphorescent emitter with long excited state lifetime up to 898 µs in water with corresponding quantum yields of 11% in the absence of O_2 [146]. The formation of singlet oxygen from the excited state and triplet oxygen due to energy transfer has a quantum yield of 61% in DMF. $[Cr(ddpd)_2]^{3+}$ is highly water soluble and stable in high and neutral pH. Upon irradiation with 435 nm LED light, no photodecomposition is observed for at least 5 h. This makes it suitable as PS and can be probed by the DNA origami technique. The same irradiation setup is used as in 4.6 a) and b) with a chromium-(III) complex concentration of 200 nM.

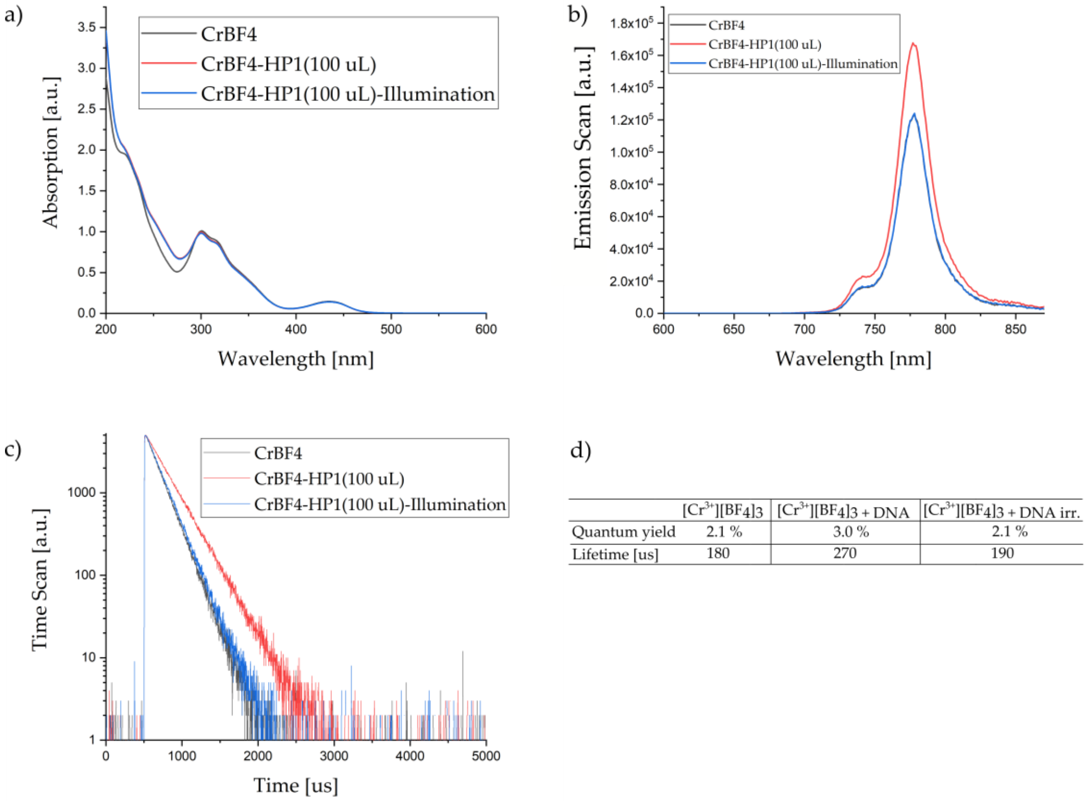

d)

	$[Cr^{3+}][BF_4]_3$	$[Cr^{3+}][BF_4]_3$ + DNA	$[Cr^{3+}][BF_4]_3$ + DNA irr.
Quantum yield	2.1 %	3.0 %	2.1 %
Lifetime [us]	180	270	190

Figure 4.17 a) Absorption spectra from $[Cr(ddpd)_2][BF_4]_3$ (black), in interaction with DNA origami triangles modified with $(GTG)_4$ and HP-1 (red) and after illumination of the chromium-(III) -DNA mixture (blue). b) The associated fluorescence spectra from a). c) Measured timescans with quantum yields and lifetimes (d). All measurements are made by *Cui Wang*.

The absorption band of chromium-(III) with $(GTG)_4$ and HP-1 modified DNA origami nanostructures increases at 260 nm due to the content of DNA. After illumination with 435 nm for one hour, no change in the absorption spectra is observed. Importantly, the emission maximum at 778 nm of the chromium-(III)-DNA origami solution mixture decreases after irradiation with LED at 435 nm to the level of the emission maximum of the chromium-(III) solution alone. The reason for that could be a separation of the chromium-(III)-DNA origami complex in its single components after illumination for one hour. All lifetimes and quantum yields of the different species are summarized in figure 4.17d. Addition of the DNA origami nanostructures to the chromium-(III) complex increases the lifetimes from 180 µs to 270 µs. The associated quantum yield also increased from 2.1 to 3.0% due to the formation of an excited oxygen state. Subsequent irradiation of the mixture shifts the values back to the initial values due to the dissolution of the non-covalent bond of both reaction partners.

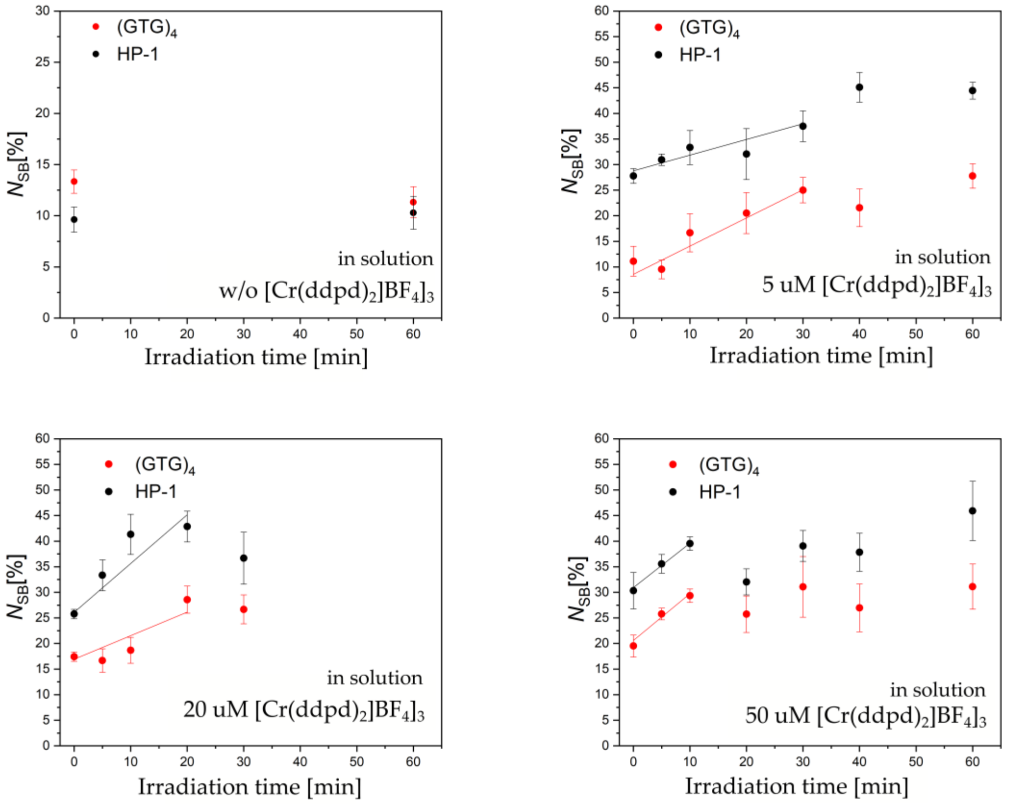

Figure 4.18 Diagram shows the number of strand breaks N_{SB} from (GTG)$_4$ and HP-1 modified DNA origami triangles covered without and with 100 and 200 nM [Cr(ddpd)$_2$][BF$_4$]$_3$ illuminated for 30 minutes at 435 nm in aqueous solution. [Cr(ddpd)$_2$][BF$_4$]$_3$ shows a damaging effect on the target sequences for all concentrations (5, 20 and 50 µM).

LED induced DNA strand breakage using (GTG)$_4$ and HP-1 modified DNA origami nanostructures with 200 nM of chromium(III)-complex in aqueous solution, prove a slightly damaging effect due to the generation of $^1O_2$. DNA damage is caused by the formation of singlet oxygen, since no DNA damage can be obtained in control samples (fig. 4.18a) without a chromium (III) complex. A saturation of N_{SB} is reached faster for higher concentrations (fig. 4.18b-d) of the chromium(III) complex. Mainly, the saturation is caused by interstrand crosslinks on the DNA origami nanostructures, whereas cleaved DNA strands remain on the triangular origami surface. Therefore, shorter irradiation times are useful in future experiments in order to obtain as many data points as possible within the linear increase. Nevertheless, chromium has a high affinity for DNA nanostructures, which can be confirmed by means of emission spectra, lifetimes and quantum yields. In addition, the exposure of well-defined DNA target sequences to LEDs at 435 nm in the presence of the chromium complex causes DNA damage. This means that the $[Cr(ddpd)_2][BF_4]_3$ is also suitable as a photosensitive molecule for use in cell experiments. However, its biocompatibility due to membrane-passing properties because of its hydrophilic ligands still has to be tested and improved [99], [100].

5 Summary and Outlook

In this work the DNA origami technique established by *Keller et al.* [10] is used to investigate electron-induced DNA single and double strand breaks in dependence of the DNA sequence, length and electron energy. Therefore, a novel irradiation setup developed by *Rackwitz et al.* is used to investigate LEE induced DNA strand break yields [16]. The setup and irradiation process were adopted and improved by redetermining the zero point energy of the charged silicon substrates from 2 V to 3.2 V. Additionally, the beam shapes were successfully characterized and optimized for electron energies between 5 and 20 eV, which are required for the energy-dependent radiation experiments. Furthermore, the factor f was determined for each energy in order to obtain absolute fluence values.

Overall, absolute cross sections of DNA single and double strand breaks were determined in the range of 10^{-15} cm^2 in the present work, whereas values in the range of 10^{-16} cm^2 were determined in similar irradiation experiments with VUV photon radiation [11].

A major focus was on the determination of the energy-dependent DNA damage of adenine-rich ssDNA 5'-(A_4), 5'-(A_8), 5'-(A_{12}), 5'- (A_{16}), and 5'-(A_{20}), in which the highest absolute cross sections were determined between 7.0 and 8.4 eV for all sequences. Furthermore, DNA origami triangles were modified with double stranded DNA hairpins HP-1 (5'-d$(CAC)_4$T(Bt-dT)$T_2$$(GTG)_4$) for the first time and their damaging ability upon LEE irradiation in the range of 5 to 20 eV were investigated. Compared to the complementary single strands (5'-d$(CAC)_4$ and 5'-d$(GTG)_4$), a lower CS with a factor of about 3 was determined for HP-1 at every energy. The σ_{SB} for all sequences investigated in this section exhibits a broad resonant structure peaking at 10 eV. This means a clear shift of resonance to higher electron energies compared to the 7.0-8.4 eV resonance peak of 5'-(A_{12}) ssDNA with the same number of nucleotides. A similar signature of the SB yield, which is strongly dependent on the electron energy, was shown in several studies using plasmid DNA and could be supported with these energy-dependent irradiation experiments. The peak position and its absolute value are influenced by the choice of the nucleotide sequence and its neighboring bases.

The fluorination of the sugar unit in the backbone resulting in 2'-fluoro-2'-deoxycytidine leads to a significant increase in the sensitivity towards LEEs at 7 and 10 eV. A low ratio between fluorinated and unmodified DNA nucleobases is sufficient to achieve an enhanced sensitivity upon LEE irradiation. The arrangement and order of the DNA bases is not influencing the DNA damage at all.

DNA origami triangles were loaded with low concentrations of the three different DNA binders [ANT994], [ANT1083] and $[Cr(ddpd)_2][BF_4]_3$ to investigate the light-induced oxidative damage of 5'-d$(GTG)_4$ and HP-1 DNA sequences. When irradiated with UV-Vis light, a damaging effect of the generated singlet oxygen $^1O_2$ in aqueous ($[Cr(ddpd)_2][BF_4]_3$) and dry state ([ANT1083]) could be determined by the DNA binder compared to unmodified DNA origami triangles, whereas [ANT994] did not show any photosensitive effect on single and double-strand modified DNA triangles.

The analysis of the DNA irradiation experiments is supported by the software *Pythagoras* to handle the huge amount of data. We successfully optimized the analysis procedure through time savings of 30%, which can be further improved in the future by generating huge databases for machine learning. If the AFM images are of sufficiently high quality, machine learning can help improving the results to a level that is as good as with manual evaluation even without manual editing. This could reduce the analysis time of an entire experiment with a total of 25,000 DNA origamis triangles from three weeks to only one or two days.

An important chapter of this work deals with the energy-dependent DNA damage of ssDNA and dsDNA between 5 and 20 eV. The current setup has an energy resolution of 1.2 ± 0.07 eV, which means that the results are meaningful due to the minor error in the CS and the good reproducibility of the individual results, but must be viewed with caution due to the weak energy resolution. It is also known that anionic resonances at energies close to 0 eV were determined in DEA gas phase experiments. Therefore, an upgrade of the irradiation setup with an electron monochromator is planned. This is intended to achieve an energy resolution of 100 - 200 meV, which provides a more precise information about energy-dependent experiments. With this setup, the DNA damage of fluorinated compared to unmodified DNA double strands can be examined depending on their electron energy between almost 0 to 20 eV electrons. A good application for this upgraded setup would be the investigation of multiple fluorination in double stranded DNA in dependence of the electron energy.

6 References

1. Sinha, R. P.; Häder, D. P. UV-induced DNA damage and repair: a review. *Photochemical & Photobiological Sciences : Official Journal of the European Photochemistry Association and the European Society for Photobiology.* **2002,** *1* (4), 225–236.
2. Gofman, J. W. *Radiation and human health;* Sierra Club Books.: San Francisco, 1981.
3. Hecht, S. S. Cigarette smoking: cancer risks, carcinogens, and mechanisms. *Langenbeck's Archives of Surgery.* **2006,** *391* (6), 603–613.
4. Hoeijmakers, J.H.J. DNA repair mechanisms. *Maturitas.* **2001,** *38* (1), 17–22.
5. Jeggo, P. A.; Löbrich, M. DNA double-strand breaks: their cellular and clinical impact? *Oncogene.* **2007,** *26* (56), 7717–7719.
6. Torre, L. A.; Bray, F.; Siegel, R. L.; Ferlay, J.; Lortet-Tieulent, J.; Jemal, A. Global Cancer Statistics, 2012. *CA: A Cancer Journal for Clinicians.* **2015,** *65* (2), 87–108.
7. Miller, K. D.; Siegel, R. L.; Lin, C. C.; Mariotto, A. B.; Kramer, J. L.; Rowland, J. H.; Stein, K. D.; Alteri, R.; Jemal, A. Cancer treatment and survivorship statistics, 2016. *CA: A Cancer Journal for Clinicians.* **2016,** *66* (4), 271–289.
8. Hajdu, S. I.; Vadmal, M.; Tang, P. A note from history: Landmarks in history of cancer, part 7. *Cancer.* **2015,** *121* (15), 2480–2513.
9. Pimblott, S. M.; LaVerne, J. A. Production of low-energy electrons by ionizing radiation. *Radiation Physics and Chemistry.* **2007,** *76* (8-9), 1244–1247.
10. Keller, A.; Bald, I.; Rotaru, A.; Cauët, E.; Gothelf, K. V.; Besenbacher, F. Probing electron-induced bond cleavage at the single-molecule level using DNA origami templates. *ACS Nano.* **2012,** *6* (5), 4392–4399.
11. Vogel, S.; Ebel, K.; Schürmann, R. M.; Heck, C.; Meiling, T.; Milosavljevic, A. R.; Giuliani, A.; Bald, I. Vacuum-UV and Low-Energy Electron-Induced DNA Strand Breaks - Influence of the DNA Sequence and Substrate. *Chemphyschem: A European Journal of Chemical Physics and Physical Chemistry.* **2019,** *20* (6), 823–830.
12. Ebel, K.; Bald, I. Length and Energy Dependence of Low-Energy Electron-Induced Strand Breaks in Poly(A) DNA. *International Journal of Molecular Sciences.* **2019,** *21* (1).
13. Rackwitz, J.; Bald, I. Low-Energy Electron-Induced Strand Breaks in Telomere-Derived DNA Sequences-Influence of DNA Sequence and Topology. *Chemistry (Weinheim an der Bergstrasse, Germany)* **2018,** *24* (18), 4680–4688.
14. Schürmann, R.; Tsering, T.; Tanzer, K.; Denifl, S.; Kumar, S. V. K.; Bald, I. Resonant Formation of Strand Breaks in Sensitized Oligonucleotides Induced by Low-Energy Electrons (0.5-9 eV). *Angewandte Chemie International Edition.* **2017,** *56* (36), 10952–10955.

15. Rackwitz, J. *A novel approach to study low-energy electron-induced damage to DNA oligonucleotides. Influence of DNA sequence, topology and nucleobase modification;* Dissertation, 2016.
16. Rackwitz, J.; Ranković, M. L.; Milosavljević, A. R.; Bald, I. A novel setup for the determination of absolute cross sections for low-energy electron induced strand breaks in oligonucleotides – The effect of the radiosensitizer 5-fluorouracil*. *The European Physical Journal D.* **2017,** *71* (2), R287.
17. Watson, J. D.; Crick, F. H. Molecular structure of nucleic acids: a structure for deoxyribose nucleic acid. J.D. Watson and F.H.C. Crick. Published in Nature, number 4356 April 25, 1953. *Nature.* **1974,** *248* (5451), 765.
18. Wing, R.; Drew, H.; Takano, T.; Broka, C.; Tanaka, S.; Itakura, K.; Dickerson, R. E. Crystal structure analysis of a complete turn of B-DNA. *Nature.* **1980,** *287* (5784), 755–758.
19. Michelotti, N.; Johnson-Buck, A.; Manzo, A. J.; Walter, N. G. Beyond DNA origami: the unfolding prospects of nucleic acid nanotechnology. *Wiley Interdisciplinary Reviews. Nanomedicine and Nanobiotechnology.* **2012,** *4* (2), 139–152.
20. Cantor, C. R.; Saenger, W. *Principles of Nucleic Acid Structure;* Springer New York.: New York, NY, 1984.
21. Drew, H. R.; Wing, R. M.; Takano, T.; Broka, C.; Tanaka, S.; Itakura, K.; Dickerson, R. E. Structure of a B-DNA dodecamer: conformation and dynamics. *Proceedings of the National Academy of Sciences of the United States of America.* **1981,** *78* (4), 2179–2183.
22. Zhang, H.; Yu, H.; Ren, J.; Qu, X. Reversible B/Z-DNA transition under the low salt condition and non-B-form polydApolydT selectivity by a cubane-like europium-L-aspartic acid complex. *Biophysical Journal.* **2006,** *90* (9), 3203–3207.
23. Rich, A.; Nordheim, A.; Wang, A. H. The chemistry and biology of left-handed Z-DNA. *Annual Review of Biochemistry.* **1984,** *53*, 791–846.
24. Kroto, H. W.; Heath, J. R.; O'Brien, S. C.; Curl, R. F.; Smalley, R. E. C60: Buckminsterfullerene. *Nature.* **1985,** *318* (6042), 162–163.
25. Keren, K.; Berman, R. S.; Buchstab, E.; Sivan, U.; Braun, E. DNA-templated carbon nanotube field-effect transistor. *Science (New York, N.Y.)* **2003,** *302* (5649), 1380–1382.
26. Gu, Q.; Cheng, C.; Gonela, R.; Suryanarayanan, S.; Anabathula, S.; Dai, K.; Haynie, D. T. DNA nanowire fabrication. *Nature.* **2006,** *17* (1), R14-R25.
27. Seeman, N. C. Nucleic acid junctions and lattices. *Journal of Theoretical Biology.* **1982,** *99* (2), 237–247.
28. Mao, C.; Sun, W.; Seeman, N. C. Designed Two-Dimensional DNA Holliday Junction Arrays Visualized by Atomic Force Microscopy. *Journal of the American Chemical Society.* **1999,** *121* (23), 5437–5443.

29. Yan, H.; Park, S. H.; Finkelstein, G.; Reif, J. H.; LaBean, T. H. DNA-templated self-assembly of protein arrays and highly conductive nanowires. *Science (New York, N.Y.)* **2003,** *301* (5641), 1882–1884.
30. Rothemund, P. W. K. Folding DNA to create nanoscale shapes and patterns. *Nature.* **2006,** *440* (7082), 297–302.
31. Chao, J.; Zhu, D.; Zhang, Y.; Wang, L.; Fan, C. DNA nanotechnology-enabled biosensors. *Biosensors & Bioelectronics.* **2016,** *76*, 68–79.
32. Tan, S. J.; Campolongo, M. J.; Luo, D.; Cheng, W. Building plasmonic nanostructures with DNA. *Nature Nanotechnology.* **2011,** *6* (5), 268–276.
33. Pei, H.; Zuo, X.; Zhu, D.; Huang, Q.; Fan, C. Functional DNA nanostructures for theranostic applications. *Accounts of Chemical Research.* **2014,** *47* (2), 550–559.
34. Tasciotti, E. Smart cancer therapy with DNA origami. *Nature Biotechnology.* **2018,** *36* (3), 234–235.
35. Gauduel, Y.; Pommeret, S.; Migus, A.; Antonetti, A. Some evidence of ultrafast H2O+-water molecule reaction in femtosecond photoionization of pure liquid water: Influence on geminate pair recombination dynamics. *Chemical Physics.* **1990,** *149* (1-2), 1–10.
36. Crespo-Hernández, C. E.; Cohen, B.; Hare, P. M.; Kohler, B. Ultrafast excited-state dynamics in nucleic acids. *Chemical Reviews.* **2004,** *104* (4), 1977–2019.
37. Kuhlmann, A.; Bihr, L.; Wagenknecht, H.-A. How Far Does Energy Migrate in DNA and Cause Damage? Evidence for Long-Range Photodamage to DNA. *Angewandte Chemie International Edition.* **2020**.
38. Nguyen, J.; Ma, Y.; Luo, T.; Bristow, R. G.; Jaffray, D. A.; Lu, Q.-B. Direct observation of ultrafast-electron-transfer reactions unravels high effectiveness of reductive DNA damage. *Proceedings of the National Academy of Sciences of the United States of America.* **2011,** *108* (29), 11778–11783.
39. Pimblott, S. M.; LaVerne, J. A. On the Radiation Chemical Kinetics of the Precursor to the Hydrated Electron. *The Journal of Physical Chemistry. A.* **1998,** *102* (17), 2967–2975.
40. Kumar, A.; Becker, D.; Adhikary, A.; Sevilla, M. D. Reaction of Electrons with DNA: Radiation Damage to Radiosensitization. *International Journal of Molecular Sciences.* **2019,** *20* (16).
41. Cauët, E.; Dehareng, D.; Liévin, J. Ab initio study of the ionization of the DNA bases: ionization potentials and excited states of the cations. *The Journal of Physical Chemistry A.* **2006,** *110* (29), 9200–9211.
42. Ma, J.; Kumar, A.; Muroya, Y.; Yamashita, S.; Sakurai, T.; Denisov, S. A.; Sevilla, M. D.; Adhikary, A.; Seki, S.; Mostafavi, M. Observation of dissociative quasi-free electron attachment to nucleoside via excited anion radical in solution. *Nature Communications.* **2019,** *10* (1), 102.
43. Eiben, K. Solvated and Stabilized Electrons in Radiation-Chemical Processes. *Angewandte Chemie International Edition.* **1970,** *9* (8), 619–632.

44. Kumar, A.; Sevilla, M. D. Role of excited states in low-energy electron (LEE) induced strand breaks in DNA model systems: influence of aqueous environment. *Chemphyschem : A European Journal of Chemical Physics and Physical Chemistry.* **2009,** *10* (9-10), 1426–1430.
45. Lide, D.; Bruno, T. J.; Rumble, J. R. *CRC handbook of chemistry and physics. A ready-reference book of chemical and physical data*, 100th edition, 2019.
46. Allan, M. Study of triplet states and short-lived negative ions by means of electron impact spectroscopy. *Journal of Electron Spectroscopy and Related Phenomena.* **1989,** *48* (2), 219–351.
47. Schulz, G. J. Resonances in Electron Impact on Diatomic Molecules. *Reviews of Modern Physics.* **1973,** *45* (3), 423–486.
48. Moran, T. F. Electron Transfer Reactions. *Electron–Molecule Interactions and their Applications*; Elsevier, 1984; pp 1–64.
49. Birtwistle, D. T.; Herzenberg, A. Vibrational excitation of N 2 by resonance scattering of electrons. *Journal of Physics B: Atomic and Molecular Physics.* **1971,** *4* (1), 53–70.
50. Fenzlaff, M.; Gerhard, R.; Illenberger, E. Associative and dissociative electron attachment by SF 6 and SF 5 Cl. *The Journal of Chemical Physics.* **1988,** *88* (1), 149–155.
51. Jaffke, T.; Illenberger, E.; Lezius, M.; Matejcik, S.; Smith, D.; Märk, T. D. Formation of C60− and C70− by free electron capture. Activation energy and effect of the internal energy on lifetime. *Chemical Physics Letters.* **1994,** *226* (1-2), 213–218.
52. Bald, I.; Langer, J.; Tegeder, P.; Ingólfsson, O. From isolated molecules through clusters and condensates to the building blocks of life. *International Journal of Mass Spectrometry.* **2008,** *277* (1-3), 4–25.
53. E. Illenberger, J. Momigny: Gaseous Molecular Ions, An Introduction to Elementary Processes Induced by Ionization, Vol. 2, aus der Reihe: Topics in Physical Chemistry, Steinkopff Verlag, Springer-Verlag, Darmstadt, ISBN 3-7985-0870-4, New York, ISBN 0-387. *Berichte der Bunsengesellschaft für physikalische Chemie* **1992,** *96* (11), 1796.
54. Olive, P. L. The Role of DNA Single- and Double-Strand Breaks in Cell Killing by Ionizing Radiation. *Radiation Research.* **1998,** *150* (5), S42.
55. Mehta, A.; Haber, J. E. Sources of DNA double-strand breaks and models of recombinational DNA repair. *Cold Spring Harbor Perspectives in Biology.* **2014,** *6* (9), a016428.
56. Schürmann, R.; Vogel, S.; Ebel, K.; Bald, I. The Physico-Chemical Basis of DNA Radiosensitization: Implications for Cancer Radiation Therapy. *Chemistry (Weinheim an der Bergstrasse, Germany)* **2018,** *24* (41), 10271–10279.

57. Huels, M. A.; Boudaïffa, B.; Cloutier, P.; Hunting, D.; Sanche, L. Single, double, and multiple double strand breaks induced in DNA by 3-100 eV electrons. *Journal of the American Chemical Society.* **2003,** *125* (15), 4467–4477.
58. Boudaïffa, B.; Cloutier, P.; Hunting, D.; Huels, M. A.; Sanche, L. Resonant formation of DNA strand breaks by low-energy (3 to 20 eV) electrons. *Science (New York, N.Y.)* **2000,** *287* (5458), 1658–1660.
59. Martin, F.; Burrow, P. D.; Cai, Z.; Cloutier, P.; Hunting, D.; Sanche, L. DNA strand breaks induced by 0-4 eV electrons: the role of shape resonances. *Physical Review Letters.* **2004,** *93* (6), 68101.
60. Li, Z.; Cloutier, P.; Sanche, L.; Wagner, J. R. Low-energy electron-induced DNA damage: effect of base sequence in oligonucleotide trimers. *Journal of the American Chemical Society.* **2010,** *132* (15), 5422–5427.
61. Solomun, T.; Hultschig, C.; Illenberger, E. Microarray technology for the study of DNA damage by low-energy electrons. *The European Physical Journal D.* **2005,** *35* (2), 437–441.
62. Rankin, D. W.H. CRC handbook of chemistry and physics, 89th edition, edited by David R. Lide. *Crystallography Reviews.* **2009,** *15* (3), 223–224.
63. Vyšín, L.; Pachnerová Brabcová, K.; Štěpán, V.; Moretto-Capelle, P.; Bugler, B.; Legube, G.; Cafarelli, P.; Casta, R.; Champeaux, J. P.; Sence, M.; Vlk, M.; Wagner, R.; Štursa, J.; Zach, V.; Incerti, S.; Juha, L.; Davídková, M. Proton-induced direct and indirect damage of plasmid DNA. *Radiation and Environmental Biophysics.* **2015,** *54* (3), 343–352.
64. Michaelidesová, A.; Vachelová, J.; Klementová, J.; Urban, T.; Pachnerová Brabcová, K.; Kaczor, S.; Falk, M.; Falková, I.; Depeš, D.; Vondráček, V.; Davídková, M. In Vitro Comparison of Passive and Active Clinical Proton Beams. *International Journal of Molecular Sciences.* **2020,** *21* (16).
65. Niederhuber, J. E.; Armitage, J. O.; Doroshow, J. H.; Tepper, J. E.; Kastan, M. B.; Abeloff, M. D. *Abeloff's clinical oncology*, 5th ed.; Saunders: Philadelphia, Pennsylvania, 2013.
66. Ma, C.-M. C.; Lomax, T. *Proton and carbon ion therapy*; Imaging in Medical Diagnosis and Therapy; Taylor & Francis: Boca Raton, 2013.
67. Heidelberg Ion Beam Therapy Center Proton and Heavy Ion Therapy. https://www.heidelberg-university-hospital.com/de/erkrankungenbehandlungen/tumorerkrankungen/protonen-und-schwerionentherapie/.
68. Shewach, D. S.; Lawrence, T. S. Antimetabolite radiosensitizers. *Journal of Clinical Oncology: Official Journal of the American Society of Clinical Oncology.* **2007,** *25* (26), 4043–4050.
69. Isanbor, C.; O'Hagan, D. Fluorine in medicinal chemistry: A review of anti-cancer agents. *Journal of Fluorine Chemistry.* **2006,** *127* (3), 303–319.

70. HEIDELBERGER, C.; CHAUDHURI, N. K.; DANNEBERG, P.; MOOREN, D.; GRIESBACH, L.; DUSCHINSKY, R.; SCHNITZER, R. J.; PLEVEN, E.; SCHEINER, J. Fluorinated pyrimidines, a new class of tumour-inhibitory compounds. *Nature.* **1957,** *179* (4561), 663–666.
71. Mini, E.; Nobili, S.; Caciagli, B.; Landini, I.; Mazzei, T. Cellular pharmacology of gemcitabine. *Annals of Oncology : Official Journal of the European Society for Medical Oncology.* **2006,** *17 Suppl 5*, v7-12.
72. Huang, P.; Robertson, L. E.; Wright, S.; Plunkett, W. High molecular weight DNA fragmentation: a critical event in nucleoside analogue-induced apoptosis in leukemia cells. *Clinical Cancer Research : An Official Journal of the American Association for Cancer Research.* **1995,** *1* (9), 1005–1013.
73. Lee, K.; Choi, Y.; Gumina, G.; Zhou, W.; Schinazi, R. F.; Chu, C. K. Structure-activity relationships of 2'-fluoro-2',3'-unsaturated D-nucleosides as anti-HIV-1 agents. *Journal of Medicinal Chemistry.* **2002,** *45* (6), 1313–1320.
74. Wilson, G. D.; Bentzen, S. M.; Harari, P. M. Biologic basis for combining drugs with radiation. *Seminars in Radiation Oncology.* **2006,** *16* (1), 2–9.
75. Kopyra, J.; Keller, A.; Bald, I. On the role of fluoro-substituted nucleosides in DNA radiosensitization for tumor radiation therapy. *RSC Advances.* **2014,** *4* (13), 6825.
76. World Health Organization (WHO) Model Lists of Essential Medicines. https://www.who.int/medicines/publications/essentialmedicines/en/.
77. Liu, P.; Sharon, A.; Chu, C. K. Fluorinated Nucleosides: Synthesis and Biological Implication. *Journal of Fluorine Chemistry.* **2008,** *129* (9), 743–766.
78. Montgomery, J. A.; Shortnacy-Fowler, A. T.; Clayton, S. D.; Riordan, J. M.; Secrist, J. A. Synthesis and biologic activity of 2'-fluoro-2-halo derivatives of 9-beta-D-arabinofuranosyladenine. *Journal of Medicinal Chemistry.* **1992,** *35* (2), 397–401.
79. Faderl, S.; Gandhi, V.; Kantarjian, H. M. Potential role of novel nucleoside analogs in the treatment of acute myeloid leukemia. *Current Opinion in Hematology.* **2008,** *15* (2), 101–107.
80. Simons, J. How do low-energy (0.1-2 eV) electrons cause DNA-strand breaks? *Accounts of Chemical Research.* **2006,** *39* (10), 772–779.
81. Berdys, J.; Anusiewicz, I.; Skurski, P.; Simons, J. Damage to model DNA fragments from very low-energy (<1 eV) electrons. *Journal of the American Chemical Society.* **2004,** *126* (20), 6441–6447.
82. Bald, I.; Kopyra, J.; Illenberger, E. Selective excision of C5 from D-ribose in the gas phase by low-energy electrons (0-1 eV): implications for the mechanism of DNA damage. *Angewandte Chemie Internation Edition.* **2006,** *45* (29), 4851–4855.
83. Kumar, A.; Sevilla, M. D. Low-energy electron attachment to 5'-thymidine monophosphate: modeling single strand breaks through dissociative electron attachment. *The Journal of Physical Chemistry. B.* **2007,** *111* (19), 5464–5474.

84. Alvarellos, M. L.; Lamba, J.; Sangkuhl, K.; Thorn, C. F.; Wang, L.; Klein, D. J.; Altman, R. B.; Klein, T. E. PharmGKB summary: gemcitabine pathway. *Pharmacogenetics and Genomics.* **2014,** *24* (11), 564–574.
85. Plunkett, W.; Huang, P.; Xu, Y. Z.; Heinemann, V.; Grunewald, R.; Gandhi, V. Gemcitabine: metabolism, mechanisms of action, and self-potentiation. *Seminars in Oncology.* **1995,** *22* (4 Suppl 11), 3–10.
86. Fehlauer, F.; Muench, M.; Smid, E.; Slotman, B.; Richter, E.; van der Valk, P.; Sminia, P. Combined modality therapy of gemcitabine and irradiation on human glioma spheroids derived from cell lines and biopsy tissue. *Oncology Reports.* **2006**.
87. Sousa Cavalcante, L. de; Monteiro, G. Gemcitabine: metabolism and molecular mechanisms of action, sensitivity and chemoresistance in pancreatic cancer. *European Journal of Pharmacology.* **2014,** *741*, 8–16.
88. Baccarelli, I.; Bald, I.; Gianturco, F. A.; Illenberger, E.; Kopyra, J. Electron-induced damage of DNA and its components: Experiments and theoretical models. *Physics Reports.* **2011,** *508* (1-2), 1–44.
89. Solomun, T.; Seitz, H.; Sturm, H. DNA damage by low-energy electron impact: dependence on guanine content. *The Journal of Physical Chemistry. B.* **2009,** *113* (34), 11557–11559.
90. Sanche, L. Low-Energy Electron Damage to DNA and its Basic Constituents. *The Journal of Physical Chemistry A.* **2003,** *68* (5), C108-C112.
91. Paterson, M. J.; Christiansen, O.; Jensen, F.; Ogilby, P. R. Overview of theoretical and computational methods applied to the oxygen-organic molecule photosystem. *Photochemistry and Photobiology.* **2006,** *82* (5), 1136–1160.
92. Daşu, A.; Denekamp, J. New insights into factors influencing the clinically relevant oxygen enhancement ratio. *Radiotherapy and Oncology.* **1998,** *46* (3), 269–277.
93. Sanche, L. Biological chemistry: Beyond radical thinking. *Nature.* **2009,** *461* (7262), 358–359.
94. Tørring, T.; Helmig, S.; Ogilby, P. R.; Gothelf, K. V. Singlet oxygen in DNA nanotechnology. *Accounts of Chemical Research.* **2014,** *47* (6), 1799–1806.
95. Ray, A.; Liosi, K.; Ramakrishna, S. N.; Spencer, N. D.; Kuzuya, A.; Yamakoshi, Y. Single-Molecule AFM Study of DNA Damage by 1O2 Generated from Photoexcited C60. *The Journal of Physical Chemistry Letters.* **2020,** *11* (18), 7819–7826.
96. Fudickar, W.; Linker, T. Synthesis of Pyridylanthracenes and Their Reversible Reaction with Singlet Oxygen to Endoperoxides. *The Journal of Organic Chemistry.* **2017,** *82* (17), 9258–9262.
97. Fudickar, W.; Linker, T. Release of Singlet Oxygen from Aromatic Endoperoxides by Chemical Triggers. *Angewandte Chemie International Edition.* **2018,** *57* (39), 12971–12975.

98. Fudickar, W.; Linker, T. Structural motives controlling the binding affinity of 9,10-bis(methylpyridinium)anthracenes towards DNA. *Bioorganic & Medicinal Chemistry.* **2020,** *28* (8), 115432.
99. Basu, U.; Otto, S.; Heinze, K.; Gasser, G. Biological Evaluation of the NIR-Emissive Ruby Analogue [Cr(ddpd) 2][BF 4] 3 as a Photodynamic Therapy Photosensitizer. *European Journal of Inorganic Chemistry.* **2019,** *2019* (1), 37–41.
100. Wang, C.; Otto, S.; Dorn, M.; Heinze, K.; Resch-Genger, U. Luminescent TOP Nanosensors for Simultaneously Measuring Temperature, Oxygen, and pH at a Single Excitation Wavelength. *Analytical Chemistry.* **2019,** *91* (3), 2337–2344.
101. Wang, C.; Otto, S.; Dorn, M.; Kreidt, E.; Lebon, J.; Sršan, L.; Di Martino-Fumo, P.; Gerhards, M.; Resch-Genger, U.; Seitz, M.; Heinze, K. Deuterated Molecular Ruby with Record Luminescence Quantum Yield. *Angewandte Chemie International Edition.* **2018,** *57* (4), 1112–1116.
102. Kumar, S. V. K.; Pota, T.; Peri, D.; Dongre, A. D.; Rao, B. J. Low energy electron induced damage to plasmid DNA pQE30. *The Journal of Chemical Physics.* **2012,** *137* (4), 45101.
103. Anfinsen, C. B.; Edsall, J. T.; Richards, F. M. *Advances in protein chemistry*; Advances in Protein Chemistry v. 37; Academic Press: Orlando, FL, London, 1985.
104. Binnig; Quate; Gerber. Atomic force microscope. *Physical Review Letters.* **1986,** *56* (9), 930–933.
105. Howland, R. & Benatar, L., Ed. *A practical guide to scanning probe microscopy*: DIANE Publishing Company, Collingdale, PA, 1998.
106. Banyasz, A.; Balanikas, E.; Martinez-Fernandez, L.; Baldacchino, G.; Douki, T.; Improta, R.; Markovitsi, D. Radicals Generated in Tetramolecular Guanine Quadruplexes by Photoionization: Spectral and Dynamical Features. *The journal of physical chemistry B.* **2019,** *123* (23), 4950–4957.
107. Banyasz, A.; Ketola, T.; Martínez-Fernández, L.; Improta, R.; Markovitsi, D. Adenine radicals generated in alternating AT duplexes by direct absorption of low-energy UV radiation. *Faraday Discussions.* **2018,** *207* (0), 181–197.
108. Boulanouar, O.; Fromm, M.; Mavon, C.; Cloutier, P.; Sanche, L. Dissociative electron attachment to DNA-diamine thin films: impact of the DNA close environment on the OH- and O- decay channels. *The Journal of Chemical Physics.* **2013,** *139* (5), 55101.
109. Abdoul-Carime, H.; Cloutier, P.; Sanche, L. Low-Energy (5–40 eV) Electron-Stimulated Desorption of Anions from Physisorbed DNA Bases. *Radiation Research.* **2001,** *155* (4), 625–633.
110. Abdoul-Carime, H.; Dugal, P.-C.; Sanche, L. Damage Induced by 1–30 eV Electrons on Thymine- and Bromouracil-Substituted Oligonucleotides. *Radiation Research.* **2000,** *153* (1), 23–28.

111. Safaee, N.; Noronha, A. M.; Rodionov, D.; Kozlov, G.; Wilds, C. J.; Sheldrick, G. M.; Gehring, K. Structure of the parallel duplex of poly(A) RNA: evaluation of a 50 year-old prediction. *Angewandte Chemie International Edition.* **2013,** *52* (39), 10370–10373.
112. Kibbe, W. A. OligoCalc: an online oligonucleotide properties calculator. *Nucleic Acids Research.* **2007,** *35* (Web Server issue), W43-6.
113. Panajotovic, R.; Martin, F.; Cloutier, P.; Hunting, D.; Sanche, L. Effective cross sections for production of single-strand breaks in plasmid DNA by 0.1 to 4.7 eV electrons. *Radiation Research.* **2006,** *165* (4), 452–459.
114. Boulanouar, O.; Fromm, M.; Bass, A. D.; Cloutier, P.; Sanche, L. Absolute cross section for loss of supercoiled topology induced by 10 eV electrons in highly uniform /DNA/1,3-diaminopropane films deposited on highly ordered pyrolitic graphite. *The Journal of Chemical Physics.* **2013,** *139* (5), 55104.
115. Lemelin, V.; Bass, A. D.; Cloutier, P.; Sanche, L. Low energy (1-19 eV) electron scattering from condensed thymidine (dT) II: comparison of vibrational excitation cross sections with those of tetrahydrofuran and the recalibrated values of thymine. *Physical Chemistry Chemical Physics : PCCP.* **2019,** *21* (43), 23818–23825.
116. Keller, A.; Kopyra, J.; Gothelf, K. V.; Bald, I. Electron-induced damage of biotin studied in the gas phase and in the condensed phase at a single-molecule level. *International Journal of Mass Spectrometry.* **2013,** *15* (8), 83045.
117. Förster, T. *Fluoreszenz organischer Verbindungen*, Unveränd. Nachdr. d. 1. Aufl. im Literaturverzeichnis ergänzt um spätere Veröffentlichungen d. Autors; Vandenhoeck & Ruprecht: Göttingen, 1982.
118. McGrath, R. A.; Williams, R. W. Reconstruction in vivo of irradiated Escherichia coli deoxyribonucleic acid; the rejoining of broken pieces. *Nature.* **1966,** *212* (5061), 534–535.
119. Dong, Y.; Zhou, L.; Tian, Q.; Zheng, Y.; Sanche, L. Chemoradiation Cancer Therapy: Molecular Mechanisms of Cisplatin Radiosensitization. *The Journal of Physical Chemistry C.* **2017,** *121* (32), 17505–17513.
120. Shao, Y.; Dong, Y.; Hunting, D.; Zheng, Y.; Sanche, L. Unified Mechanism for the Generation of Isolated and Clustered DNA Damages by a Single Low Energy (5–10 eV) Electron. *The Journal of Physical Chemistry C.* **2017,** *121* (4), 2466–2472.
121. Sutherland, B. M.; Bennett, P. V.; Sidorkina, O.; Laval, J. Clustered damages and total lesions induced in DNA by ionizing radiation: oxidized bases and strand breaks. *Biochemistry.* **2000,** *39* (27), 8026–8031.
122. Sutherland, B. M.; Bennett, P. V.; Sutherland, J. C.; Laval, J. Clustered DNA Damages Induced by X Rays in Human Cells. *Radiation Research.* **2002,** *157* (6), 611–616.

123. Ward, J. F. Radiation mutagenesis: the initial DNA lesions responsible. *Radiation Research.* **1995,** *142* (3), 362–368.
124. Li, Z.; Cloutier, P.; Sanche, L.; Wagner, J. R. Low-energy electron-induced damage in a trinucleotide containing 5-bromouracil. *The Journal of Physical Chemistry. B.* **2011,** *115* (46), 13668–13673.
125. Anusiewicz, I.; Berdys, J.; Sobczyk, M.; Skurski, P.; Simons, J. Effects of Base π-Stacking on Damage to DNA by Low-Energy Electrons. *The Journal of Physical Chemistry A.* **2004,** *108* (51), 11381–11387.
126. Barrios, R.; Skurski, P.; Simons, J. Mechanism for Damage to DNA by Low-Energy Electrons †. *The Journal of Physical Chemistry. B.* **2002,** *106* (33), 7991–7994.
127. Berdys, J.; Anusiewicz, I.; Skurski, P.; Simons, J. Theoretical Study of Damage to DNA by 0.2−1.5 eV Electrons Attached to Cytosine †. *The Journal of Physical Chemistry A.* **2004,** *108* (15), 2999–3005.
128. Wang, C.-R.; Nguyen, J.; Lu, Q.-B. Bond breaks of nucleotides by dissociative electron transfer of nonequilibrium prehydrated electrons: a new molecular mechanism for reductive DNA damage. *Journal of the American Chemical Society.* **2009,** *131* (32), 11320–11322.
129. Sponer, J.; Riley, K. E.; Hobza, P. Nature and magnitude of aromatic stacking of nucleic acid bases. *Physical Chemistry Chemical Physics : PCCP.* **2008,** *10* (19), 2595–2610.
130. Sugiyama, H.; Saito, I. Theoretical Studies of GG-Specific Photocleavage of DNA via Electron Transfer: Significant Lowering of Ionization Potential and 5′-Localization of HOMO of Stacked GG Bases in B-Form DNA. *Journal of the American Chemical Society.* **1996,** *118* (30), 7063–7068.
131. Markus, T. Z.; Daube, S. S.; Naaman, R. Cooperative effect in the electronic properties of human telomere sequence. *The Journal of Physical Chemistry. B.* **2010,** *114* (43), 13897–13903.
132. Cauët, E. Unique hole-trapping property of the human telomere sequence. *Journal of Biomolecular Structure & Dynamics.* **2011,** *29* (3), 557–561.
133. Kumar, A.; Sevilla, M. D. Density functional theory studies of the extent of hole delocalization in one-electron oxidized adenine and guanine base stacks. *The Journal of Physical Chemistry. B.* **2011,** *115* (17), 4990–5000.
134. Colson, A. O.; Besler, B.; Sevilla, M. D. Ab initio molecular orbital calculations on DNA radical ions. 4. Effect of hydration on electron affinities and ionization potentials of base pairs. *The Journal of Physical Chemistry.* **1993,** *97* (51), 13852–13859.
135. Straub, H. C.; Lin, D.; Lindsay, B. G.; Smith, K. A.; Stebbings, R. F. Absolute partial cross sections for electron-impact ionization of CH 4 from threshold to 1000 eV. *The Journal of Chemical Physics.* **1997,** *106* (11), 4430–4435.

136. Vogel, S.; Rackwitz, J.; Schürman, R.; Prinz, J.; Milosavljević, A. R.; Réfrégiers, M.; Giuliani, A.; Bald, I. Using DNA origami nanostructures to determine absolute cross sections for UV photon-induced DNA strand breakage. *The Journal of Physical Chemistry Letters.* **2015,** *6* (22), 4589–4593.
137. Lindsay, B. G.; Rejoub, R.; Stebbings, R. F. Production of positive ion pairs by electron-impact ionization of CH4. *The Journal of Chemical Physics.* **2001,** *114* (22), 10225–10226.
138. Mittleman, M. Electronic and Ionic Impact Phenomena. H. S. W. Massey, E. H. S. Burhop, and H. B. Gilbody. Second edition, in four volumes. Vol. 1, Collision of Electrons with Atoms. H. S. W. Massey and E. H. S. Burhop., Vol. 2, Electron Collisions with Molecules and Photo-ionization. H. S. W. Massey. Oxford University Press, New York, 1969. International Series of Monographs on Physics. *Science (New York, N.Y.)* **1970,** *168* (3930), 462–463.
139. Schröter, M.-A.; Meyer, S.; Hahn, M. B.; Solomun, T.; Sturm, H.; Kunte, H. J. Ectoine protects DNA from damage by ionizing radiation. *Scientific Reports.* **2017,** *7* (1), 15272.
140. Murphy, J. D.; Lucas, D. R.; Somnay, Y. R.; Hamstra, D. A.; Ray, M. E. Gemcitabine-mediated radiosensitization of human soft tissue sarcoma. *Translational Oncology.* **2008,** *1* (1), 50–56.
141. McGinn, C. J.; Lawrence, T. S. Recent advances in the use of radiosensitizing nucleosides. *Seminars in Radiation Oncology.* **2001,** *11* (4), 270–280.
142. Mauracher, A.; Huber, S. E. Dependence of Electronic Properties of DNA Single Strands on Size and Environment. *ACS Omega.* **2019,** *4* (6), 10791–10798.
143. Kollmann, F.; Ramakrishnan, S.; Shen, B.; Grundmeier, G.; Kostiainen, M. A.; Linko, V.; Keller, A. Superstructure-Dependent Loading of DNA Origami Nanostructures with a Groove-Binding Drug. *ACS Omega.* **2018,** *3* (8), 9441–9448.
144. Neidle, S. DNA minor-groove recognition by small molecules. *Natural Product Reports.* **2001,** *18* (3), 291–309.
145. Tawar, U.; Jain, A. K.; Chandra, R.; Singh, Y.; Dwarakanath, B. S.; Chaudhury, N. K.; Good, L.; Tandon, V. Minor groove binding DNA ligands with expanded A/T sequence length recognition, selective binding to bent DNA regions and enhanced fluorescent properties. *Biochemistry.* **2003,** *42* (45), 13339–13346.
146. Otto, S.; Grabolle, M.; Förster, C.; Kreitner, C.; Resch-Genger, U.; Heinze, K. Cr(ddpd)2(3+): A Molecular, Water-Soluble, Highly NIR-Emissive Ruby Analogue. *Angewandte Chemie International Edition.* **2015,** *54* (39), 11572–11576.

7 Appendix

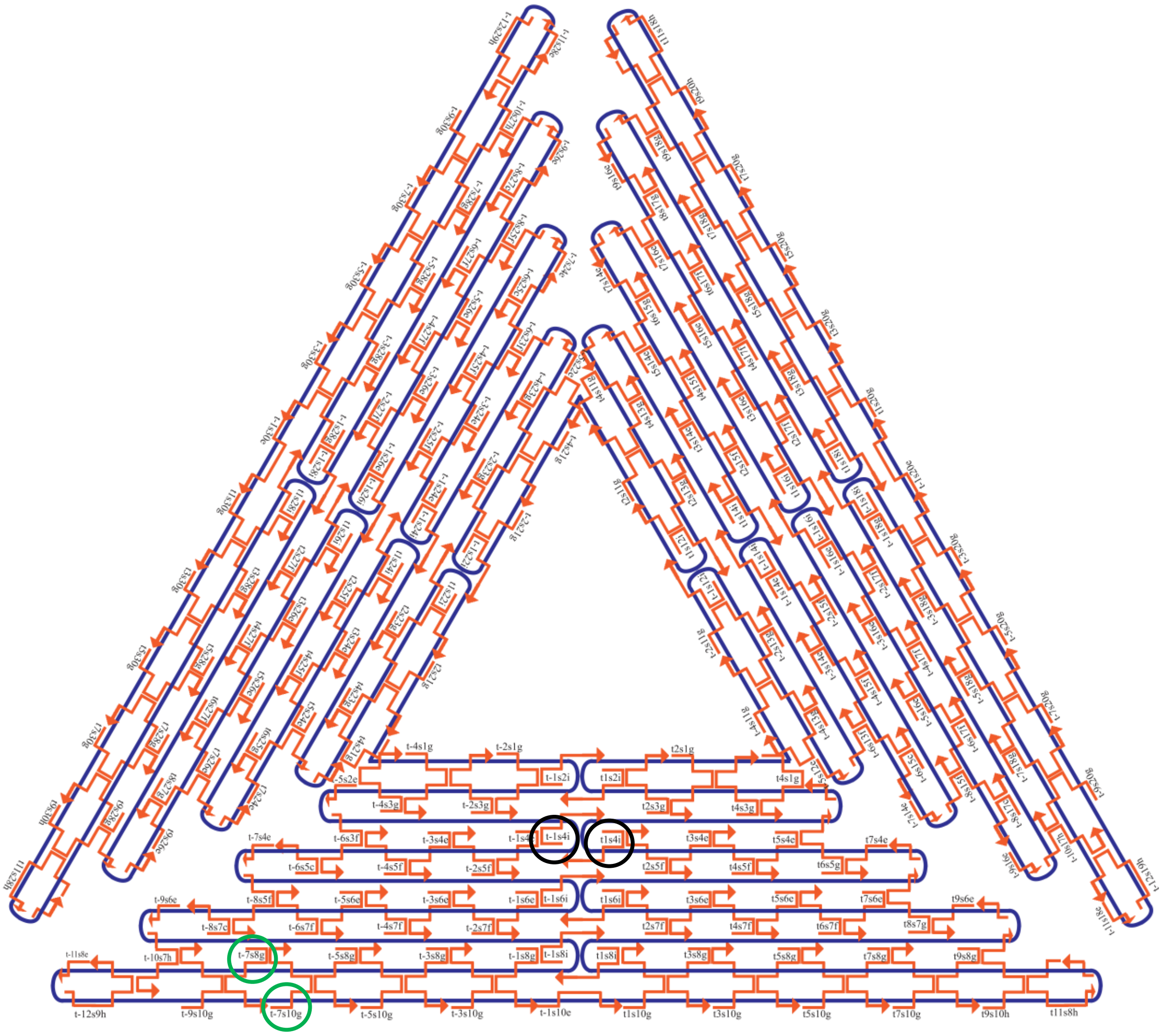

Figure 7.1 Schematic illustration of the unmodified triangular DNA origami template. Circled staple strand codes (black – middle positon; green – side positon) represents the modified positions on the DNA origami triangle.

Table 7.1. List of all modified DNA target sequences used during the irradiation experiments.

	List of modified sequences	
Name	**Sequence 5′ → 3′**	**Staple code**
A_4	Bt-$(A)_4$	t-1s4i/14i/24i
A_8	Bt-$(A)_8$	t-7s8g/18g/28g
A_{12}	Bt-$(A)_{12}$	t-1s4i/14i/24i
A_{16}	Bt-$(A)_{16}$	t-7s8g/18g/28g
A_{20}	Bt-$(A)_{20}$	t-1s4i/14i/24i
$(CAC)_4$	Bt-$(CAC)_4$	t-7s10g/20g/30g
$(GTG)_4$	$(GTG)_4$-Bt	t2s5f/15f/25f
HP-1	$(CAC)_4$T(Bt-dT)$T_2$$(GTG)_4$	t-7s10g/20g/30g
HP-Bt	T(Bt-dT)T_2	t2s5f
T-Bt	T-Bt	t2s5f
GCCC	GCCC	t-1s4i/14i/24i
CGCC	CGCC	t-7s8g/18g/28g
GC^{dF}CC	GC^{dF}CC	t-1s4i/14i/24i
^{dF}CGCC	^{dF}CGCC	t-7s8g/18g/28g

Table 7.2 List of all staple strands used for target sequences positioning on the DNA origami triangle.

	List of modified sequences used during experiments
Staple code	**Sequence 5′ → 3′**
t-1s4i	T TTA ACC TAT CAT AGG TCT GAG AGT TCC AGT A
t-1s14i	C AAC AGT TTA TGG GAT TTT GCT AAT CAA AAG G
t-1s24i	GGA AGA TGG GGA CGA CGA CAG TAA TCA TAT T
t-7s8g	GC GCC TGT TAT TCT AAG AAC GCG ATT CCA GAG CCT AAT TT
t-7s18g	C ACT TAA TCT TGA CAA GAA CTT AAT CAT TGT GAA TT
t-7s28g	TT CCA GTC CTT ATA AAT CAA AAG AGA ACC ATC ACC CAA AT
t-7s10g	GCC AGT TAC AAA ATA ATA GA AGG CTT ATC CGG TTA TCA AC
t-7s20g	ACC TTA TGC GAT TTT ATG ACC TTC ATC AAG AGC ATC TTT G
t-7s30g	CAA GTT TTT TGG GGT CGA AAT CGG CAA AAT CCG GGA AAC C
t2s5f	CCG GAA CCC AGA ATG GAA AGC GCA ACA TGG CT
t2s15f	ATA GTA GTA TGC AAT GCC TGA GTA GGC CGG AG
t2s25f	AAG GAA TTA CAA AGA AAC CAC CAG TCA GAT GA
t5s8g	TTG ACG GAA ATA CAT ACA TAA AGG GCG CTA ATA TCA GAG A
t5s18g	TAA TTG CTT TAC CCT GAC TAT TAT GAG GCA TAG TAA GAG C
t5s28g	GAA TAC GTA ACA GGA AAA ACG CTC CTA AAC AGG AGG CCG A

Table 7.3 List of the calculated current percentage $I_{\%}$ for every used electron energy.

Settings for all electron energies used by the flood gun					
Energy [eV]	**ENG [V]**	**FIL [A]**	**ANO [V]**	$I_{\%}$	f
5.0	8.2	2.1	1.4	5.60	2.75
6.0	9.2		1.5	5.77	2.60
7.0	10.2		1.7	5.88	2.42
8.0	11.2		1.7	5.90	2.26
8.4	11.6		1.7	5.93	2.16
8.8	12.0		1.8	7.39	2.14
9.0	12.2		1.8	5.91	2.10
10.0	13.2		1.9	6.00	2.02
11.0	14.2		1.9	5.90	1.95
12.0	15.2		2.0	6.22	1.87
13.0	16.2		2.0	5.93	1.72
14.0	17.2		2.1	7.28	1.66
15.0	18.2		2.1	6.32	1.61
16.0	19.2		2.1	6.12	1.50
17.0	20.2		2.2	5.99	1.30
18.0	21.2		2.2	6.07	1.25
19.0	22.2		2.3	6.12	1.08
20.0	23.2		2.3	6.11	1.02

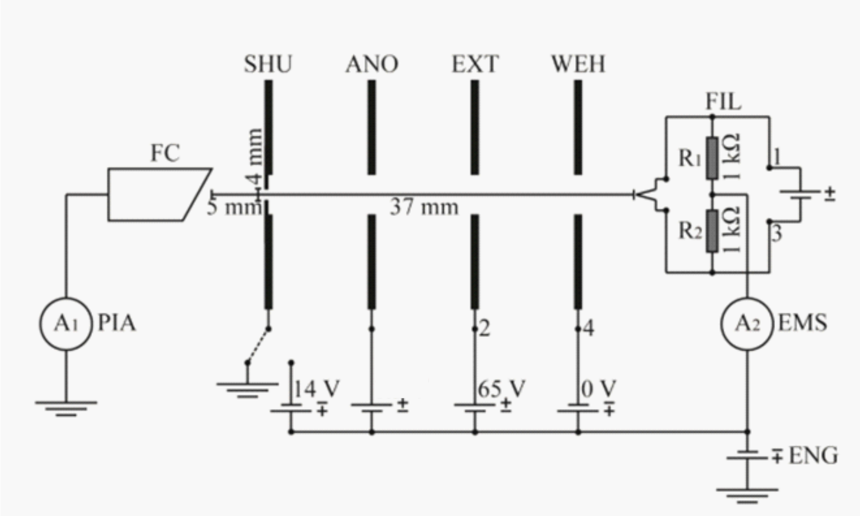

Figure 7.2 Technical drawing of the electrical circuit of the electron gun FS100. The electron gun includes the four electrostatic lenses shutter (SHU), anode (ANO), extractor (EXT), the Wehnelt cylinder (WEH) and the beam voltage (ENG). A multimeter (EMS) is connected to the filament (FIL) and controls the emission current. The picoamperemeter (PIA) is connected to the faraday cup (FC) collecting the absolute current I_{FC}. Settings for ANO and ENG vary for each electron energy (see tab. 7.3) This image is adopted from ref. [15].

List of publications

1. *Low-energy electron induced single and double strand breaks in well-defined oligonucleotides and the role of negative ion resonances in DNA radiosensitization*; K. Ebel, J. Olszewski and I. Bald [Manuscript in preparation]
2. *DNA binding and visible light induces DNA damage by Chromium complexes* K. Ebel, C. Wang, U. Resch-Genger, K. Heinze, I. Bald [Manuscript in preparation]
3. *Length and Energy Dependence of Low-Energy Electron-Induced Strand Breaks in Poly(A) DNA*; K. Ebel and I. Bald, *International Journal of Molecular Sciences 2020, 21, 111*
4. *Kinetics of Molecular Decomposition Under Irradiation of Gold Nanoparticles with Nanosecond Laser Pulses - A 5-Bromouracil Case Study*; T. Marques, R. Schürmann, K. Ebel, C. Heck, M. Śmiałek, S. Eden, N. Mason and I. Bald, *The Journal of Molecular Physics 2020, 152, 124712*
5. *Vacuum-UV induced DNA strand breaks - influence of the radiosensitizers 5-bromouracil and 8-bromoadenine*; S. Vogel, K. Ebel, C. Heck, R. Schürmann, A. Milosavljević, A. Giuliani and I. Bald, *Physical Chemistry Chemical Physics 2019, 21, 1972*
6. *Vacuum-UV and Low-Energy Electron Induced DNA Strand Breaks – Influence of the DNA Sequence and Substrate*; S. Vogel, K. Ebel, R. Schürmann, T. Meiling, A. Milosavljević, A. Giuliani and I. Bald, *A European Journal - ChemPhysChem 2019, 20, 1*
7. *Role of Valence Band States and Plasmonic Enhancement in Electron-Transfer-Induced Transformation of Nitrothiophenol*; R. Schürmann, K. Ebel, C. Nicolas, A. Milosavljevic and I. Bald, *The Journal of Physical Chemistry Letters 2019, 10, 3153*
8. *The physico-chemical basis of DNA radiosensitization - Implications for cancer radiation therapy*; R. Schürmann, S. Vogel, K. Ebel and I. Bald, *Chemistry A European Journal 2018, 24, 10271*
9. *Photophysics and Chemistry of Nitrogen-Doped Carbon Nanodots with High Photoluminescence Quantum Yield*; T. T. Meiling, R. Schürmann, S. Vogel, K. Ebel, C. Nicolas, A. R. Milosavljević and I. Bald, *The Journal of Physical Chemistry C 2018, 122, 18, 10217*

10. *Sensitizing DNA Towards Low-Energy Electrons with 2-Fluoroadenine*; J. Rackwitz, J. Kopyra, I. Dabkowska, K. Ebel, M. Lj. Rankovic, A. R. Milosavljevic and I. Bald, *Angewandte Chemie International Edition 2016, 55, 10248*

Conference contributions

- Poster: K. Ebel and I. Bald; *LEE-induced DNA strand breaks in 2-fluorocytidine, 2-fluoroadenine and 5-fluorouridine sensitized DNA*, Radiation Research Society, Online conference, **2020**
- Poster: K. Ebel and I. Bald; *Electron-induced single and double strand breaks in DNA determined by using the DNA origami technique*, NANTECH, Helsinki, Finnland **2019**
- Poster: K. Ebel and I. Bald; *Electron-induced single and double strand breaks in DNA determined by using the DNA origami technique;* ***Best Poster Award 1st Place,*** DySoN, Potsdam, Germany **2018**
- Poster: K. Ebel, S. Vogel and I. Bald; *Electron-induced single and double strand breaks in DNA determined by using the DNA origami technique*; Argent conference, Paris, France **2018**
- Poster: K. Ebel and I. Bald; *Electron-induced single and double strand breaks in DNA determined by using the DNA origami technique*; 116th General Assembly of the German Bunsen Society for Physical Chemistry, Kaiserslautern, Germany **2017**
- Poster: K. Ebel, J. Rackwitz, S. Vogel and I. Bald; *Optimization of DNA origami substrates for the study of electron-induced DNA strand breaks;* DNA Nanotechnology, Jena, Germany **2016**
- Talk: K. Ebel and I. Bald; *Study of electron-induced DNA strand breaks using DNA origami substrates*; DNA Mitteldeutschland, Potsdam, Germany **2016**

Acknowledgements

Die hier vorliegende Arbeit ist in Zusammenarbeit mit der Bundesanstalt für Materialforschung und -prüfung und der Universität Potsdam innerhalb der Arbeitsgruppe Hybride Nanostrukturen entstanden. Zunächst gilt mein größter Dank Prof. Dr. Ilko Bald für die exzellente Betreuung meiner Doktorarbeit mit dem interessanten Forschungsgebiet der DNA Strahlenschädigung. In gemeinsamen wissenschaftlichen Diskussionen konnte ich immer viel lernen und Fragen stellen. Darüber hinaus ermöglichte er es mir, meine Arbeit auf verschiedenen Konferenzen zu präsentieren und meine Forschungsergebnisse auf Dienstreisen zu erweitern. Ich werde meine Promotionszeit immer in bester Erinnerung behalten. Zudem möchte ich mich für die Anfertigung des Erstgutachtens zu meiner Doktorarbeit bedanken.

Ferner gilt mein Dank PD Dr. habil. Adrian Keller für die Mitarbeit an der Grundidee der DNA-Origami-Technik und der Erstellung des Zweitgutachtens. Ein zusätzlicher Dank gilt Frau Dr. Marie Davídková, welche mir einen Einblick in das 'Nuclear Physic Institute of the Czech Academy of Science' gewährt hat und für die Anfertigung des Drittgutachtens.

Ohne meine Kollegen Phillip, Steffi Z., Robin, Youngeun, Steffi V., Syvoney, Pia, Janine, Anni und Julia hätte ich nicht eine so tolle Arbeitsatmosphäre, fachliche Hilfe und kreativen Einfälle gehabt. Insbesondere möchte ich mich bei meinen Freunden für die Motivation und Unterstützung bedanken. Dabei gilt ein besonderer Dank Nicky und Patti, die vor allem in der letzten Phase der Doktorarbeit sehr zurückstecken mussten. Des Weiteren gilt eine große Anerkennung meiner Familie für die Unterstützung in allen Lebenslagen. Meinen Eltern bin ich besonders dankbar, welche mir das Studium erst ermöglichten.

Nicht zuletzt gilt mein außerordentlich großer Dank meiner Frau Franzi, welche mit mir durch alle Höhen und Tiefen gegangen ist und in der Endphase sehr auf mich verzichten musste. Danke! Deine tägliche Motivation und dein zugesprochener Mut haben mich sehr unterstützt. Des Weiteren danke ich Oskar, der bei dem Verfassen der Arbeit immer an meiner Seite war.

Zu guter Letzt danke ich den 1.218.017 analysierten DNA-Origami Dreiecken.

Nachweis über Lehrveranstaltungen

Lehrerfahrung: Aus dem Modul „Physikalische Chemie für Nebenfachstudenten“ an der Universität Potsdam wurde je eine Praktikumsbetreuung von Herrn Kenny Ebel mit 2 SWS in den Sommersemestern 2017, 2018, 2019 und 2020 geleitet.

Seminarteilnahme: Herr Kenny Ebel hat während der gesamten Promotionszeit an den im Semester wöchentlich stattfindenden Seminaren der Arbeitsgruppen „Hybride Nanostrukturen“ und „Physikalische Chemie“ an der Universität Potsdam, sowie dem „Doktorandenseminar“ der Bundesanstalt für Materialforschung und -prüfung teilgenommen. Im Seminar der erstgenannten Arbeitsgruppe wurde einmal im Semester der aktuelle Stand der wissenschaftlichen Arbeit in Form eines Vortrages präsentiert, andernfalls einmal pro Jahr.

Kenny Ebel	Prof. Dr. Ilko Bald (Hauptbetreuer)

Versicherung

Hiermit versichere ich, dass ich die vorliegende Arbeit ohne unzulässige Hilfe Dritter und ohne Benutzung anderer als der angegebenen Hilfsmittel angefertigt habe; die aus fremden Quellen direkt oder indirekt übernommenen Gedanken sind als solche kenntlich gemacht. Die Arbeit wurde bisher weder im Inland noch im Ausland in gleicher oder ähnlicher Form einer anderen Prüfungsbehörde vorgelegt. Ich erkenne die Promotionsordnung der Universität Potsdam an.

Potsdam, 25.11.2020

Kenny Ebel